Host-guest dynamics in copper-based Metal-Organic Frameworks

by Charl X. Bezuidenhout

Submitted in partial fulfilment of the requirements for the degree
Doctor of Philosophy

Promoter: Prof. Leonard J. Barbour

Co-promoter: Prof. Catharine Esterhuysen

Department of Chemistry and Polymer Science
Faculty of Science
University of Stellenbosch

December 2017

Declaration

By submitting this dissertation electronically, I declare that the entirety of the work contained therein is my own, original work, that I am the sole author thereof (save to the extent explicitly otherwise stated), that reproduction and publication thereof by Stellenbosch University will not infringe any third party rights and that I have not previously in its entirety or in part submitted it for obtaining any qualification.

December 2017

This work is dedicated to my grandparents who raised me.

Sarah Bezuidenhout and Johannes Jacobus Bezuidenhout

Acknowledgements

I would like to thank my accomplished and erudite supervisors, Prof. Len Barbour and Prof. Catharine Esterhuysen for their guidance and support during the years of my PhD studies. I am grateful for the very stimulating research environment they provided that allowed me to explore my ideas and work independently as well as collaborate with other group members and researchers.

I am very grateful to my family and friends for the support and a great atmosphere outside of research.

I would like to extend my gratitude and appreciation towards the members of the Supramolecular Materials Research Group and the support staff. An especial thankyou is extended to Dr Vincent Smith, Dr Prashant Bhatt, Phumile Sikiti, Dr Emile Engel, Dr Himanshu Aggarwal, Dr Prem Lama and Debbie Isaacs for their support both socially and scientifically.

Finally, I would like to thank the University of Stellenbosch for providing the necessary facilities and the National Research Foundation for funding.

Abstract

A vast number of metal-organic framework materials (MOFs) and structures have been reported in the literature. These materials are of interest as they exhibit a wide range of remarkable properties such as porosity, magnetism, chromism, thermal expansion and dynamic phase-change behaviour. However, many of the reports do not include investigations of all these possible properties, which provides an opportunity to revisit such materials. This study reports three sets of related MOFs that were studied in order to gain insight into their properties and dynamic host-guest interactions.

In the first section three isoreticular copper(II)glutarate based 3D MOFs, whose pore dimensions vary according to the length of the 4,4´-bipyridyl linkers, allows exploration of the effect of increasing pore dimensions on the sorption behaviour of the frameworks. These MOFs capture CO_2 under supercritical conditions and retain the gas under ambient conditions. The retention of the CO_2 makes it possible to model the positions of the molecules within the channels of the frameworks using single-crystal X-ray diffraction analysis (SCXRD). Comparison of the CO_2 gas sorption isotherms with the trend in thermal evolution of the CO_2 adducts provided insight into the dynamics of the host-guest interactions within the MOFs. Theoretical models constructed from crystallographic data were used to calculate framework electrostatic potential maps through DFT and semi-empirical methods. The maps yielded a detailed picture of the electrostatic interactions prevailing at the sorption sites, which shows an electrostatic complementarity between the sorption sites and the CO_2 molecules for two of the MOFs. The $\delta+$ carbon of the CO_2 molecules interacts with the $\delta-$ carboxylate moieties of the framework. Furthermore, both $\delta-$ oxygen atoms of each of the CO_2 molecules interact with several $\delta+$ hydrogen atoms of the framework. This electrostatic complementarity between CO_2 and the sorption site results in a strong interaction, which stabilises the gas within these MOFs.

The second set of MOFs studied comprises two 3D Cu(II)-glutarate-based MOFs with flexible linkers, $[Cu_2(glu)_2(bpa)]$ and $[Cu_2(glu)_2(bpp)]$, that undergo spontaneous phase changes upon solvent loss at room temperature. These MOFs are an extension of the isoreticular series of the previous section. Using SCXRD, we show that the phase changes result in new narrow-channel phases, with a large reduction in solvent accessible volume as compared with the original wide-channel phases. Moreover, the $[Cu_2(glu)_2(bpa)]$ MOF displays a stepped sorption isotherm upon CO_2 sorption at RT. This is indicative of the framework reverting to the wide-channel phase. The positions of the CO_2 molecules in the channels of the frameworks were determined using SCXRD analysis of crystals exposed to supercritical CO_2. Finally, a scan of the potential energy surface using molecular mechanics was conducted to elucidate the mechanism by which the phase change occurs. This appears to be a direct enantiomeric conversion of the glutarate ligands as a result of structural constraints.

The third section describes a one-dimensional porous coordination polymer (PCP) $[Cu_2(acetate)_2(dptz)]_n \bullet 2CHCl_3$, that possesses pleochroic properties, *i.e.* the crystals appear to have different colours depending on their orientation. Solvent exchange with acetonitrile and nitromethane reveals that crystals of this PCP are also solvatochromic. This allows the solvent exchange process to be monitored using optical microscopy with polarised light. The experiment revealed an unexpected double V-shaped pattern in the crystals, which could be explained using an overlay of the measured crystal facets with the crystal structure, along with

modelling of crystal surface adsorption at the different crystal facets. Furthermore, we identified that the crystals must be growth twins subject to the double re-entrant corner effect.

Opsomming

Daar is 'n groot aantal metaal-organiese raamwerk materiale (MOFs) en strukture in die literatuur gerapporteer. Hierdie materiale is van belang aangesien dit 'n wye verskeidenheid van merkwaardige eienskappe soos porositeit, magnetisme, optiese, termiese uitsetting en dinamiese fase-verandering gedrag openbaar. Daar is egter baie publikasies wat nie die ondersoeke van al hierdie moontlike eienskappe behels nie, en bied dus 'n geleentheid aan om sulke materiaal te heroorweeg vir studie. Hierdie studie omhels drie stelle verwante MOFs wat gebestudeer word ten insig van hul materiaal eienskappe en dinamiese gasheer-gas interaksies.

Die eerste artikel omhels drie iso-retikulêre Cu(II)-glutaraat-gebaseerde MOFs, waarvan die porie dimensies wissel na gelang van die 4,4-bipyridyl koppelingsligand lengte, om die effek van verhoging in porie dimensies op die sorpsie gedrag van die raamwerke te bestudeer. Hierdie MOFs neem CO_2 op onder superkritiese kondisies en behou die gas onder omringende omstandighede. Die behoud van CO_2 maak dit moontlik om die posisies van die molekules te modelleer binne die kanale van die raamwerke duer gebruik te maak van enkel-kristal X-straal diffraksie analise (SCXRD). Vergelyking van die CO_2 gas sorpsie isoterme met die tendens in die termiese evolusie van die CO_2 gevulde MOFs bied insig in die dinamika van die gasheer-gas interaksies binne die materiaale. Teoretiese modelle opgebou uit kristallografiese data word gebruik om raamwerk elektrostatiese potensiaal afbeelde te bereken deur gebruik te maak van DFT en semi-empiriese metodes. Die afbeelde lewer 'n gedetailleerde prent van die elektrostatiese interaksie wat heersend is by die sorpsie lokasies. Hierdie interaksies is elektrostatiese ooreenstemmend tussen die sorpsie lokasies en die CO_2 molekules vir twee van die MOFs. Die δ^+ koolstof atoom van die CO_2 molekules form 'n interaksie met die δ^- karboksilaatgroep van die raamwerk. Boonop dit is daar 'n interaksie tussen beide δ^- suurstof atome van die CO_2 molekules en verskeie δ^+ waterstof atome van die raamwerk. Dit elektrostatiese komplementariteit tussen CO_2 en die sorpsie lokasie lei tot 'n sterk interaksie wat die gas binne hierdie MOFs stabiliseer.

Die tweede stel MOFs gebestudeer bestaan uit twee 3D Cu(II)-glutaraat-gebaseerde MOFs met buigsame koppelingsligande, $[Cu_2(glu)_2(bpa)]$ en $[Cu_2(glu)_2(bpp)]$, wat spontaan faseveranderinge ondergaan tydens verlies van die ingeslote oplosmiddel by kamer temperatuur. Hierdie MOFs is 'n uitbreiding van die iso-retikulêre reeks in die vorige afdeling. Die gebruik van enkel-kristal X-straal diffraksie wys dat die faseveranderinge lei tot nuwe smal-kanaal fases met 'n groot afname in gas toeganklik volume in vergelyking met die oorspronklike wye-kanaal fases. Verder vertoon die $[Cu_2(glu)_2(bpa)]$ MOF 'n staps gewyse sorpsie isoterm vir CO_2 by kamer temperatuur. Dit is 'n aanduiding dat die raamwerk terugkeer na die wye-kanaal fase. Die posisies van die CO_2 molekules in die kanale van die raamwerke is bepaal met behulp van SCXRD analise van kristalle blootgestel aan superkritiese CO_2. Ten slotte, 'n skandering van die potensiële energie oppervlak met behulp van molekulêre meganika is gedoen om die meganisme waardeur die faseverandering plaasvind uit te lig. As gevolg van strukturele beperkinge skyn dit na 'n direkte enantiomeriese omskakeling van die glutaraat ligande.

In die derde deel bestudeer ons 1D poreuse koördinasie polymer (PCP) $[Cu_2(asetaat)_2(dptz)]_n \bullet 2ChCl_3$, wat besit veelvoudig kleur eienskappe, die kristalle het aansienlik

verskillende kleure afhangend van die crystal se ruimtelike oriëntasie. Oplosmiddel verwisseling met acetonitril en nitro metaan onthul dat die kristalle van hierdie PCP ook oplosmiddel-verkleuring vertoon. Dit beslaan die moonlikheid om die oplosmiddel uitruilings proses te monitor deur gebruik te maak van optiese mikroskopie met gepolariseerde lig. Die eksperiment onthul 'n onverwagse tweeledige V-patroon in die kristalle. Hierdie waarneming kan verklaar word deur 'n samestelling van die afgemete crystal fasette bo-op die kristalstruktuur en die modellering van kristal-opervlak-adsorpsie op die verskillende Kristal fasette. Verder moet die kristalle onderhewig wees aan meervoudige deurgroeiing soos die dubbel-intrede hoek effek.

Publications

1. H. Aggarwal, P. M. Bhatt, **C. X. Bezuidenhout**, L. J. Barbour, Direct Evidence for Single-Crystal to Single-Crystal Switching of Degree of Interpenetration in a Metal−Organic Framework, *J. Am. Chem. Soc.* **2014**, *136*, 3776–3779.
2. E. R. Engel, V. J. Smith, **C. X. Bezuidenhout**, L. J. Barbour, Uniaxial negative thermal expansion facilitated by weak host–guest interactions, *Chem. Commun*. **2014**, *50*, 4238– 4241.
3. **C. X. Bezuidenhout**, V. J. Smith, P. M. Bhatt, C. Esterhuysen, L. J. Barbour, Extreme Carbon Dioxide Sorption Hysteresis in Open-Channel Rigid Metal–Organic Frameworks, *Angew. Chem. Int. Ed*. **2015**, *54*, 2079–2083.
4. E. R. Engel, V. J. Smith, **C. X. Bezuidenhout**, L. J. Barbour, Thermoresponsive Organic Inclusion Compounds: Modification of Thermal Expansion Behaviour by Simple Guest Replacement, *Chem. Mater*. **2016**, *28*, 5073–5079.
5. P. Lama, H. Aggarwal, **C. X. Bezuidenhout**, L. J. Barbour, Giant Hysteretic Sorption of CO_2: InSitu Crystallographic Visualization of Guest Binding within a Breathing Framework at 298 K, *Angew. Chem. Int. Ed.* **2016**, *55*, 13271–13275.
6. **Charl X. Bezuidenhout**, Vincent J. Smith, Catharine Esterhuysen* and Leonard J. Barbour*, Solvent and Pressure-Induced Phase Changes in Two 3D Copper Glutarate-Based MOFs via Glutarate (+gauche ⇋ -gauche) Conformational Isomerism, *J. Am. Chem. Soc.* **2017**, *139*, 5923–5929.
7. **Charl X. Bezuidenhout**, Catharine Esterhuysen* and Leonard J. Barbour*, Solvatochromism as a Probe to Observe the Solvent Exchange Process in a 1-D Porous Coordination Polymer with 1-D Solvent Accessible Channels, *Chem Commun.* **2017**, *53*, 5618–5621.
8. Emile R. Engel, Abdelaziz Jouaiti, **Charl X. Bezuidenhout**, Mir Wais Hosseini*, and Leonard J. Barbour*, Activation-dependent breathing in a flexible metal-organic framework and the effects of repeated sorption/desorption cycling, *Angew. Chem. Int. Ed.* **2017**, 56, 1 – 6, 10.1002/anie.201704044.

Conferences

1. **ICCOSS XXIII**: 23rd International Conference on the Chemistry of the Organic Solid State in Stellenbosch, South Africa on 2 - 7 April 2017

   Poster: *Solvent and Pressure-Induced Phase Changes in Two 3D Copper Glutarate-Based MOFs via Glutarate (+gauche ⇋ -gauche) Con-formational Isomerism.*

2. **Indaba 8**: Serendipity vs Prediction, organised by the South African Crystallographic Society, 16-21 August 2015, held in Skukuza, Kruger National Park, South Africa.

   Poster: Pleochroism as a probe to monitor the solvent exchange process in a 1-D metal-organic framework with 1-D solvent accessible channels.

3. **1st meeting on Porous Molecular Solids** in Stellenbosch, South Africa on 9 - 10 April 2015.

   Oral presentation: *Host and guest dynamics Copper Glutarate based metal-organic frameworks (MOFs).*

   Poster: *Pleochroism as a probe to monitor the solvent exchange process in a 1-D metal-organic framework with 1-D solvent accessible channels.*

4. **Indaba 7**: Insights from Structure, organised by the South African Crystallographic Society, September 2012, held in Skukuza, Kruger National Park, South Africa. Poster: *Extreme stability of CO_2 in open channel MOF:* $[Cu_2(\text{glutarate})_2(\textit{trans-bis}(4\text{-pyridyl})\text{ethylene})]_n$.

Abbreviations

1D	1-dimensional
2D	2-dimensional
3D	3-dimensional
MOF	Metal-organic framework
PCP	Porous coordination polymer
SBU	Secondary building unit
np	Narrow-pore
lp	Large-pore
nc	Narrow-channel
wc	Wide-channel
E-ray	Extraordinary ray
O-ray	Ordinary ray
CSD	Cambridge Structural Database
QM	Quantum Mechanics
DFT	Density Functional Theory
MD	Molecular Dynamics
MEP	Molecular Electrostatic Potential
MM	Molecular Mechanics
PQeq	Periodic charge equilibration
Qeq	Molecular charge equilibration method
SCXRD	Single-crystal X-ray diffraction
PXRD	Powder X-ray diffraction
DSC	Differential scanning calorimetry
TGA	Thermogravimetric analysis
H_2glu	Glutaric acid
glu	Glutarate anion
$scCO_2$	Supercritical carbon dioxide

Atomic colour key

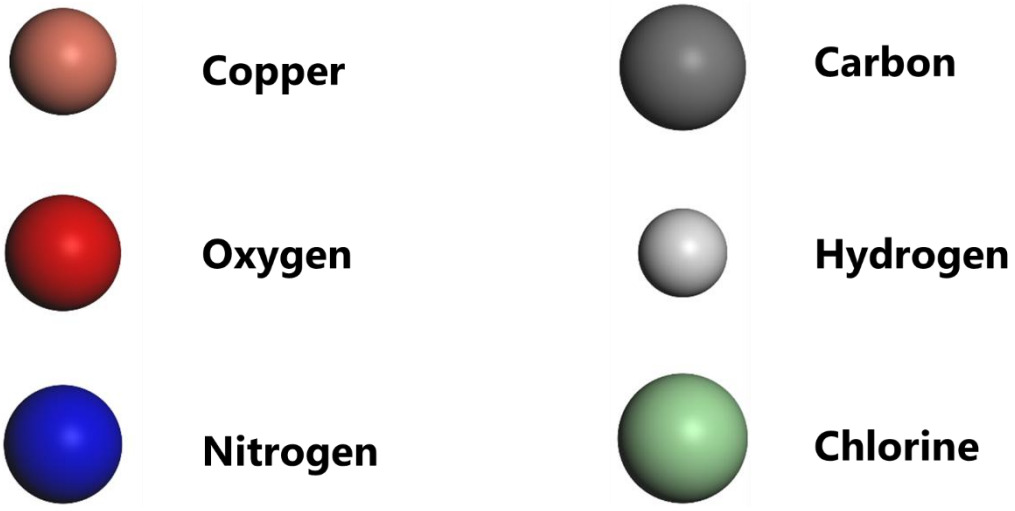

TABLE OF CONTENTS

CHAPTER 1

INTRODUCTION

Porous materials have attracted much attention owing to growing interest in their applications in heterogeneous catalysis, storage and separation.[1] In the 1990s, carbon-based and inorganic materials were the two types of porous materials of general interest, with the most well-known inorganic 3-dimensional crystalline materials being zeolites. Their frameworks contain typically interconnected guest-accessible voids occupied by water molecules and metal ions. Removal of the water molecules from the framework results in a robust and highly porous material.[2] Activated carbons, on the other hand, have a disordered structure with high porosity and high specific surface areas.

These compounds have since been surpassed by a class of materials known as porous coordination polymers (PCPs), which are compounds formed by self-assembly through coordination bonds of metal cations and inorganic or organic ligands to form extended networks with potential guest-accessible space. The first example had, in fact, been discovered in 1897 when Hofmann *et al.* identified a coordination network based on ammonia-nickel cyanide (Hofmann complex). However their study of this and related materials was inhibited by the shortcomings of structural characterisation techniques at the time.[3] In 1949, with the aid of X-ray studies, Powell and Rayner revealed the crystal structure of this Hofmann complex to be an extended 2D framework with benzene solvent molecules trapped within the structure $(Ni(CN)_2(NH_3)\cdot C_6H_6)$.[4] In 1990, Hoskins and Robson reported the first 3D extended coordination assembly with Cu(I) and 4,4',4'',4'''-tetracyanotetraphenylmethane as an organic linker.[5] These framework materials are the earliest forms of PCPs.

PCP research increased greatly in the 1990s due to interest in their regular topologies, high porosity and designable frameworks, yielding early examples of functional microporous materials.[6] A desired extended network assembly can be constructed by reacting certain combinations of metallic nodes or inorganic clusters with multidentate ligands under relatively mild conditions. For instance, Robson *et al.* reported anion exchange using a PCP in 1990[5], while in 1994 Fujita *et al.* reported the catalytic properties of $[Cd(4,4'\text{-bpy})_2]$ (bpy=bipyridine).[7] In 1995, Yaghi *et al.*[8] and Moore *et al.*[9] independently studied the adsorption of aromatic solvent molecules in PCPs, followed by a report by Kitagawa *et al.*'s of gas sorption at ambient temperatures, in 1997.[10] Kitagawa *et al.* summarised the possible framework architectures that could be constructed by combining different connectors (a metal node or metal clusters) and linkers (**Figure 1** – left).[11] As illustrated in **Figure 1**, this strategy allows for the formation of one-, two- and three-dimesional (1D, 2D and 3D) framework architectures.

In 1995 Yaghi *et al.* introduced the term "Metal-Organic Framework" (MOF) to describe a material that consists of organic ligands coordinated to metal-cations yielding a stable

permanently porous framework.[8, 19] It has to be noted that there is little distinction in the definitions of PCPs and MOFs. According to IUPAC guidelines a MOF is an extended coordination network, thus confining it to 2D and 3D frameworks, whereas PCP can be used to describe all three framework dimensionalities.[12] However, in the IUPAC guideline communication, it is noted that PCPs could be based on only inorganic components whereas MOFs must contain organic components as well. In light of this, since the framework materials discussed in this dissertation contain organic components, the term "MOF" will be used to describe 2D and 3D frameworks, whereas PCP will be used to describe 1D coordination polymers.

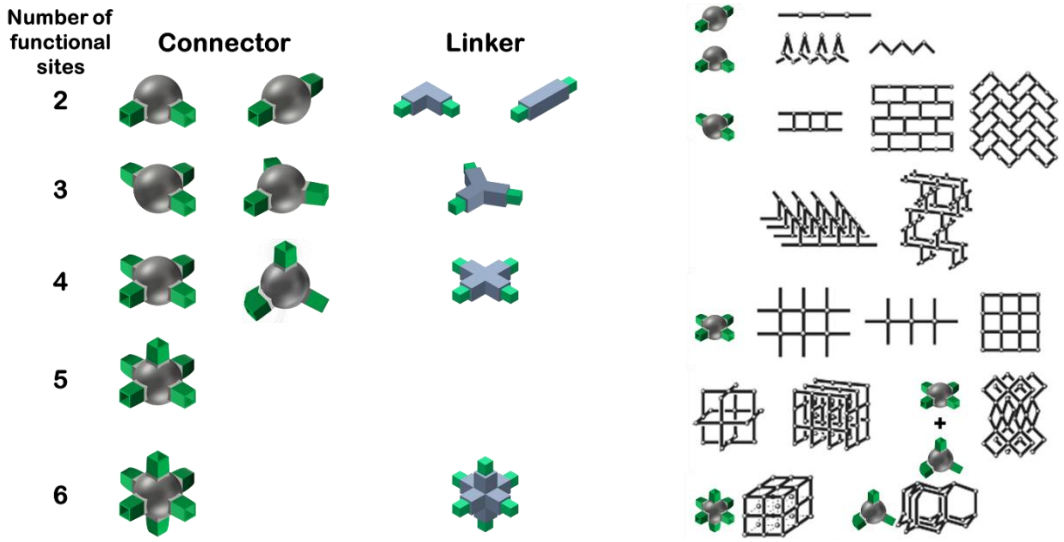

Figure 1. Components of coordination polymers. Possible frameworks that can be assembled using different combinations of connectors and linkers. Figure recreated from Kitagawa *et al.*[11]

1.1. 1D PCPs

1D coordination polymers have attracted considerable interest owing to their electrical, chromic, and gas sorption properties, as well as structural flexibility.[13] The 1D polymeric coordination chains form extended assemblies through directional electrostatic interactions, $\pi \cdots \pi$ interactions and close packing van der Waals interactions.[14-15] The simplicity of PCP topologies allows for easy modification of their structures through the choice of metal centers and organic linkers. This enables 1D coordination polymers to adopt various types of architectures such as linear chains, zigzag chains, ladders, ribbons, etc. (**Figure 1** - right).[11] 1D coordination polymers often form close-packed structures. However, porous structures can be formed as a result of appropriate structure-directing interactions.[16] In 2002 Takamizawa *et al.* prepared an empty single-crystal host, $[Rh(II)_2(O_2CPh)_4(pyz)]_n$ (**Figure 2 (a)** and **(b)**), and established its porosity through nitrogen adsorption,[17] and later its carbon dioxide (CO_2) adsorption capabilities.[18] The later result was accompanied by the structural visualization of the CO_2 host-guest adduct obtained by single crystal X-ray diffraction (SCXRD) under CO_2 atmosphere at 93 K (**Figure 2 (c)**). The empty host was shown to have insufficient void space to accommodate the CO_2 molecules, and had thus undergone a phase change upon CO_2 adsorption in order to accommodate the guest molecules.

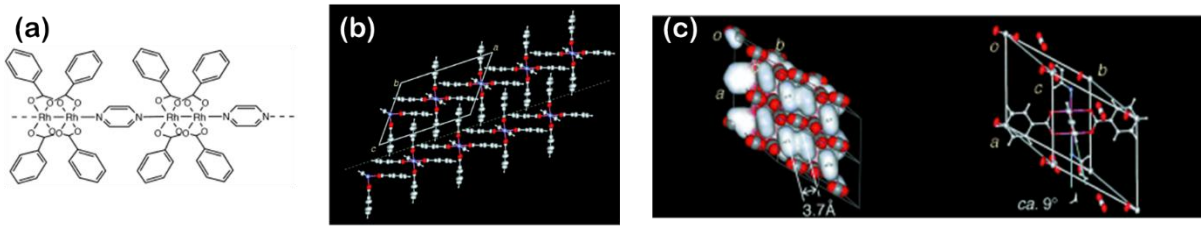

Figure 2. (a) Schematic of $[Rh(II)_2(O_2CPh)_4(pyz)]_n$ (b) The close packed structure of the empty host. (c) The CO_2 host-guest adduct. Figures taken from Takamizawa *et al.*[18]

1.2. METAL-ORGANIC FRAMEWORKS (MOFS)

Although MOF research did not attract much initial interest, the discovery of the remarkably stable and highly porous tetra nuclear zinc-carboxylate MOF by Li *et al.* in 1999 highlighted the potential of MOFs for applications such as gas storage.[19] This sparked a rapid increase in MOF-related research, leading to a highly active area of study.[11, 20-24] In 2000, based on their work on MOF-5, Eddaoudi *et al.* synthesised three MOFs using zinc(II) cations combined with terephthalate and trimesate linkers (**Figure 3**).[25] The porosity of the MOFs was demonstrated by ethanol vapour sorption, and it was suggested that the unsaturated zinc metal site in the $Zn_2(BTC)(NO_3)$ framework (MOF-4) could be useful for catalysis.

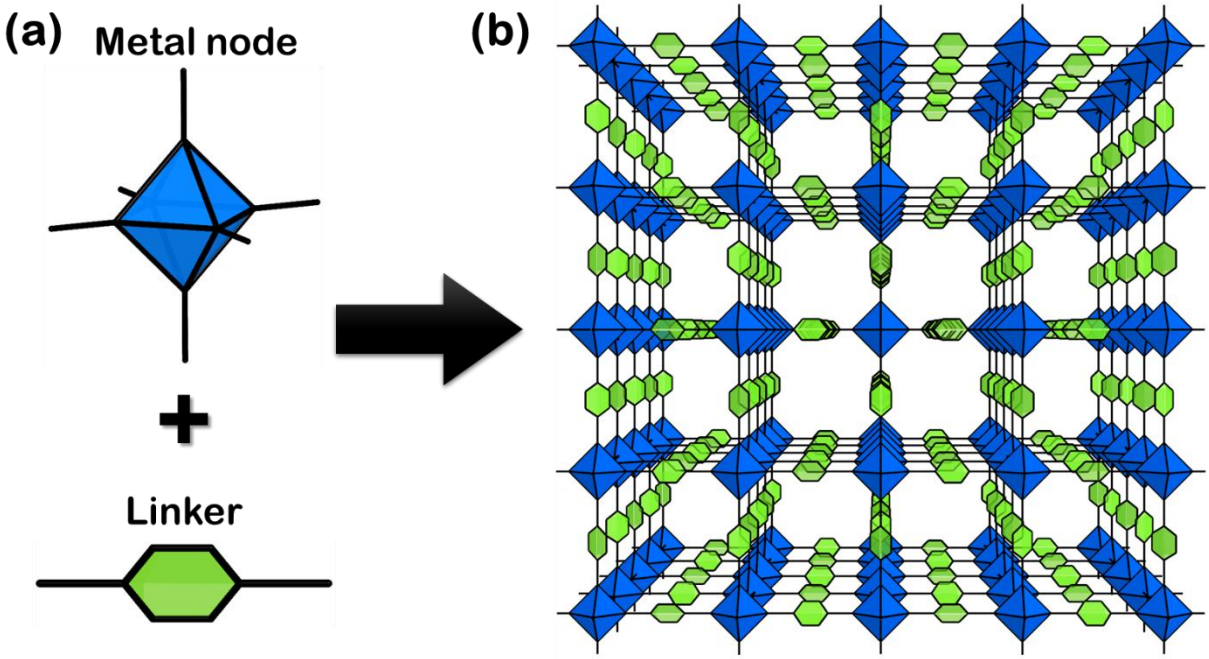

Figure 3. Schematic representation for the basic concept behind MOF framework assemblies using the MOF-5 crystal structure as an example. (a) The components of a MOF framework. (b) A typical framework that can be formed using these components.

1.2.1. Synthesis of MOFs

Part of the appeal of MOFs is the diversity of synthetic methods that can be employed, which hold the possibility of obtaining a large variety of interesting structures and structural phases (even with the same metals and ligands).[23] Furthermore, the characteristics of the material, such as crystal size or shape, thin films, membranes, etc., are greatly affected by the employed method of synthesis.[21, 24] Conventional methods for synthesising MOFs include room temperature mixing, conventional electric heating and solvothermal methods. In recent years alternative synthetic routes have been explored such as microwave heating, electrochemical, mechanochemical, and sonochemical methods. **Figure 4** provides an overview of the synthetic methods used for MOFs, as well as the temperature regime of each. The two most used methods are hydrothermal- or solvothermal- and microwave-assisted synthesis:

- Hydrothermal or solvothermal: *Synthesis using solvents such as water (hydrothermal) or dimethylformamide (solvothermal). These solvent also act as a reagent at elevated temperature to deprotonate the carboxylic acid groups of the ligands used. According to the definition given by Rabenau, solvatothermal reactions "take place in closed vessels under autogenous pressure above the boiling point of the solvent".* [26]
- Microwave-assisted synthesis: *This method utilises the interaction of electromagnetic waves with polar species in a solution or electrons/ions in a solid as a very energy efficient homogeneous method of heating.*

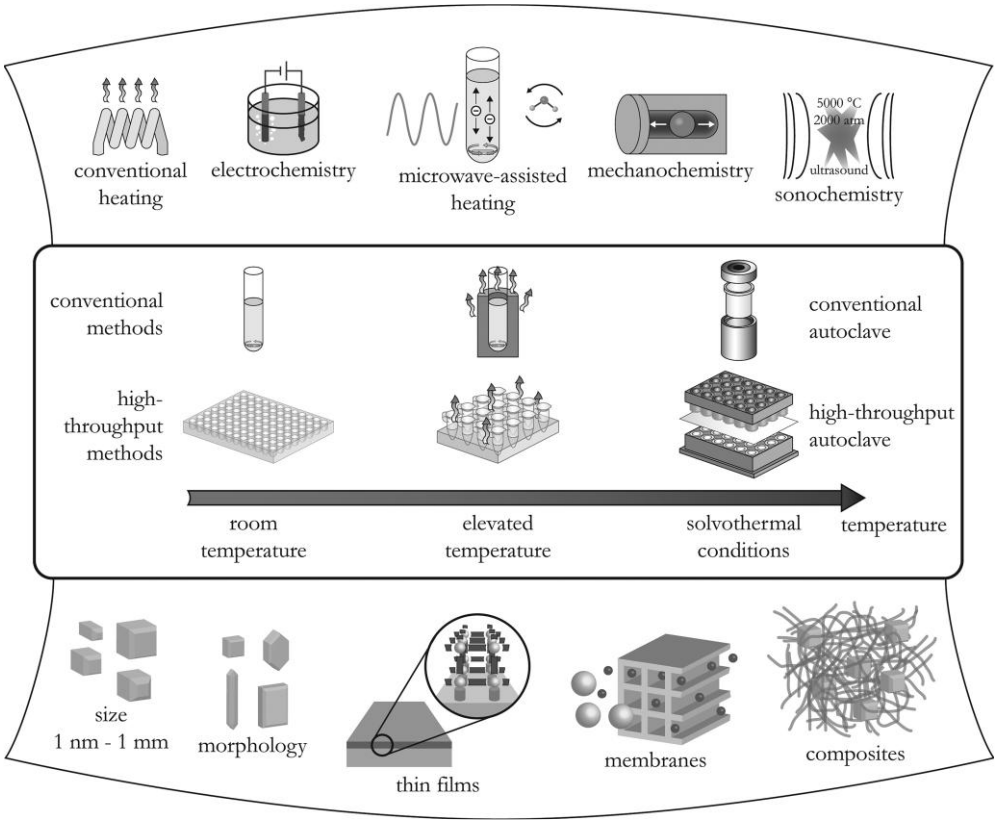

Figure 4. An overview of synthesis methods in the preparation of MOFs. Figure taken from Stock et al.[24]

1.2.2. Secondary building units (SBUs)

Research has progressed towards a modular approach in the synthesis and design of new MOFs. The realisation of reoccurring metal cluster motifs and framework architecture in MOFs led to the term "secondary building units" (SBUs) as a way of describing these motifs (**Figure 5**).[27] The underlying topology of MOF structures can also be classified based on the SBUs employed. Most SBUs are built from metal-carboxylate clusters owing to the predominant use of rigid aromatic polydentate carboxylic acids as linkers in the exploration for new MOFs.[20, 23, 25, 28-30] **Figure 5** shows some of the most common metal-carboxylate SBUs, which may be combined with different linker geometries to afford a wide range 3D architectures. A more comprehensive catalogue of these MOF SBUs was reported by Tranchemontagne *et al.* in a review in 2009.[31] It should be noted that the term "linker" describes a ligand that participates in the coordination assembly of a MOF and should not be confused with uncoordinated ligands located within the MOF structure. Thus, all linkers are ligands, but all ligands need not be linkers.

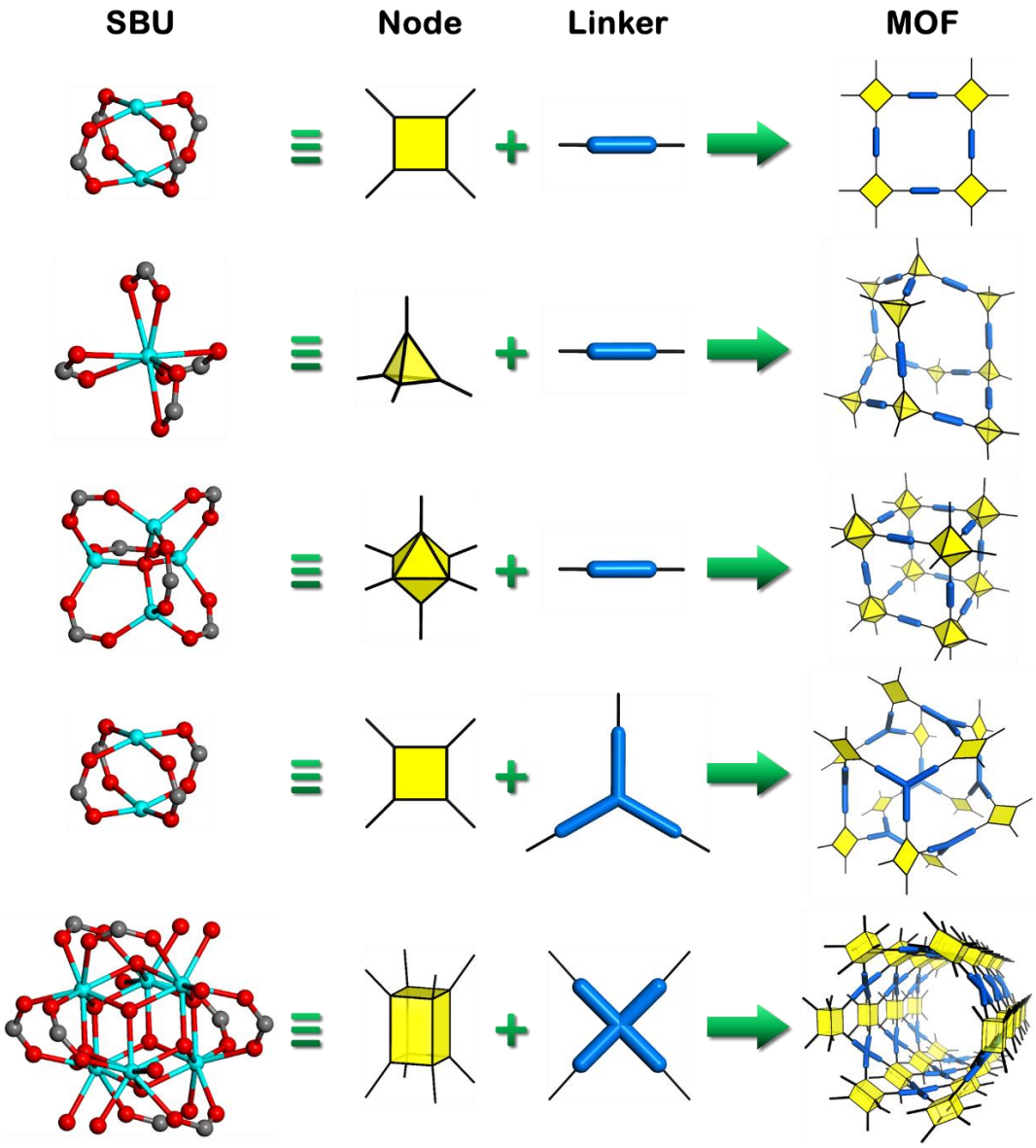

Figure 5. Schematic illustration of the construction of MOFs from SBUs and rigid linkers.[32]

1.2.3. Ligand design for isoreticular synthesis of MOFs

Using the concept of SBUs researchers were able to reproduce certain MOF architectures and topologies by replacing the organic ligands with those containing a modified spacer. The spacer in a ligand is generally a synthetically inert part of the ligand with respect to MOF synthesis, but can alter the functional properties of the material. MOFs produced using this method that possess the same network topology are referred to as "isoreticular".[33] The isoreticular series based on MOF-5, reported by Eddaoudi *et al.*,[28] are prime examples of such MOFs and are referred to as IRMOFs (isoreticular MOFs, **Figure 6**). This series shows a systematic increase in pore volume through lengthening of the spacer in the organic dicarboxylate linker, as well as functionalisation of the pores by adding side groups (–Br, $–NH_2$, etc.) to the spacer. This approach allows tuning of properties such as sorption capacity and selectivity.[32] In addition, such isoreticular series are useful platforms for the systematic study of the properties of MOFs.[34-37]

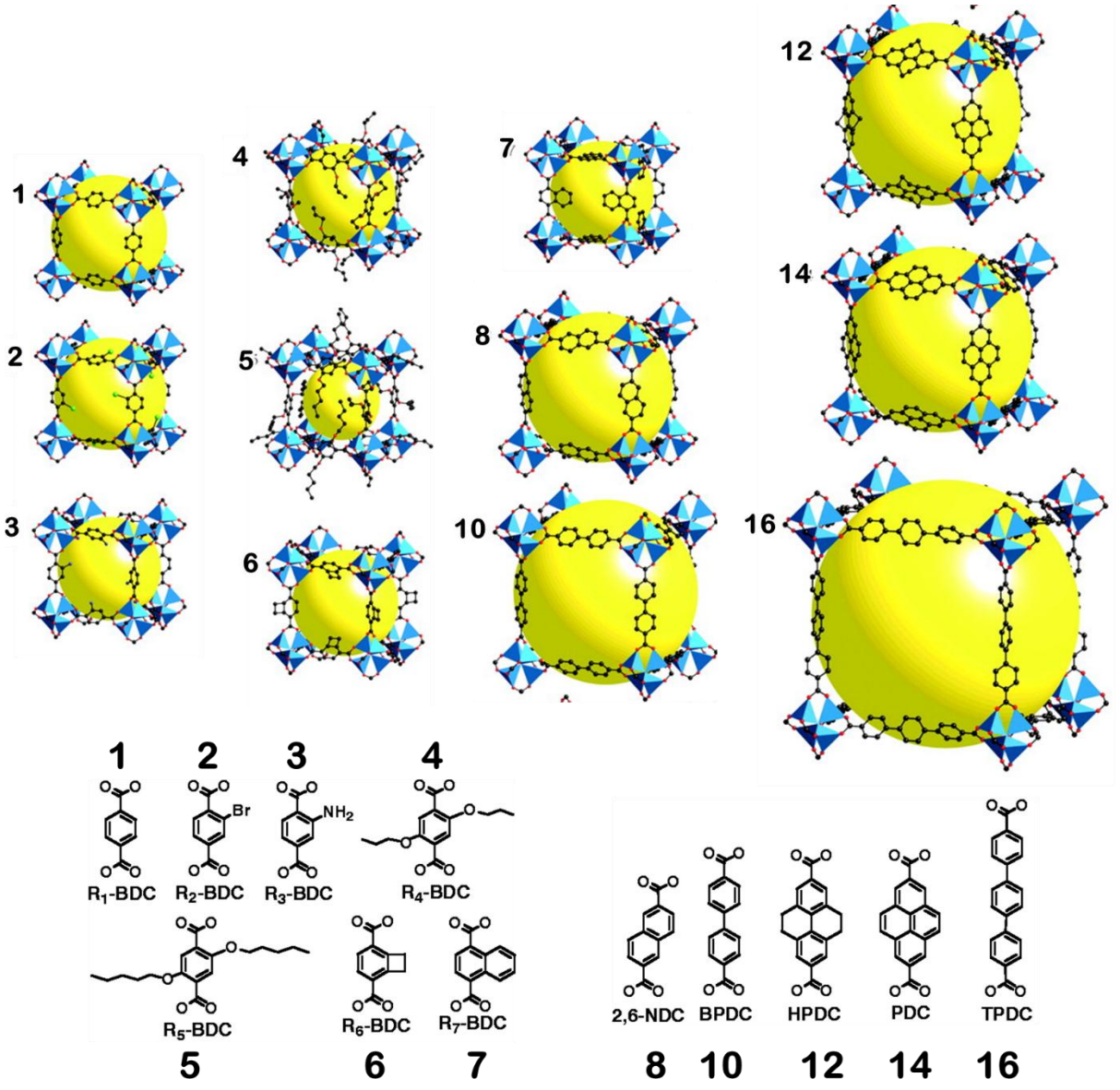

Figure 6. The isoreticular doubly-interpenetrated IRMOFs. The change in the MOF cavity size is indicated by the large yellow spheres. Figure taken from Eddaoudi *et al.*[28]

1.2.4. Porosity

A material is considered porous if it contains voids within its structure that could be occupied by guest molecules. To prove that a material is porous, permeability specific to a host phase should be demonstrated.[38] The degree of porosity can be established experimentally by determining the surface area of a material, generally applying BET (Brunauer-Emmett-Teller) theory to nitrogen sorption data measured at 77 K.[39] However, this only demonstrates the permeability of the material with respect to nitrogen and does not guarantee the adsorption of other guests. From this perspective, a material could have voids within its structure without being porous, or it could be only be porous towards selected guests. Kitagawa *et al.* categorised porosity based on the spatial dimensions of the voids (**Figure 7**).[11] Zero-dimensional pores are isolated within the host framework. One-dimensional porosity refers to non-intersecting channels, while two-dimensional porosity exists in assemblies of separate layers. Three-dimensional porosity constitutes a system of intersecting channels.

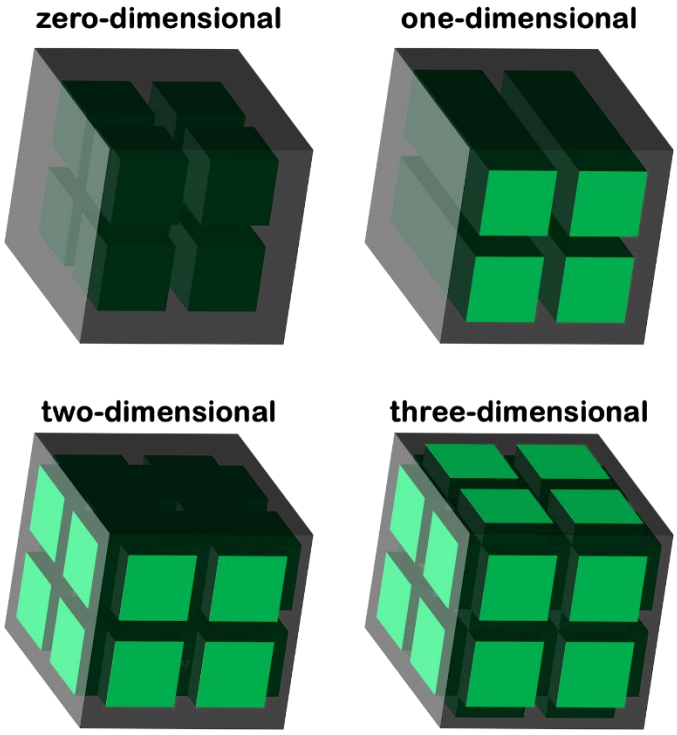

Figure 7. The four categories for the dimensionality of porosity in MOFs/PCPs: 0D, 1D, 2D and 3D porosity. Figure recreated from Kitagawa *et al.*[11]

1.2.5. Gas sorption

Sorption capacity is influenced by three factors: (i) the molecular sieving effect, which is based on a size/shape exclusion principle, (ii) the thermodynamic effect, which results from preferential packing of gas molecules in the pores of the host, the channel topology and the surface interactions between gas molecules and the channel walls, and (iii) the kinetic effect, resulting from different gases having different kinetic diameters and energies, which in turn leads to variation in diffusion rates. Together, these factors contribute to the characteristic isotherms associated with sorption; in this regard the IUPAC has classified six typical sorption isotherms (**Figure 8 (a)**).[40-41] The Type I isotherm is usually associated with microporous

frameworks, Types II, III and VI with non-, meso- or macroporous materials, and Types IV and V exclusively with mesoporosity. According to Fletcher *et al.*[42] the shapes of the isotherms are influenced by pore size, host-guest and guest-guest interactions. Moreover, the shapes of the isotherms for rigid frameworks are greatly influenced by electrostatic interactions, which can produce artifacts (e.g. adsorption hysteresis and stepped isotherms) similar to those induced by framework flexibility.[43]

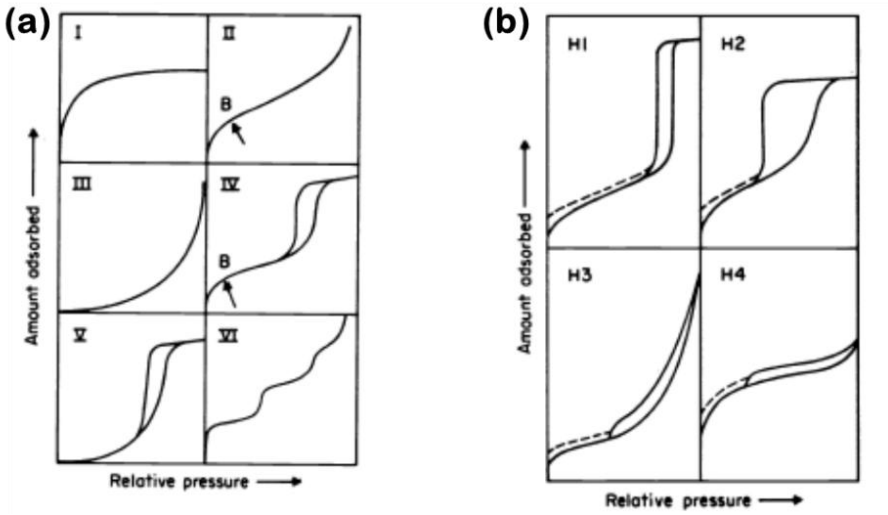

Figure 8. (a) Types of physisorption isotherms. (b) The four typical hysteretic isotherms.[40-41, 44]

Adsorption hysteresis occurs when the sorption and desorption isotherms do not overlap, and may result from intrinsic framework flexibility, a phase transition, capillary condensation or gas trapping within the pore apertures.[45] Sorption isotherms that display hysteresis can be classified into several categories, as shown in **Figure 8 (b)**: extreme (H1 and H4) and intermediate (H2 and H3). In H1 the hysteretic sorption and desorption isotherms are close to vertical and almost parallel to each other (**Figure 9 (a)**) while in H4 they are close to horizontal and almost parallel. Types H2 (**Figure 9 (b)**) and H3 have shapes that fall between those of H1 and H4.[44] Sorption hysteresis can be exploited in various applications such as storage where the materials are filled at a high gas pressure and then stored at a lower pressure while still maintaining a high gas loading.[45] This is a result of the difference in loadings involved in the adsorption and desorption processes at particular pressures, as determined by sorption analysis (**Figure 9 (b)**).

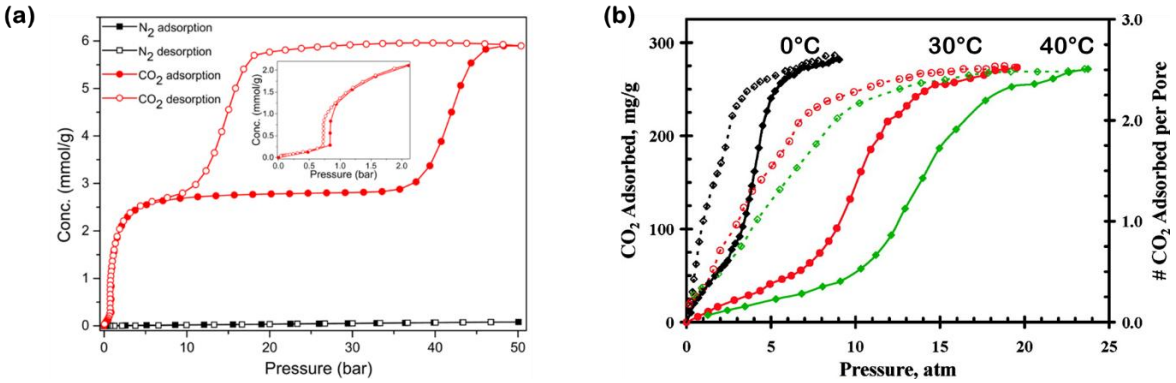

Figure 9. Examples of experimental hysteretic CO_2 sorption. (a) Zn(terephthalate)(1,2,3-triazolate) at 25 °C,[46] and (b) [Ni(1,2-bis(4-pyridyl)ethylene)][Ni(CN)$_4$] at different temperatures.[45]

1.2.6. Flexible MOFs

Flexible MOFs or 'soft porous crystals' are materials that respond dynamically to stimuli such as pressure, atmospheric vapour or gas pressure, changes in temperature, and electromagnetic radiation.[47] In 2005, Kitagawa *et al.* classified these materials under three categories: first, second and third generation based on the framework response to guest removal (**Figure 10**).[48] The first generation compounds collapse and lose all structural integrity when the guest is removed. The second generation materials are permanently porous, usually rigid frameworks. The third generation[49] compounds are soft porous crystals that undergo reversible transformations upon guest removal, uptake or exchange. In 2009, Kitagawa *et al.* updated their definition to state that "*at least one crystal phase possesses space that can be occupied by guest molecules, so that the framework exhibits reproducible guest adsorption*".[50]

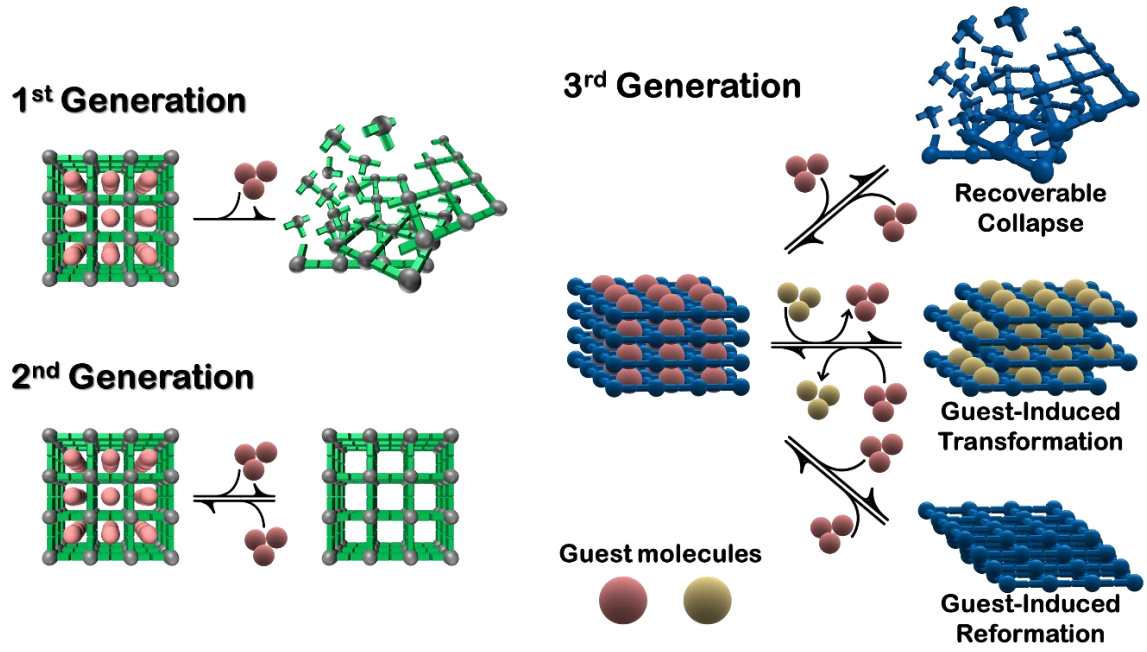

Figure 10. Schematic representation of first, second and third generation porous coordination polymers as described by Kitagawa *et al.*[48-49, 51]

Schneemann *et al.*[52] summarised the different modes of flexibility in MOF structures (**Figure 11**). These include breathing, swelling, linker rotation and subnetwork displacement. Often such changes lead to distinct phases, a narrow-pore (np) and a large-pore (lp) phase. The sorption properties of the materials is greatly affected by this kind of flexibility and can produce steps (gate-opening) in the sorption isotherm at particular pressures for certain gases.[46] This gate-opening step occurs upon transformation of the MOF from the np to the lp phase. The MIL-53(M) ([M(1,4-benzenedicarboxylate)(OH)]$_n$ where M = Al, Fe, Cr, Sc, Ga, In) series are typical examples of breathing flexibility (**Figure 12 (a)** and **(b)**).[53-54] Lama *et al.* reported linker rotation of both ligands in the MOF [Zn(terephthalate)(1,2,3-triazolate)]$_n$ upon sorption of CO_2 at high pressures (**Figure 12 (c)** and **(d)**).[46] Other types of np/lp transformations include conformational isomerism of the organic ligands by irradiation with light[55] or temperature[56] and breaking/reformation of metal-ligand coordination bonds.[47] The terms narrow-pore and large-pore are generic terms pertaining to all dimensionalities of porosity. However, in work presented in this dissertation, we use the terms narrow-channel (nc) and wide-channel (wc), which are more specific to 1D porosity (i.e. channels).

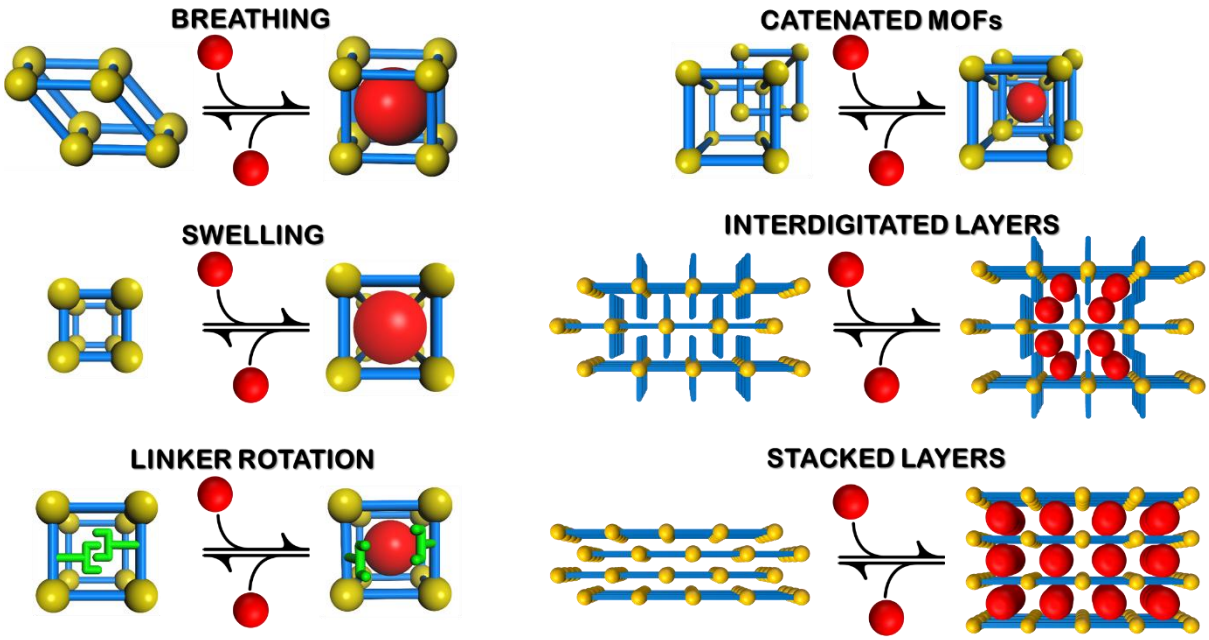

Figure 11. The classification of different modes of flexibility in MOFs. Figure recreated from Schneemann *et al.*[52]

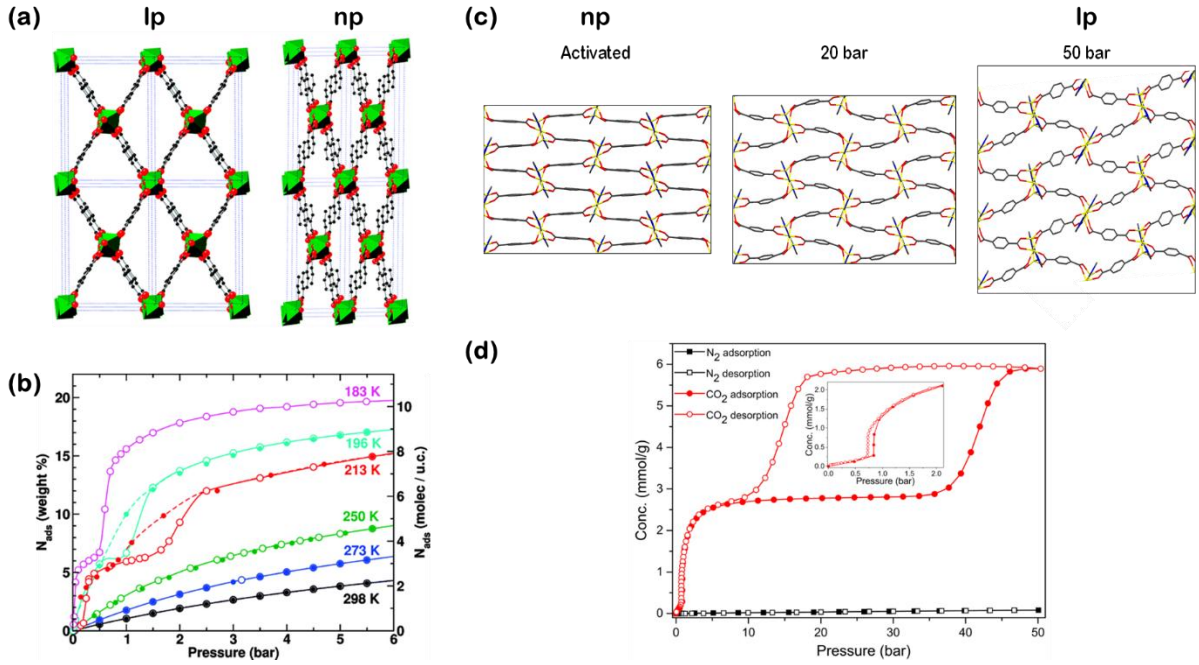

Figure 12. (a) The MIL-53(Al) metastable lp and np structures. (b) The methane sorption isotherms for MIL-53(Al) collected between 183 and 298 K.[54] (c) The metastable lp and np structures of [Zn(terephthalate)(1,2,3-triazolate)]$_n$ under increasing CO_2 pressure. (d) The corresponding CO_2 sorption isotherm collected at 298 K.[46]

1.2.7. Solvatochromism in MOFs and PCPs

Solvatochromism is the propensity of a compound or material to change colour when exposed to a different solvent. This property was first studied for organic dye molecules in solution using UV-vis absorption spectroscopy. The first systematic study of solvatochromism was

carried out by Kosower in 1958 as a means to probe solvent polarity.[57] Recognizing MOFs and PCPs as versatile platforms for hybrid-organic materials, researchers have sought to incorporate the properties of organic dyes and chromophores into porous materials.[58] In MOFs, solvatochromism generally originates from *d-d* transitions of metal centres undergoing a change in their coordination sphere.[59-60] This is usually accompanied by large structural changes in the framework that can lead to deterioration of the material.[61-63] A shift in the *d-d* absorption of the metal can also be induced through interaction of guest molecules with the organic ligands, which in turn affects the electronic structure of the metal.[64] As a result, effort has gone into generating MOFs with stable pores upon guest exchange and with chromophores as organic linkers forming the walls of the pores. Building this property into a MOF can turn the material into a functioning small-molecule sensor. A prime example of a MOF-based small-molecule sensor, shown in **Figure 13**, contains stable pores with the channel walls comprising hydrogen-bonded solvatochromic tetrazine-based bipyridyl ligands (**Figure 13 (a)**). **Figure 13 (b)** shows the large visible colour difference for each solvate.[65]

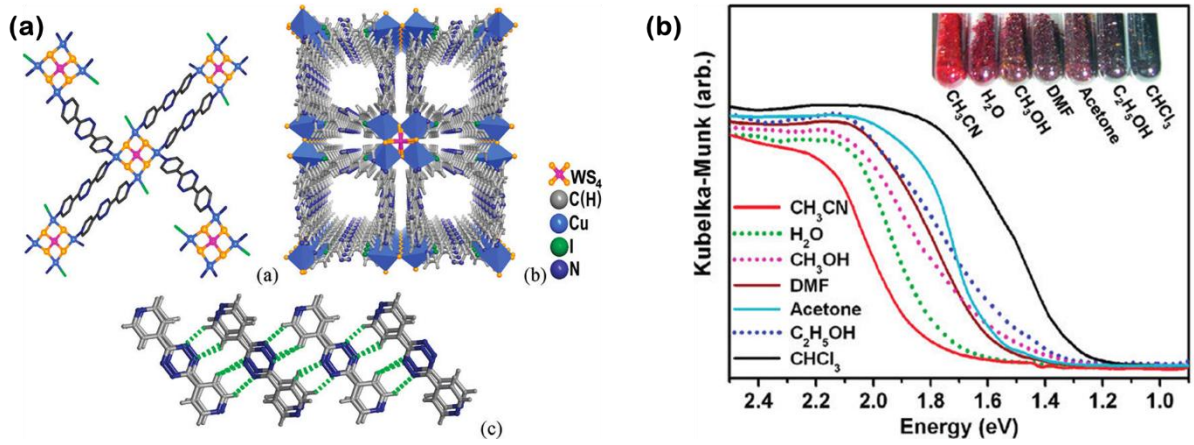

Figure 13. (a) Structure of a nanotubular MOF. (b) Photograph of different inclusion compounds showing considerable changes in colour. Figure taken from Zhen-Zhong Lu *et al.*[65]

1.3. PLEOCHROISM

Double refraction (birefringence)[66] is the division of a beam of light into two rays (two principal vibrations) when it passes through an anisotropic material (**Figure 14 (a)**): an ordinary ray (O-ray) and an extraordinary ray (E-ray). These mutually perpendicular principal vibrations are oriented perpendicular to the direction in which the waves propagate. The paths of the two rays diverge as they travel through the crystal, thus resulting in different path lengths. Since the rays follow different path lengths through the anisotropic material the extent of their absorption by the material may be different (seen as different intensities, **Figure 14. (b)**). By using a polariser and a calcite crystal, the mutually perpendicular nature of the split ray can be observed visually (**Figure 14 (b)**).[67] When the crystal is coloured, the O- and E-rays have specific frequencies. Owing to the different rates of absorption of the two rays, the crystal then appears to have different colours when viewed from different angles (the pathways of the two rays change giving rise to pleochroism). Rotating the crystal relative to a polariser has the effect of selecting which ray may pass through, thus changing the colour of the crystal upon

rotation (**Figure 14. (c)**). Polarised light also enhances the saturation of the observed colours. This makes polarised light microscopy ideal for observing pleochroism.[68]

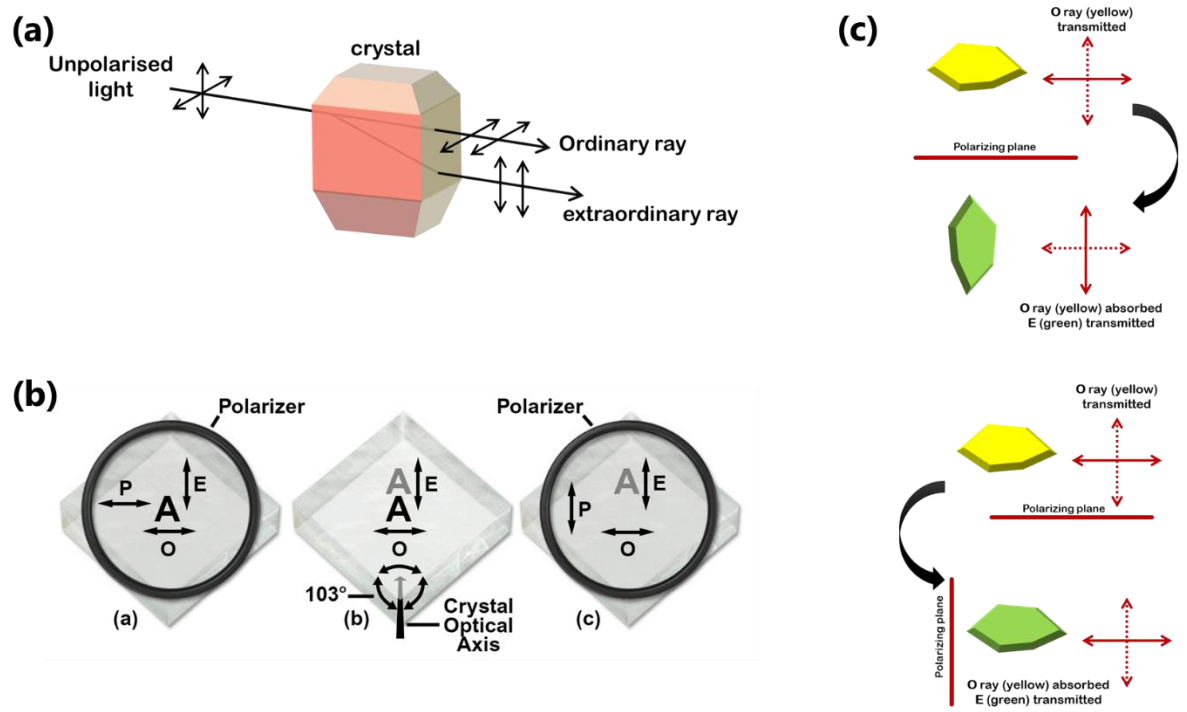

Figure 14. (a) Schematic principles of birefringence. (b) Electric vector orientations of a birefringent calcite crystal. The P denotes the polarising plane, E denotes the extraordinary ray and O the ordinary ray.[67] (c) Illustration of how birefringence can lead to pleochroism.

1.4. COMPUTATIONAL METHODOLOGIES AND APPROACHES IN MATERIAL SCIENCE.

In the field of materials science, important fundamental insight can be obtained regarding the properties of materials by applying quantum-mechanical (QM) methods. In this regard density functional theory (DFT) is the most cost effective method as compared to wave function-based coupled-cluster and perturbation methods.[69] The latter are computationally very demanding for large systems, which cannot always be avoided when studying materials such as MOFs. Furthermore, the development of efficient periodic DFT methods has greatly reduced the computational cost for calculating large unit cells with heavy metal atoms such as MOF systems.[69-70] Simulation of these systems at an atomistic or molecular level provides sub-microscopic insight that is experimentally inaccessible, and reveals the underlying physics.[71] In addition, it can be used to validate the interpretation of experimental observations as well as to establish the structure-property relationship.[72] When it comes to simulating properties that requires multi-unit-cell models, molecular dynamics (MD) and molecular mechanics (MM) simulation are the only option.[71, 73] These methods, parameterised using experimental and QM methods,[74-75] have been successfully utilised for the prediction of possible structures and determination of properties (such as sorption) for MOFs.[76-77] When used in conjunction with high resolution powder diffraction measurements, it is possible to determine the actual crystal structure of the MOF.[78-79]

1.4.1. DFT for periodic systems

DFT approximates a solution for the many-electron Schrödinger equation for calculating the ground state energy of a system. DFT uses electron density ($\rho(\vec{r})$), which is the central quantity in the method, to determine the energy of a system. A key assumption in DFT that the ground state of the system (E_0) is connected to the electron density for which the energy is minimised under the constraint that the total number of electrons represented by $\rho(\vec{r})$ remains constant. This means that it is possible to have numerous $\rho(\vec{r})$ configurations for a certain system. Thus, DFT uses an iterative process, also known as the self-consistent field (SCF) procedure, to search for a $\rho(\vec{r})$ configuration that yields E_0.[80]

When attempting to apply DFT to periodic systems some difficulties must be overcome. Electronic wavefunctions extend over the entire solid and consequently require an infinite basis set to expand each wavefunction. This can be overcome by applying Bloch's theorem to the cell-periodic part of the electronic wavefunctions when conducting calculations involving periodic systems. The Bloch theorem allows for the expansion of the electronic wavefunctions in terms of a distinct set of plane waves with wave vectors that are reciprocal lattice vectors of the crystal.[81] Plane-wave basis sets can be truncated by introducing a cut-off for the kinetic energy that only includes plane waves with kinetic energies less than a particular value. Plane waves with small kinetic energies are generally more significant than those with large kinetic energies. This results in the construction of a finite basis set that significantly reduces the computational load. The plane-wave method is efficient for *ab initio* MD and uses the same basis set for molecules and solids (unlike Gaussian basis sets).[82] Calculating stresses and forces are computationally cheap in this approach, leading to efficient geometry optimisation and molecular dynamics schemes. The main computational task in plane-wave electronic calculations is fast calculation of Fourier transforms. It is an efficient way of transforming various entities such as wavefunctions, potentials and search directions from real to reciprocal space and back, which reduces the overall computational cost.[83-84]

Pseudopotentials are required for the plane-wave method to be efficient. The basis sets for these pseudo wavefunctions are reasonably small owing to the absence of nodes inside the core regions (not "all-electron", *i.e.* frozen core). The core region is approximated by using a weaker pseudopotential that acts on a set of pseudo wavefunctions. The application of these concepts is particularly useful for describing chemical bonding.[85-86]

The quantum mechanical (QM) DFT-based code CASTEP in the Materials Studio software[87] suite utilises a plane wave basis-set approach and several methods to handle pseudopotentials. All calculations in CASTEP must be performed on a periodic system since the code is based on a supercell method. This code has local (LDA) and gradient-corrected (GGA) exchange-correlation functionals available. Materials Studio also incorporates the semi-empirical dispersion-correction schemes put forth by Grimme (2006, DFT-D2),[88] Jurecka *et al.* (2007),[89] Ortmann, Bechstedt and Schmidt (2006, OBS) and by Tkatchenko and Scheffler (2009, TS).[90] CASTEP has been successfully applied to MOFs for the study of various properties such chemical bonding,[91] guest-binding,[92] gate-opening,[93] adsorption,[94-96] to name a few.

1.4.2. Molecular electrostatic potential (MEP) mapping

The molecular electrostatic potential ($V(\boldsymbol{r})$) is a well-established and highly useful tool for the study of molecular properties and noncovalent interactions between molecules.[97] The electrostatic potential is derived, as a classical Coulombic interaction using atomic monopoles, from the electron density and nuclear charges as described by Eq. 1:

$$V(\boldsymbol{r}) = \sum_{A} \frac{\mathrm{Z}_A}{|\boldsymbol{R}_A - \boldsymbol{r}|} - \int \frac{\rho(\boldsymbol{r}')d\boldsymbol{r}'}{|\boldsymbol{r}' - \boldsymbol{r}|} \qquad \textit{Eq. 1}$$

where Z_A is the charge on nucleus A, located at $\boldsymbol{R}_A$, and $\rho(\boldsymbol{r})$ is the molecule's electron density. $V(\boldsymbol{r})$ is the interaction energy between the system and a unit positive point charge at $\boldsymbol{r}$ and it is typically expressed in units of energy. $V(\boldsymbol{r})$ is a three-dimensional function that can be evaluated at any point $\boldsymbol{r}$ within the system, with the exception of at the nuclei ($\boldsymbol{R}_A \neq \boldsymbol{r}, Eq.1$).[98] These results can be mapped onto 2D planes (slices though the system under investigation) or 3D surfaces of molecules at a particular electron density contour, depending on the relevance and aspect of interest.[99] The contour utilised for the 3D surface can be defined arbitrarily, which may lead to ambiguity in the analysis of the results. In this work we use the 0.0015 e^-/Bohr^3 (0.01 e^-/Å^3) outer contour of the molecule's electron density ($\rho(\boldsymbol{r})$) as suggested by Bader et al.[100-101] This contour contains 95-98% of a molecule's electron density and 97% of a molecule's electronic charge.[102] Of the various representations of MEPs, the most common are 2D and 3D contour maps.[71] The VAMP module[103] of the Materials Studio software package provides high quality molecular electrostatic potentials (MEPs) a great deal faster than comparable methods.[104] This code utilises a choice of standard semi-empirical Hamiltonian methods, four NDDO Hamiltonians and four ZINDO Hamiltonians. Amongst these Hamiltonians NDDO-AM1* is parameterised for systems containing transition metals thus making it suitable for the study of MOFs.[105-107]

1.4.3. Molecular mechanics (MM).

QM theory is generally employed for accurate simulation of atomic and molecular systems. However, owing to their computational expense, QM techniques are typically only applied to small systems comprising fewer than 100 atoms. Alternative more practical methodologies are required for modelling large systems such as condensed polymers and crystal structures with large unit cells.[108] The goal in simulating large systems is predominantly to extract bulk (statistical) properties such as adsorption isotherms, which mainly depend on the position or average configurations of the atomic nuclei.[73, 109] MM makes use of forcefields (potentials), an empirical fit to the potential energy surface, to perform such calculations. Classical simulation methods provide a number of forcefields and distribution generating techniques which generate configurations by integrating the Newtonian (classical) equations of motion. The solution of these equations is called molecular dynamics (MD).[110] Since using QM to perform MD simulations is computationally very expensive, forcefield methods are more frequently employed for the treatment of large systems. MM focuses on finding static time-independent properties such as equilibrium structures, relative energies, harmonic vibrational frequencies and transition states, and essentially provides a snapshot of the system. MM allows for cheap exploration of large configurational spaces of a system in order to accomplish tasks such as

conformational searches (quench dynamics) and potential energy surface scans for very large systems.

1.4.4. Forcefields

A crucial part of any MD or MM simulation is the choice of forcefield. The forcefield is an approximate description of the potential energy hypersurface on which the atomic nuclei move. The utility of a forcefield is its description of the potential energy surface for very large systems with reasonable accuracy. Forcefields are parameterised using empirical data of a small set of models and extrapolates to larger sets of related models.[110] Forcefields are usually tuned (parameterised) for particular groups of systems and therefore the choice of forcefield depends on the type of structure being investigated. The most common forcefields in use include pcff, COMPASS (a new version of pcff), cvff, Dreiding and Universal.[111] Forcefields can reproduce experimental parameters such as crystal structures, sublimation energies and vibrational frequencies depending on their "*fitness*" (quality of the forcefield parameterisation) and therefore has quantum effects empirically included.[112-115] Recently, for hybrid materials such as MOFs, there has been successful forcefield development derived from electronic structure calculations for application in gas adsorption and transport studies.[116] However, there are chemical reactions and physical processes that are not well defined for a mechanical approach and they should always be considered.

The areas were forcefield methods cannot be used successfully are:

- Proton transfer (acid/base reactions)
- Electronic transitions (photon absorption)
- Electron transport phenomena etc.

The advantages of forcefield methods are:

- The simulation costs of forcefield-based simulations are exceedingly lower (and faster) than QM-based calculations, which allows them to handle large systems for utilisation in the study of condensed-phase molecules, macromolecules, crystal structures, etc.[117]
- The energy can be decomposes into the contributions of the bond stretching, angle deformations, non-bonding energies, etc. The non-bonding energies can be further partitioned into its coulombic and van der Waals components.

1.4.5. Atomic partial charge calculation

The contributions of long-range electrostatic intermolecular interactions are often dominant in systems such as MOFs and have to be considered in the application of computational methods. Since Coulombic interactions decrease at a slow rate with respect to distance ($^1/_{\boldsymbol{r}}$), their contribution to the interaction energy is not negligible, even at substantial distances. It is therefore important to assign the proper atomic charges, as electrostatic interactions are crucial in determining the packing and structures of organic and inorganic systems. However, the precise nature of the variation in electrostatic interaction energy with distance depends on

the structure of the material. The electrostatic potentials of MOFs are often represented by assigning partial charges on the framework atoms, which provides both computational accuracy and efficiency. Some of the typical methods for determining partial charges used in MOF studies are summarised below.

- Mulliken Population Analysis.

  This is a means of estimating partial atomic charges from calculations that use methods based on the linear combination of atomic orbitals (LCAO) molecular orbital approach.[118] DFT calculations performed on periodic structures of MOFs utilise a plane-wave basis set, which provides no information regarding the localisation of the electrons in the system. The technique described by Sanchez-Portal *et al.* is used to project the plane-wave states onto a localized basis in order to implement population analysis. This method is used in the plane wave calculations employed by the CASTEP code running in the Materials Studio software package for periodic models.[119-120]

- ESP charges

  Cluster-Based Quantum Mechanics are used to obtained electrostatic potential (ESP) derived charges from single-point energy DFT calculations implemented on representative clusters of a MOF. The unsaturated atoms and bonds within the models that exist due to "abbreviating" the framework are corrected using moieties such as methyl groups or hydrogen atoms.[121-122]

- Molecular Charge Equilibration Method (QEq).

  The basic idea of charge equilibration (QEq) is the prediction of the charges and their distribution based on experimental atomic properties and the geometry of the system.[123] This method is mainly used in the application of fast and reasonable high-throughput MOF screening.[124-125]

- Periodic Charge Equilibration Method (PQEq).

  PQEq is an extension of QEq that includes the effect of a lattice on the charge distribution. This method only requires the unit cell content and dimensions.[126]

1.5. AIMS

Owing to the versatility of MOF synthesis and applications, there has been a large increase in the number of MOF structures that have been deposited in the Cambridge Structural Database (CSD).[127] In general, the focus in MOF research has been to produce very high porosity for applications such as sorption. However, this has led to a large number of unexplored materials in the literature and the CSD. Using the CSD we aimed to obtain MOFs with structural similarities (such as isoreticular frameworks) that could be used as platforms for the systematic study of host-guest dynamics. Using a range of complementary experimental and computational methods we sought to systematically target some fundamental aspects of the host-guest dynamics in MOFs, as well as the structure-property relationships of these materials. We opted for five copper-glutarate-based MOFs that form an isoreticular series in which only the bipyridyl ligands are substituted. These MOFs were separated in two groups for study: three containing rigid bipyridyl ligands and two with flexible bipyridyl ligands. We also studied host-guest dynamics and the related optical properties of a copper-acetate-based

PCP constructed using an optically active ligand. We investigated the link between the properties of these selected MOFs and the organic ligands used to construct them. Such a study can provide some insight into the fundamental nature of ligand-derived properties in multi-component systems such as MOFs and PCPs.

1.6. THESIS OUTLINE

The systems reported in this study were analysed using various techniques such as single-crystal X-ray diffraction, powder X-ray diffraction, thermal analysis, gas sorption, solid-state UV-vis spectroscopy, optical microscopy, and computational methods. The methodologies, experimental conditions and instrumentation used during the course of this work are described in **Chapter 2** of this dissertation.

Chapter 3 describes a systematic study of three closely related microporous 3D copper(II)-glutarate-based MOFs whose pore dimensions vary according to the choice of rigid 4,4´-bipyridyl linker. The tuneable linker allows exploration of the effect of increasing pore dimensions on the sorption behaviour of the frameworks. The MOFs described here capture CO_2 under supercritical conditions and continue to sequester the gas under ambient conditions. The trend in the gas sorption isotherms for CO_2 is compared with the thermal stability of the CO_2 adducts formed by the three MOFs. Computational models constructed using crystallographic data were used to calculate framework electrostatic potential maps in order to elucidate the nature of the framework—CO_2 interactions.

In **Chapter 4** the isoreticular series of rigid MOFs in **Chapter 3** is extended to two MOFs containing flexible, rather than rigid, 4,4´-bipyridyl linkers. These two materials undergo spontaneous phase changes upon solvent loss at room temperature. The crystal structures of these phases, along with the CO_2 adducts, were analysed for insight into the phase change behaviour. Gas sorption studies were conducted using various gases to determine if the phase change can be induced using gas pressure at room temperature. Potential energy surface scans employing density functional theory and molecular mechanics were used to elucidate the phase change behaviour of these flexible 3D MOFs.

Chapter 5 describes the solvent exchange process and related structural change in a 1D PCP comprising 1D channels occupied by solvent guest molecules. This coordination polymer uses the same copper carboxylate paddle-wheel SBU as the MOFs described in **Chapters 3** and **4**. The bipyridyl tetrazine-based ligand used to construct this PCP afforded crystals with solvatochromic properties. These properties were exploited in order to observe the solvent exchange process involving two polar organic solvents using polarised light optical microscopy. This yielded unusual solvent exchange behaviour, which we rationalised using a computational approach.

Finally, **Chapter 6** summarises this work and presents some concluding remarks.

REFERENCES

[1] P. B. Venuto, *Microporous Mater.* **1994**, *2*, 297-411.
[2] J. V. Smith, *Chem. Rev.* **1988**, *88*, 149-182.
[3] K. A. Hofmann, F. Küspert, *Z. Anorg. Chem.* **1897**, *15*, 204-207.
[4] H. Powell, J. Rayner, *Nature* **1949**, *163*, 566-567.
[5] B. F. Hoskins, R. Robson, *J. Am. Chem. Soc.* **1990**, *112*, 1546-1554.
[6] H. Furukawa, K. E. Cordova, M. O'Keeffe, O. M. Yaghi, *Science* **2013**, *341*.
[7] M. Fujita, Y. J. Kwon, S. Washizu, K. Ogura, *J. Am. Chem. Soc.* **1994**, *116*, 1151-1152.
[8] O. M. Yaghi, G. Li, H. Li, *Nature* **1995**, *378*, 703-706.
[9] D. Venkataraman, G. B. Gardner, S. Lee, J. S. Moore, *J. Am. Chem. Soc.* **1995**, *117*, 11600-11601.
[10] M. Kondo, T. Yoshitomi, H. Matsuzaka, S. Kitagawa, K. Seki, *Angew. Chem. Int. Ed. Engl.* **1997**, *36*, 1725-1727.
[11] S. Kitagawa, R. Kitaura, S.-i. Noro, *Angew. Chem. Int. Ed.* **2004**, *43*, 2334-2375.
[12] S. R. Batten, N. R. Champness, X.-M. Chen, J. Garcia-Martinez, S. Kitagawa, L. Ohrstrom, M. O'Keeffe, M. P. Suh, J. Reedijk, *CrystEngComm* **2012**, *14*, 3001-3004.
[13] D. V. Soldatov, I. L. Moudrakovski, C. I. Ratcliffe, R. Dutrisac, J. A. Ripmeester, *Chem. Mater.* **2003**, *15*, 4810-4818.
[14] A. J. Blake, S. J. Hill, P. Hubberstey, W.-S. Li, *J. Chem. Soc., Dalton Trans.* **1997**, 913-914.
[15] C.-H. Chen, J. Cai, C.-Z. Liao, X.-L. Feng, X.-M. Chen, S. W. Ng, *Inorg. Chem.* **2002**, *41*, 4967-4974.
[16] J. Huang, X. Wang, J. Zhang, *J. Inorg. Organomet. Polym. Mater.* **2012**, *22*, 686-691.
[17] T. Satoshi, H. Taku, N. Ei-ichi, M. Katsura, M. Wasuke, *Chem. Lett.* **2002**, *31*, 1208-1209.
[18] S. Takamizawa, E.-i. Nakata, H. Yokoyama, K. Mochizuki, W. Mori, *Angew. Chem. Int. Ed.* **2003**, *42*, 4331-4334.
[19] H. Li, M. Eddaoudi, M. O'Keeffe, O. M. Yaghi, *Nature* **1999**, *402*, 276-279.
[20] S. L. James, *Chem. Soc. Rev.* **2003**, *32*, 276-288.
[21] T. R. Cook, Y. Zheng, P. J. Stang, *Chem. Rev.* **2013**, *113*, 734-777.
[22] S. T. Meek, J. A. Greathouse, M. D. Allendorf, *Adv. Mater.* **2011**, *23*, 249-267.
[23] S. Qiu, G. Zhu, *Coord. Chem. Rev.* **2009**, *253*, 2891-2911.
[24] N. Stock, S. Biswas, *Chem. Rev.* **2012**, *112*, 933-969.
[25] M. Eddaoudi, H. Li, O. M. Yaghi, *J. Am. Chem. Soc.* **2000**, *122*, 1391-1397.
[26] A. Rabenau, *Angew. Chem. Int. Ed. Engl.* **1985**, *24*, 1026-1040.
[27] M. Eddaoudi, D. B. Moler, H. Li, B. Chen, T. M. Reineke, M. O'Keeffe, O. M. Yaghi, *Acc. Chem. Res.* **2001**, *34*, 319-330.
[28] M. Eddaoudi, J. Kim, N. Rosi, D. Vodak, J. Wachter, M. O'Keeffe, O. M. Yaghi, *Science* **2002**, *295*, 469-472.
[29] H. Deng, C. J. Doonan, H. Furukawa, R. B. Ferreira, J. Towne, C. B. Knobler, B. Wang, O. M. Yaghi, *Science* **2010**, *327*, 846-850.
[30] M. Li, D. Li, M. O'Keeffe, O. M. Yaghi, *Chem. Rev.* **2014**, *114*, 1343-1370.
[31] D. J. Tranchemontagne, J. L. Mendoza-Cortes, M. O'Keeffe, O. M. Yaghi, *Chem. Soc. Rev.* **2009**, *38*, 1257-1283.
[32] W. Lu, Z. Wei, Z.-Y. Gu, T.-F. Liu, J. Park, J. Park, J. Tian, M. Zhang, Q. Zhang, T. Gentle Iii, M. Bosch, H.-C. Zhou, *Chem. Soc. Rev.* **2014**, *43*, 5561-5593.

[33] O. M. Yaghi, M. O'Keeffe, N. W. Ockwig, H. K. Chae, M. Eddaoudi, J. Kim, *Nature* **2003**, *423*, 705-714.
[34] R. Banerjee, H. Furukawa, D. Britt, C. Knobler, M. O'Keeffe, O. M. Yaghi, *J. Am. Chem. Soc.* **2009**, *131*, 3875-3877.
[35] H. Furukawa, Y. B. Go, N. Ko, Y. K. Park, F. J. Uribe-Romo, J. Kim, M. O'Keeffe, O. M. Yaghi, *Inorg. Chem.* **2011**, *50*, 9147-9152.
[36] L. Ma, J. M. Falkowski, C. Abney, W. Lin, *Nat. Chem.* **2010**, *2*, 838-846.
[37] J. Liu, B. Lukose, O. Shekhah, H. K. Arslan, P. Weidler, H. Gliemann, S. Bräse, S. Grosjean, A. Godt, X. Feng, K. Müllen, I.-B. Magdau, T. Heine, C. Wöll, *Sci. Rep.* **2012**, *2*, 921.
[38] L. J. Barbour, *Chem. Commun.* **2006**, 1163-1168.
[39] K. S. W. Sing, *Adv. Colloid Interface Sci.* **1998**, *76–77*, 3-11.
[40] S. Brunauer, L. S. Deming, W. E. Deming, E. Teller, *J. Am. Chem. Soc.* **1940**, *62*, 1723-1732.
[41] K. S. W. Sing, in *Pure Appl. Chem., Vol. 57*, **1985**, p. 603.
[42] A. J. Fletcher, K. M. Thomas, M. J. Rosseinsky, *J. Solid State Chem.* **2005**, *178*, 2491-2510.
[43] K. S. Walton, A. R. Millward, D. Dubbeldam, H. Frost, J. J. Low, O. M. Yaghi, R. Q. Snurr, *J. Am. Chem. Soc.* **2008**, *130*, 406-407.
[44] M. D. Donohue, G. L. Aranovich, *J. Colloid Interface Sci.* **1998**, *205*, 121-130.
[45] J. T. Culp, M. R. Smith, E. Bittner, B. Bockrath, *J. Am. Chem. Soc.* **2008**, *130*, 12427-12434.
[46] P. Lama, H. Aggarwal, C. X. Bezuidenhout, L. J. Barbour, *Angew. Chem. Int. Ed.* **2016**, *55*, 13271-13275.
[47] J. Seo, C. Bonneau, R. Matsuda, M. Takata, S. Kitagawa, *J. Am. Chem. Soc.* **2011**, *133*, 9005-9013.
[48] K. Uemura, R. Matsuda, S. Kitagawa, *J. Solid State Chem.* **2005**, *178*, 2420-2429.
[49] K. Uemura, S. Kitagawa, M. Kondo, K. Fukui, R. Kitaura, H.-C. Chang, T. Mizutani, *Chem. Eur. J.* **2002**, *8*, 3586-3600.
[50] S. Horike, S. Shimomura, S. Kitagawa, *Nat. Chem.* **2009**, *1*, 695-704.
[51] S. Kitagawa, R. Matsuda, *Coord. Chem. Rev.* **2007**, *251*, 2490-2509.
[52] A. Schneemann, V. Bon, I. Schwedler, I. Senkovska, S. Kaskel, R. A. Fischer, *Chem. Soc. Rev.* **2014**, *43*, 6062-6096.
[53] T. Loiseau, C. Serre, C. Huguenard, G. Fink, F. Taulelle, M. Henry, T. Bataille, G. Férey, *Chem. Eur. J.* **2004**, *10*, 1373-1382.
[54] A. Boutin, F.-X. Coudert, M.-A. Springuel-Huet, A. V. Neimark, G. Férey, A. H. Fuchs, *J. Phys. Chem. C* **2010**, *114*, 22237-22244.
[55] A. Modrow, D. Zargarani, R. Herges, N. Stock, *Dalton Trans.* **2011**, *40*, 4217-4222.
[56] I. Grobler, V. J. Smith, P. M. Bhatt, S. A. Herbert, L. J. Barbour, *J. Am. Chem. Soc.* **2013**, *135*, 6411-6414.
[57] E. M. Kosower, *J. Am. Chem. Soc.* **1958**, *80*, 3253-3260.
[58] Y. Cui, Y. Yue, G. Qian, B. Chen, *Chem. Rev.* **2011**, *112*, 1126-1162.
[59] H. Golchoubian, F. Khoshsiar, *IJEE* **2012**.
[60] S. Takamizawa, *Angew. Chem. Int. Ed.* **2015**, *54*, 7033-7036.
[61] M. Kondo, H. Takahashi, H. Watanabe, Y. Shimizu, K. Yamanishi, M. Miyazawa, N. Nishina, Y. Ishida, H. Kawaguchi, F. Uchida, *Int. J. Mol. Sci.* **2010**, *11*, 2821-2838.
[62] K. Uemura, S. Kitagawa, K. Fukui, K. Saito, *J. Am. Chem. Soc.* **2004**, *126*, 3817-3828.
[63] Y. Takasaki, S. Takamizawa, *Chem. Commun.* **2015**, *51*, 5024-5027.
[64] Y. Cui, Y. Yue, G. Qian, B. Chen, *Chem. Rev.* **2012**, *112*, 1126-1162.

[65] Z.-Z. Lu, R. Zhang, Y.-Z. Li, Z.-J. Guo, H.-G. Zheng, *J. Am. Chem. Soc.* **2011**, *133*, 4172-4174.

[66] R. E. Stoiber, S. A. Morse, *Crystal Identification with the Polarizing Microscope*, Springer US, Boston, USA, **2012**,

[67] Nikon - MicroscopyU, Birefringence in Calcite Crystals, https://www.microscopyu.com/tutorials/birefringence-in-calcite-crystals

[68] P. Simoncic, T. Armbruster, P. Pattison, *J. Phys. Chem. B* **2004**, *108*, 17352-17360.

[69] Q. Yang, D. Liu, C. Zhong, J.-R. Li, *Chem. Rev.* **2013**, *113*, 8261-8323.

[70] M. Fischer, J. R. B. Gomes, M. Jorge, *Mol. Simul.* **2014**, *40*, 537-556.

[71] Q. Yang, C. Zhong, *ChemPhysChem* **2006**, *7*, 1417-1421.

[72] M. Tong, Q. Yang, Y. Xiao, C. Zhong, *PCCP* **2014**, *16*, 15189-15198.

[73] R. Krishna, J. M. van Baten, *J. Phys. Chem. C* **2012**, *116*, 23556-23568.

[74] L. Chen, C. A. Morrison, T. Düren, *J. Phys. Chem. C* **2012**, *116*, 18899-18909.

[75] A. L. Dzubak, L.-C. Lin, J. Kim, J. A. Swisher, R. Poloni, S. N. Maximoff, B. Smit, L. Gagliardi, *Nat. Chem.* **2012**, *4*, 810-816.

[76] Q. Yang, Q. Xu, B. Liu, C. Zhong, S. Berend, *Chin. J. Chem. Eng.* **2009**, *17*, 781-790.

[77] W. Morris, N. He, K. G. Ray, P. Klonowski, H. Furukawa, I. N. Daniels, Y. A. Houndonougbo, M. Asta, O. M. Yaghi, B. B. Laird, *J. Phys. Chem. C* **2012**, *116*, 24084-24090.

[78] F. Gandara, T. D. Bennett, *IUCrJ* **2014**, *1*, 563-570.

[79] M. Mazaj, V. Kaucic, N. Zabukovec Logar, *Acta Chim Slov* **2016**, *63*, 440-458.

[80] F. Jensen, *Introduction to Computational Chemistry*, Wiley, **2007**,

[81] M. C. Payne, M. P. Teter, D. C. Allan, T. A. Arias, J. D. Joannopoulos, *Rev. Mod. Phys.* **1992**, *64*, 1045-1097.

[82] G. Kresse, J. Furthmüller, *Phys. Rev. B* **1996**, *54*, 11169-11186.

[83] S. Goedecker, M. Boulet, T. Deutsch, *Comput. Phys. Commun.* **2003**, *154*, 105-110.

[84] P. D. Haynes, M. Côté, *Comput. Phys. Commun.* **2000**, *130*, 130-136.

[85] G. Kresse, D. Joubert, *Phys. Rev. B* **1999**, *59*, 1758-1775.

[86] N. Troullier, J. L. Martins, *Phys. Rev. B* **1991**, *43*, 1993-2006.

[87] Accelrys Software Inc., San Diego, Materials Studio Modeling Environment v8.0.0, **2015**

[88] S. Grimme, *J. Comput. Chem.* **2006**, *27*, 1787-1799.

[89] P. Jurečka, J. Černý, P. Hobza, D. R. Salahub, *J. Comput. Chem.* **2007**, *28*, 555-569.

[90] F. Ortmann, F. Bechstedt, W. G. Schmidt, *Phys. Rev. B* **2006**, *73*, 205101.

[91] S. Saha, U. Becker, *RSC Adv.* **2015**, *5*, 26735-26748.

[92] S. Yang, A. J. Ramirez-Cuesta, R. Newby, V. Garcia-Sakai, P. Manuel, S. K. Callear, S. I. Campbell, C. C. Tang, M. Schröder, *Nat. Chem.* **2015**, *7*, 121-129.

[93] M. E. Casco, Y. Q. Cheng, L. L. Daemen, D. Fairen-Jimenez, E. V. Ramos-Fernandez, A. J. Ramirez-Cuesta, J. Silvestre-Albero, *Chem. Commun.* **2016**, *52*, 3639-3642.

[94] K. Liu, S. Zhang, X. Hu, K. Zhang, A. Roy, G. Yu, *Environ. Sci. Technol.* **2015**, *49*, 8657-8665.

[95] M. Fischer, R. G. Bell, *J. Phys. Chem. C* **2013**, *117*, 24446-24454.

[96] J. Cepeda, S. Pérez-Yáñez, G. Beobide, O. Castillo, M. Fischer, A. Luque, P. A. Wright, *Chem. Eur. J.* **2014**, *20*, 1554-1568.

[97] L. Banting, T. Clark, R. J. Deeth, A. Vityuk, T. Tuttle, D. Richie, T. Engel, P. Popelier, J. W. Essex, *Drug Design Strategies: Computational Techniques and Applications*, Royal Society of Chemistry, **2012**, 89-100.

[98] P. Politzer, J. S. Murray, *Theor. Chem. Acc.* **2002**, *108*, 134-142.

[99] J. S. Murray, P. Politzer, *Wiley Interdiscip. Rev. Comput. Mol. Sci.* **2011**, *1*, 153-163.
[100] R. F. W. Bader, M. T. Carroll, J. R. Cheeseman, C. Chang, *J. Am. Chem. Soc.* **1987**, *109*, 7968-7979.
[101] R. F. W. Bader, W. H. Henneker, P. E. Cade, *J. Chem. Phys.* **1967**, *46*, 3341-3363.
[102] J. S. Murray, P. Politzer, *Croat. Chem. Acta.* **2009**, *82*, 267-275.
[103] T. Clark, A. Alex, B. Beck, F. Burckhardt, J. Chandrasekhar, P. Gedeck, A. Horn, M. Hutter, B. Martin, G. Rauhut, W. Sauer, T. Schindler, T. Steinke, Accelrys Materials Studio, San Diego, CA , USA: Erlangen, Germany, VAMP 10, **2014**
[104] V. Strauss, J. T. Margraf, K. Dirian, Z. Syrgiannis, M. Prato, C. Wessendorf, A. Hirsch, T. Clark, D. M. Guldi, *Angew. Chem. Int. Ed.* **2015**, *54*, 8292-8297.
[105] H. Kayi, T. Clark, *J. Mol. Model.* **2010**, *16*, 29-47.
[106] H. Kayi, T. Clark, *J. Mol. Model.* **2011**, *17*, 2585-2600.
[107] H. Kayi, T. Clark, *J. Mol. Model.* **2007**, *13*, 965-979.
[108] L. Banting, T. Clark, R. S. o. Chemistry, R. J. Deeth, A. Voityuk, T. Tuttle, D. Richie, T. Engel, P. Popelier, J. W. Essex, *Drug Design Strategies: Computational Techniques and Applications*, Royal Society of Chemistry, **2012**, 88-89.
[109] I. Erucar, T. A. Manz, S. Keskin, *Mol. Simul.* **2014**, *40*, 557-570.
[110] M. A. González, *JDN* **2011**, *12*, 169-200.
[111] J. Jiang, *Mol. Simul.* **2014**, *40*, 516-536.
[112] J. G. Harris, K. H. Yung, *J. Phys. Chem.* **1995**, *99*, 12021-12024.
[113] M. G. Martin, J. I. Siepmann, *J. Phys. Chem. B* **1999**, *103*, 4508-4517.
[114] J. J. Potoff, J. I. Siepmann, *AlChE J.* **2001**, *47*, 1676-1682.
[115] T. J. H. Vlugt, R. Krishna, B. Smit, *J. Phys. Chem. B* **1999**, *103*, 1102-1118.
[116] L.-C. Lin, K. Lee, L. Gagliardi, J. B. Neaton, B. Smit, *J. Chem. Theory Comput.* **2014**, *10*, 1477-1488.
[117] H. Sun, *J. Phys. Chem. B* **1998**, *102*, 7338-7364.
[118] R. S. Mulliken, *J. Chem. Phys.* **1955**, *23*, 1833-1840.
[119] M. D. Segall, R. Shah, C. J. Pickard, M. C. Payne, *Phys. Rev. B* **1996**, *54*, 16317-16320.
[120] M. D. Segall, C. J. Pickard, R. Shah, M. C. Payne, *Mol. Phys.* **1996**, *89*, 571-577.
[121] C. Zheng, D. Liu, Q. Yang, C. Zhong, J. Mi, *Ind. Eng. Chem. Res.* **2009**, *48*, 10479-10484.
[122] J. J. Low, A. I. Benin, P. Jakubczak, J. F. Abrahamian, S. A. Faheem, R. R. Willis, *J. Am. Chem. Soc.* **2009**, *131*, 15834-15842.
[123] A. K. Rappé, W. A. Goddard, *J. Phys. Chem.* **1991**, *95*, 3358-3363.
[124] C. E. Wilmer, R. Q. Snurr, *Chem. Eng. J.* **2011**, *171*, 775-781.
[125] E. S. Kadantsev, P. G. Boyd, T. D. Daff, T. K. Woo, *J. Phys. Chem. Lett.* **2013**, *4*, 3056-3061.
[126] S. Ramachandran, T. G. Lenz, W. M. Skiff, A. K. Rappé, *J. Phys. Chem.* **1996**, *100*, 5898-5907.
[127] Nangia A., *CrystEngComm.* **2002**, 1-9.

CHAPTER 2

EXPERIMENTAL METHODS

2.1. MATERIALS

All materials were purchased from Sigma Aldrich and used without further processing or purification except for the N,N´-bis-pyridine-4-ylmethylene-hydrazine (bpymh) and 3,6-di(pyridin-4-yl)-1,2,4,5-tetrazine (dptz) ligands, which were synthesised according to literature procedures.[1-2]

2.2. SYNTHESIS OF MOFS

2.2.1. Chapter 3

$[Cu_2(glu)_2(bpy)]_n \cdot 2.9H_2O$: $Cu(NO_3)_2$ (1 mmol), glutaric acid (H_2glu, 1 mmol) and 4,4´-bipyridine (bpy, 0.5 mmol) and 100 ml H_2O were mixed in a 100 ml reagent glass bottle and placed in a pre-heated oven at 100 °C. Green block-shaped crystals forms at 100 °C after 24 – 48 hours.

$[Cu_2(glu)_2(bpe)]_n \cdot 3H_2O$: $Cu(NO_3)_2$ (1 mmol), glutaric acid (H_2glu, 1 mmol) and *trans*-bis(4-pyridyl)ethylene (bpe, 0.5 mmol) and 100 ml H_2O were mixed in a 100 ml reagent bottle and placed in a pre-heated oven at 100 °C. Green block-shaped crystals forms at 100 °C after 24 – 48 hours.

$[Cu_2(glu)_2(bpymh)]_n \cdot 7.5H_2O$: $Cu(NO_3)_2$ (1 mmol), glutaric acid (H_2glu, 1 mmol) and *N,N´-bis*-pyridine-4-ylmethylene-hydrazine (bpymh, 0.5 mmol) and 100 ml H_2O were mixed in a 100 ml reagent glass bottle and placed in a pre-heated oven at 100 °C. Green block-shaped crystals forms at 100 °C after 24 – 48 hours.

2.2.2. Chapter 4

$[Cu_2(glu)_2(bpa)]_n \cdot 2.4H_2O$: $Cu(NO_3)_2$ (1 mmol), glutaric acid (1 mmol) and 1,2-bis(4-pyridyl)ethane (bpa, 0.5 mmol) and 100 ml H_2O were mixed in a 100 ml glass bottle with a plastic screw cap. One molar eqv. of NaOH was added dropwise with swirling to prevent precipitation. The blue solution was placed in an oven pre-heated to 80 °C. Green block-shaped crystals were obtained after 24 – 48 hours.

$[Cu_2(glu)_2(bpp)]_n \cdot 2acetone$: 50 ml of a H_2O/acetone (1:1) buffer solution was layered on a solution of glutaric acid (1 mmol), 1 eqv NaOH (1M) and 1,3-bis(4-pyridyl)propane (bpp, 0.5 mmol) in 50 ml H_2O/acetone (2:1). A solution of $Cu(NO_3)_2$ (1 mmol) in 50 ml acetone (ace) was

then layered on the buffer solution. Slow solvent diffusion was allowed to occur in an oven heated to 50-55° C. Green block and plate-like crystals forms at 50-55° C and were isolated after 48 hours.

2.2.3. Chapter 5

$[Cu_2(acetate)_2(dptz)]_n \cdot 2CHCl_3$: 50 ml methanol:chloroform buffer (1:1) was layered on a chloroform solution of 3,6-di(pyridin-4-yl)-1,2,4,5-tetrazine (dptz). A methanolic solution of $Cu(acetate)_2$ (0.5 mmol in 50 ml) was then layered on top of the buffer solution. The layered mixture was kept in a 200 ml reagent bottle at 50 °C to afford dark-purple block-shaped crystals.

2.3. SINGLE-CRYSTAL X-RAY DIFFRACTION (SCD)

Suitable single-crystals were selected and loaded onto a diffractometer using a MiTeGen MicroCrystal mount. Single-crystal X-ray diffraction data were collected using a Bruker SMART or an APEX-II DUO diffractometer. Both diffractometers are equipped with APEX-II CCD area-detectors and Oxford Cryosystems 700Plus cryostats. For the SMART X-rays were generated from a sealed tube (MoKα radiation λ = 0.71073 Å) fitted with a multilayer monochromator, while the APEX-II DUO uses an Incoatec IμS microfocus source fitted with a multilayer monochromator. All data were collected at 100 K.

Data reduction was carried out by means of a standard procedure using the Bruker software package SAINT[3] and absorption corrections and the correction of other systematic errors were performed using SADABS[4]. Using Xseed[5-6] and Olex2[7], each structure was solved with the ShelXS[7] structure solution program using Direct Methods and refined with the ShelXL[8] refinement package using least squares minimisation. Hydrogen atoms were placed in calculated positions using riding models. PLATON SQUEEZE[9] was used to determine the total electron count per unit cell (e^-/unit cell) of guest molecules within the MOFs. These values were used to determine the total occupancy of the guest molecules within the MOFs.

2.4. POWDER X-RAY DIFFRACTION (PXRD)

A benchtop Bruker D2 PHASER equipped with a Lynxeye 1D detector and Ni-filtered Cu Kα radiation (λ = 1.5418 Å, generator power is set at 30 kV and 10 mA, and the X-ray beam is restricted by a 1.0 mm divergence slit and a 2.5 mm Soller collimator) was used for routine powder X-ray diffraction (PXRD) data collections. Samples were ground into a powder (with a mortar and pestle) if needed and then loaded onto zero-background sample holders. Samples that lose solvent spontaneously at RT were wrapped with clingfilm to prevent solvent loss during the experiment. A PXRD trace was first measured for the clingfilm on its own in order to ensure that it does not interfere with the PXRD trace of the material of interest.

2.5. THERMOGRAVIMETRIC ANALYSIS (TGA)

Thermogravimetric analysis was conducted using a TA Instruments Q500 analyser. Samples were weighed into a standard TA Instruments aluminium pan and heated from room

temperature at 10 °C/min under a N_2 flow of 50 mL/min up to 600°C. A typical sample size of 1–10 mg was used. Data were exported using the Universal Analysis 2000 v 4.5A (TA Instruments) software while the analyses and figures were prepared using OriginPro.[10]

2.6. DIFFERENTIAL SCANNING CALORIMETRY (DSC)

DSC provides information regarding the physical and chemical changes of a material as a function of temperature. Thermal events are observed as either endothermic or exothermic peaks. A TA Instruments Q100 with Liquid Nitrogen Cooling Accessory (LNCS) was used for differential scanning calorimetry. DSC measures the heat flow into or out of the sample, relative to a reference (empty pan identical to the sample pan), as a function of time and temperature in a controlled atmosphere (Typically N_2 with a flow rate of 50 ml/min). A sample of 1–10 mg was placed in a standard TA Instruments aluminium pan and either analysed as an open pan or covered with an aluminium lid, crimped and pricked to form a pin hole in the lid. The reference pan is subjected to the same protocol as the sample pan. The sample was then heated and cooled at a rate of 10 °C/min. Data were exported using the Universal Analysis 2000 v 4.5A (TA Instruments) software while the analyses and figures were prepared using OriginPro.[10]

2.7. SUPERCRITICAL CO_2 EXPERIMENTS

Newly synthesised MOF crystals were exposed to supercritical CO_2 ($scCO_2$) for 24 h to obtain the apohost or activated phase. Supercritical CO_2, having properties of both liquid and gas, exerts little or no surface tension on the walls of the channels in the crystal. Depending on the solvent present in the channels and the exact conditions of temperature and pressure ($31.1 < T_c < 44$ °C; $73 < P_c < 110$ bar – beyond the critical temperature and pressure) $scCO_2$ is able to dissolve the solvent molecules and leave behind the activated phase. Typically, after the experiment the vial containing the crystals is placed directly onto dry-ice in a Dewar flask for transport to the analytical instruments.

2.8. VOLUMETRIC SORPTION MEASUREMENTS

A Setaram PCTPro-E&E gas sorption analyser with MicroDoser attachment was utilised to conduct high pressure gas sorption experiments with test gases such as N_2, CH_4, C_2H_6, C_3H_8 and CO_2. The instrument is a volumetric gas analyser which utilises Sievert's volumetric method. The sample temperature was maintained to an accuracy of ± 0.05 °C using a Grant refrigerated recirculation bath filled with antifreeze and water. A sample at known pressure and volume was connected to a reservoir of known volume and pressure through an isolation valve. The valve was opened and the system allowed to equilibrate. The difference between the measured pressure and calculated pressure was used to determine the amount of gas adsorbed. NIST software was used to calculate the thermodynamic corrections in order to account for the non-ideal behaviour of the gases at relatively high pressures. The PCTPro-E&E with the MicroDoser attachment is used for small sample sizes and has a range of vacuum to 60 bar. Sample sizes of 100-250 mg were used and activated in-situ using vacuum and heat, if necessary. Blank runs for each gas were recorded to further correct for any other residual

systematic errors in the experiment. Figure preparation and data analyses were performed using Microsoft Excel and OriginPro.[10]

2.9. FOURIER TRANSFORM INFRARED SPECTROSCOPY (FTIR)

A Thermo Nicolet iS10 spectrometer with ATR attachment was used to measure IR spectra. A background scan was collected immediately before each sample scan.

2.10. SOLID-STATE UV-VISIBLE SPECTROSCOPY

Solid-state UV-visible absorption spectra were measured using a SPECORD 210 PLUS spectrophotometer with an integrating sphere supplied by Analytik Jena. The data were analysed and exported using the native software package WinAspect PLUS 3.9.14. and then plotted using Origin Pro.

2.11. TIME-LAPSED POLARISED-LIGHT OPTICAL MICROSCOPY

Single crystals of the relevant compounds were immersed in acetonitrile and nitromethane and sealed within a chamber with windows at the top and bottom. Adjustment (lighting, crystal position, polariser, etc.) were made rapidly and photographs were taken using an appropriate time interval (10 s – 5 min).

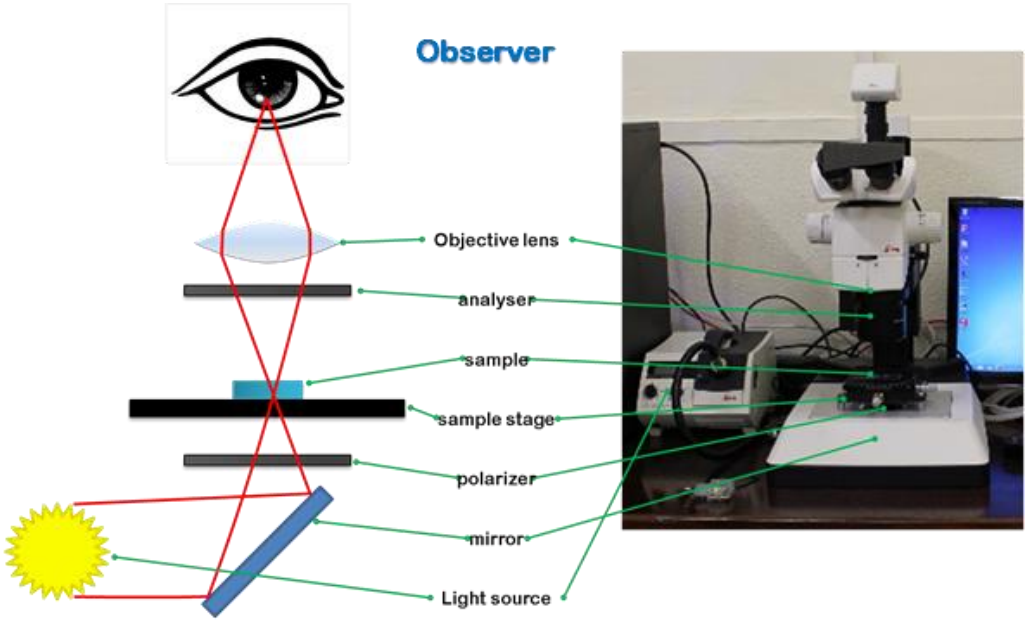

Figure 15. The Leica optical microscope setup used to conduct solvent-exchange experiments.

2.12. CAMBRIDGE STRUCTURAL DATABASE (CSD)[11]

The CSD (version 5.37 + February 2016 data base update) is a structural database that contains published single-crystal and powder diffraction data. The user can conduct searches with specific constraints to obtain a refined set of structural data consistent with the imposed constraints. This makes it possible to study systems with similar traits, synthons and so on to

further understand the nature of intermolecular interactions, molecular conformations, and their roles in the formation of crystals. In this work a search was carried out for glutarate conformations within the database and the frequency of occurrence of these conformations was evaluated.

2.13. GAUSSIAN09

DFT calculations were carried out using the Gaussian09 software package.[12] This was used to compute a *gauche* torsional scan of a single glutaric acid molecule. All optimisations were carried out at the mPW1PW91/6-311+G(d,p) (hybrid Hartree–Fock density functional) level of theory. The SCF=QC option was used to manage conversion difficulties and consequently a larger DFT integration grid (Int=UltraFine) was chosen.

2.14. BIOVIA MATERIALS STUDIO

Materials Studio is a modelling and simulation platform for materials science and chemistry-related fields that enables the user to predict and understand the structure-property relationships of a material.[13]

2.14.1. Materials Visualiser

BIOVIA Materials Studio Visualiser is the core interface of all the materials studio computational modules combined with modelling, analysis, and visualisation tools. The interactive sketching, building and editing tools allow for the construction of molecules as well as periodic models (crystal structures). Results from calculations can be visualised and animated (potentials scans, dynamics trajectories, etc.). Volumetric and surface data (from calculations) of charge density, potentials, and orbitals can be visualised and overlaid. Morphology calculations combined with crystal facets (from SCXRD face indexing) are used to display crystal habits, which can be overlaid with the crystal structures from which they were generated. The Visualiser module also provides a scripting tool which allows for receptive, iterative and linked tasks (between Materials Studio modules). The "*MaterialsScript*" Application Programming Interface (API) also supports scripts written in Perl and allows for debugging with the Visualiser. The scripting capabilities allow one to perform tasks well beyond the capability of the user interface. In this study scripting was mostly used to perform potential energy scans on both molecular and periodic systems.

2.14.2. CASTEP (Cambridge Serial Total Energy Package)

CASTEP is a contemporary quantum mechanics-based program specifically designed for solid-state materials science. CASTEP utilises the DFT plane-wave pseudopotential method which allows for first-principles quantum mechanics calculations that explore the properties of crystals in materials such as semiconductors, ceramics, metals, minerals, zeolites and metal-organic frameworks (MOFs). CASTEP was used to optimise the hydrogen atoms of all the MOF crystal structures as periodic systems. Optimisations was performed using the GGA PBE functional with Grimme's DFT-D dispersion correction. The thresholds for the geometry optimisation and SCF convergence were chosen as 1×10^{-6} eV. Mulliken charges were

calculated at the end of the optimisation process (this is given as an option in the properties tab of the calculation setup). These atomic charges were used in all the molecular mechanics and molecular dynamics calculations.[14]

2.14.3. DMOL^3

DMol^3 is an all-electron numerical method for solving density functional theory (DFT) to model the electronic structures and energetics of molecules, solids, and surfaces. In this work, DMol^3 was used to perform single-point energy calculations (using CASTEP geometries) in order to extract the electron density grid. In this study the 0.01 $e^-/\text{Å}^3$ outer contour of the molecule or framework's electron density ($\rho(\mathbf{r})$) was used to generate a 3D surface on which to map the electrostatic potential of the molecule or framework.[15-16]

2.14.4. Forcite Plus

Forcite is a collection of molecular mechanics tools for the investigation of a wide range of systems. The potential energy surface, on which the atomic nuclei move, is represented by a classical forcefield. High level quantum mechanical calculations and experiment data were used to parameterise the forcefields. Forcite employs several forcefields, namely COMPASS[17], Dreiding[18], Universal[19] and pcff[20]. Forcite can perform the following tasks: single-point energy calculation, geometry optimisation, molecular dynamics (MD), quench dynamics (QD), anneal dynamics, shear, confined shear, cohesive energy density calculation, mechanical properties calculation, solvation free energy calculation. Forcite can perform calculations on single molecules and periodic systems (crystal structures). In this work geometry optimisations, MD and MaterialsScript API (see 2.14.1) were using in conjunction with one another to perform various complex simulations.

2.14.5. VAMP

VAMP is a semi-empirical molecular orbital package optimised to be highly numerically stable and fast. VAMP also implements the natural atomic orbital/point charge (NAO-PC) model for molecular electrostatic properties. It gives accurate dipole and quadrupole data, and high quality molecular electrostatic potential (MEP) data. In this work VAMP was used to calculate MEPs that were mapped on the outer electron density contour of a molecule or MOF. The electrostatic potentials were calculated as part of single-point energy calculations using the NDDO - AM1* method. An SCF convergence threshold of 5×10^{-7} kcal mol^{-1} was used and the grid size for the imported electrostatic potential was set to 0.1 Å. The electron density data obtained from CASTEP (periodic systems) and DMol^3 (molecular models) calculations were used to construct the 3D 0.01 $e^-/\text{Å}^3$ electron density contours of the molecules or frameworks.

2.14.6. Adsorption Locator

The Adsorption Locator module was used to simulate a substrate loaded with an adsorbate. Adsorption Locator can determine low energy adsorption sites on both periodic and non-periodic substrates to investigate preferential adsorption. Adsorption Locator uses an MD simulated annealing approach to identify possible adsorption configurations by carrying out

Monte Carlo searches of the configurational space of the substrate-adsorbate system as the temperature is slowly decreased stepwise. In this work it was used to study the interactions between two solvents (nitromethane and acetonitrile) and two experimentally identified crystal faces.

REFERENCES

[1] A. R. Kennedy, K. G. Brown, D. Graham, J. B. Kirkhouse, M. Kittner, C. Major, C. J. McHugh, P. Murdoch, W. E. Smith, *New J. Chem.* **2005**, *29*, 826-832.

[2] H. Bakkali, C. Marie, A. Ly, C. Thobie-Gautier, J. Graton, M. Pipelier, S. Sengmany, E. Léonel, J.-Y. Nédélec, M. Evain, D. Dubreuil, *Eur. J. Org. Chem.* **2008**, *2008*, 2156-2166.

[3] Bruker AXS Inc., Madison, WI, SAINT Data Reduction Software Version 6.45, **2003**

[4] Bruker AXS Inc., Madison, WI, SADABS Version 2.05, **2002**

[5] J. L. Atwood, L. J. Barbour, *Cryst. Growth Des.* **2003**, *3*, 3-8.

[6] L. J. Barbour, *J. Supramol. Chem.* **2001**, *1*, 189-191.

[7] O. V. Dolomanov, L. J. Bourhis, R. J. Gildea, J. A. K. Howard, H. Puschmann, *J. Appl. Crystallogr.* **2009**, *42*, 339-341.

[8] G. Sheldrick, *Acta Crystallogr. Sect. C.* **2015**, *71*, 3-8.

[9] A. Spek, *Acta Crystallogr. Sect. D.* **2009**, *65*, 148-155.

[10] Origin (OriginLab, Northampton, MA)

[11] A. Nangia, *CrystEngComm* **2002**, *4*, 93-101.

[12] M. J. Frisch, G. W. Trucks, H. B. Schlegel, G. E. Scuseria, M. A. Robb, J. R. Cheeseman, G. Scalmani, V. Barone, B. Mennucci, G. A. Petersson, H. Nakatsuji, M. Caricato, X. Li, H. P. Hratchian, A. F. Izmaylov, J. Bloino, G. Zheng, J. L. Sonnenberg, M. Hada, M. Ehara, K. Toyota, R. Fukuda, J. Hasegawa, M. Ishida, T. Nakajima, Y. Honda, O. Kitao, H. Nakai, T. Vreven, J. A. Montgomery Jr., J. E. Peralta, F. Ogliaro, M. J. Bearpark, J. Heyd, E. N. Brothers, K. N. Kudin, V. N. Staroverov, R. Kobayashi, J. Normand, K. Raghavachari, A. P. Rendell, J. C. Burant, S. S. Iyengar, J. Tomasi, M. Cossi, N. Rega, N. J. Millam, M. Klene, J. E. Knox, J. B. Cross, V. Bakken, C. Adamo, J. Jaramillo, R. Gomperts, R. E. Stratmann, O. Yazyev, A. J. Austin, R. Cammi, C. Pomelli, J. W. Ochterski, R. L. Martin, K. Morokuma, V. G. Zakrzewski, G. A. Voth, P. Salvador, J. J. Dannenberg, S. Dapprich, A. D. Daniels, Ö. Farkas, J. B. Foresman, J. V. Ortiz, J. Cioslowski, D. J. Fox, Gaussian, Inc., Wallingford, CT, USA, Gaussian 09 **2009**

[13] Accelrys Software Inc., San Diego, Materials Studio Modeling Environment v8.0.0, **2015**

[14] S. J. Clark, M. D. Segall, C. J. Pickard, P. J. Hasnip, M. I. J. Probert, K. Refson, M. C. Payne, in *Z. Kristallogr. Cryst. Mater., Vol. 220*, **2005**, p. 567.

[15] B. Delley, *J. Chem. Phys.* **1990**, *92*, 508-517.

[16] B. Delley, *J. Chem. Phys.* **2000**, *113*, 7756-7764.

[17] H. Sun, *J. Phys. Chem. B* **1998**, *102*, 7338-7364.

[18] S. L. Mayo, B. D. Olafson, W. A. Goddard, *J. Phys. Chem.* **1990**, *94*, 8897-8909.

[19] A. K. Rappé, C. J. Casewit, K. Colwell, W. A. Goddard, W. Skiff, *J. Am. Chem. Soc* **1992**, *114*, 10024-10035.

[20] H. Sun, *J. Comput. Chem.* **1994**, *15*, 752-768.

CHAPTER 3

EXTREME CO_2 SORPTION HYSTERESIS IN OPEN-CHANNEL RIGID METAL-ORGANIC FRAMEWORKS

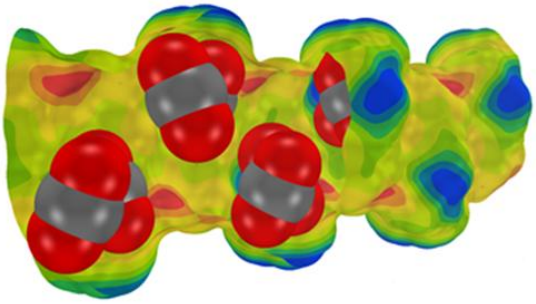

3.1. COMMUNICATION IN ANGEWANDTE CHEMIE INTERNATIONAL EDITION (PUBLISHED)

Contributions of the author:

- Design of project with Dr Vincent J. Smith
- Preparation of MOFs
- Supercritical CO_2 experiments
- Collection of single-crystal X-ray data
- Solution and refinement of single-crystal X-ray structures
- Recording of PXRD patterns
- Recording of TGA and DSC thermograms
- Sorption analysis with Dr. Prashant M. Bhatt
- Computational modelling and electrostatics calculations
- Interpretation of results with Dr Vincent J. Smith
- Writing the first draft of the article

Angewandte Communications

extreme hysteresis

DOI: 10.1002/anie.201((will be filled in by the editorial staff))

Extreme CO_2 Sorption Hysteresis in Open-Channel Rigid Metal-Organic Frameworks**

*Charl X. Bezuidenhout, Vincent J. Smith, Prashant M. Bhatt, Catharine Esterhuysen and Leonard J. Barbour**

***Abstract**: We report a systematic study of three closely related microporous metal-organic frameworks whose pore dimensions vary according to the choice of 4,4´-bipyridyl linker. The tunable linker allows exploration of the effect of increasing pore dimensions on the sorption behaviour of the frameworks. The MOFs described here capture CO_2 under supercritical conditions and continue to sequester the gas under ambient conditions. Gas sorption isotherms for CO_2 are compared with thermogravimetric data and the CO_2 molecules in the channels of the frameworks could be modeled using single-crystal X-ray diffraction analysis. Crystallographic data were used to construct a theoretical model based on DFT methods in order to calculate framework electrostatic potential maps with a view to understanding the nature of the sorbate-sorbent interactions.*

The potential advantages of metal-organic frameworks (MOFs) for CO_2 capture and storage are derived from a number of their inherent properties. These include chemical versatility, robustness, high thermal and chemical stability, large surface areas, and large void volumes. High guest-accessible volumes and surface areas result in low densities, which in turn may yield high CO_2 sorption capacities by weight. This is evidenced by superior active surface areas per unit weight (up to 7100 $m^2 g^{-1}$ for MOFs)[1] when compared to other sorbents such as activated carbon and zeolites (400 to 1500 $m^2 g^{-1}$). However, for some applications (e.g. separation), sorption capacity is less important than selectivity. The latter is influenced by three factors: (i) the molecular sieving effect, which is based on a size/shape exclusion principle, (ii) the thermodynamic effect, which results from preferential packing of gas molecules in the pores of the host, the channel topology and the surface interactions between gas molecules and the channel walls and (iii) the kinetic effect, resulting from different gases having different kinetic diameters and energies, which in turn leads to variation in diffusion rates.[2] Together these factors contribute to the characteristic isotherms associated with sorption; in this regard the IUPAC have classified six typical sorption isotherms (Figure S1, ESI), five of which are based on the work by Brunauer *et al*. (BDDT system).[3] The Type I isotherm is usually associated with microporous frameworks, Types II, III and VI with non-, meso- or macroporous materials and Types IV and V exclusively with mesoporosity. According to Fletcher *et al*.[3c] the shapes of the isotherms are influenced by pore size, host-guest and guest-guest interactions. Moreover, the shapes of the isotherms for rigid frameworks are greatly influenced by electrostatic interactions, which can produce artifacts (e.g. adsorption hysteresis and stepped isotherms) similar to those induced by framework flexibility.[3d,3e]

Adsorption hysteresis occurs when the sorption and desorption isotherms do not overlap and it may result from intrinsic framework flexibility, a phase transition, capillary condensation or gas trapping within the pore apertures.[3a] Sorption isotherms that display hysteresis can be classified into several categories as shown in Scheme 1: extreme (H1 and H4) and intermediate (H2 and H3). In H1 the hysteretic sorption and desorption isotherms are close to vertical and almost parallel to each other while in H4 they are close to horizontal and almost parallel. Types H2 and H3 have shapes that fall between those of H1 and H4.[3f]

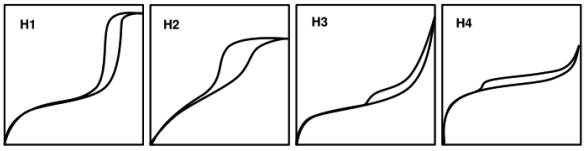

Scheme 1. The four typical hysteretic isotherms.[3f]

The positions of guest molecules in a channel or cavity are determined by steric forces resulting from Pauli repulsion (host-guest fit) and attractive interactions with the walls of the channel or cavity. The latter are primarily due to electrostatic attraction, although dispersion may also play a role. In a largely uniform channel, steric repulsion and attractive dispersion interactions remain relatively constant along the channel length. Hence the electrostatic interactions between the guest and the walls of the channel play a dominant role in determining the guest sorption site.[4] Therefore molecular electrostatic potential (MEP) maps can provide significant insight into the nature of the electrostatic interactions between guest molecules and the host framework.

The MEP ($V(r)$) is a well-established and highly useful tool for the study of molecular properties and noncovalent interactions between molecules. Of the various representations of MEPs, the most common are two-dimensional (2D) and three-dimensional (3D) contour maps.[4a,4b] The application of MEPs is mainly associated with the study of electrostatic (Coulombic) interactions;[5] e.g. in the study of protonation processes,[6] molecular recognition,[7] differentiation between agonists and antagonists,[8] enzyme-ligand interactions,[9] excited electronic

[*] C. X. Bezuidenhout, Dr V. J. Smith, Dr P. M. Bhatt, Prof. C. Esterhuysen and Prof L. J. Barbour
Department of Chemistry and Polymer Science
University of Stellenbosch
Matieland 7602, South Africa
E-mail: ljb@sun.ac.za

[**] LJB and CE thank the National Research Foundation (NRF) of South Africa and Stellenbosch University for financial support as well as the Centre for High Performance Computing (CHPC) in Cape Town for the use of their resources.

CCDC 1016695-1016697. Supporting information for this article is available on the WWW under http://dx.doi.org/10.1002/anie.201xxxxxx.

Angewandte Communications

states,[10] molecular reactivity,[11] and tautomerization.[12]

The hydrothermal reaction of $Cu(NO_3)_2{\cdot}2.5H_2O$, glutaric acid ($gluH_2$) and L_n where L_1 = 4,4´-bipyridine (bpy), L_2 = *trans-bis*(4-pyridyl)ethylene (bpe) and L_3 = *N,N´-bis*-pyridine-4-ylmethylene-hydrazine (bpymh) in H_2O yielded three 3D MOFs: $[Cu_2(glu)_2(bpy){\cdot}2.9H_2O]$ = **1a**, $[Cu_2(glu)_2(bpe){\cdot}3H_2O]$ = **2a** and $[Cu_2(glu)_2(bpymh){\cdot}7.5H_2O]$ = **3a**.[13] Green block-shaped crystals of the as-synthesized frameworks were dehydrated by placing them under dynamic vacuum at 150 °C for 24 h, affording crystals of the apohosts **1**, **2** and **3** (Figure 1). Single-crystal X-ray diffraction analysis (SCD) reveals the homeotypic[14] nature of frameworks **1a**, **2a**, **3a**, **1**, **2**, and **3**. All of the frameworks crystallize in the monoclinic space group *C*2/*c* with their *a* axes, *β* angles, unit cell volumes and channel dimensions responding to changes in the length of the bipyridyl linker. The three rigid microporous frameworks are related to the α-polonium net and contain open 1D corrugated channels with constriction and dilation dimensions of 2.8 × 5.5 Å and 5.6 × 7.6 Å for **1**, 4.7 × 6.5 Å and 7.3 × 10.9 Å for **2**, and 6.2 × 7.2 Å and 9.2 × 10.6 Å for **3**. The framework structures can be described as 2D corrugated layers comprising glutarate anions that are equatorially coordinated to two pentacoordinate Cu cations, thus forming paddlewheel secondary building units (SBUs). Adjacent corrugated layers are joined by the various axially coordinated linkers that form crisscrossed pillars (Figure S2).

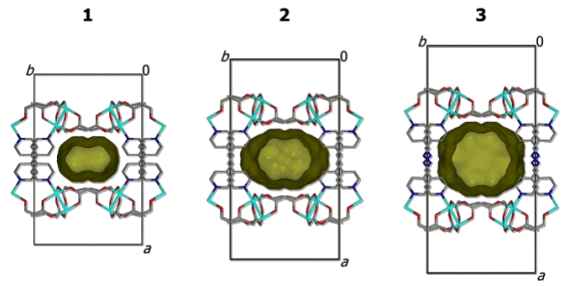

Figure 1. Perspective views along the channels of **1**, **2** and **3** running parallel to [0 0 1]. The guest-accessible surfaces were mapped using a probe of radius 1.4 Å. Hydrogen atoms are omitted for clarity.

We also investigated whether the as-synthesized frameworks could be desolvated under supercritical CO_2 ($scCO_2$) conditions according to a procedure similar to that first reported by Hupp *et al*.[15] After separately exposing **1a**, **2a** and **3a** to $scCO_2$ for 24 h, crystals of suitable quality were selected under ambient conditions and then subjected to SCD analysis at 100 K. The crystal structures reveal that the original H_2O molecules had been replaced by CO_2 molecules, which are then retained in the channels after removal of the crystals from $scCO_2$. The new phases **1b**, **2b** and **3b** are also homeotypic with respect to the as-synthesized and apohost phases.

In all three cases it was possible to model the CO_2 molecules in the dilated regions of the channels using SCD analysis (Figure 2); guest arrangements in the channels of **1b**, **2b** and **3b** resemble two of those observed in dry ice *i.e. slipped-parallel* and *crossed* (Figure S3). However, the *T-shaped* motif is not observed. The intermolecular distances between neighboring CO_2 molecules are much larger than those observed in dry ice, and this is most likely due to corrugation of the channel.

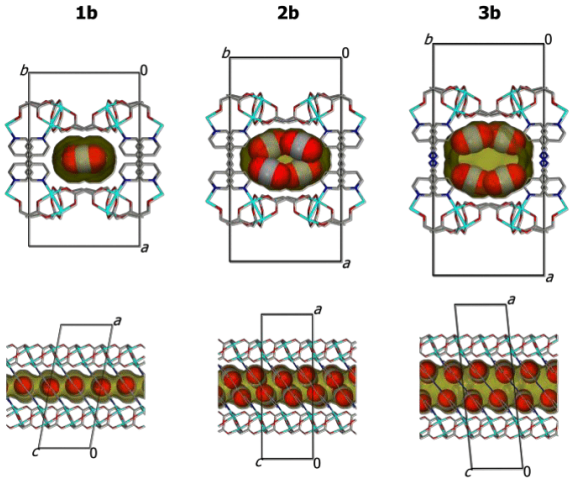

Figure 2. Perspective views along [001] of the crystal structures obtained for **1b**, **2b** and **3b** after $scCO_2$ treatment. The CO_2 molecules are shown in space filling representation and the solvent-accessible surfaces were mapped with a probe of radius of 1.4 Å. Hydrogen atoms are omitted for clarity.

In order to distinguish between the idealized arrangements of CO_2 molecules in dry ice and those observed in frameworks **1b**, **2b** and **3b**, we prefix the term describing the arrangement with '*pseudo*'. The CO_2 molecules in **1b** are *pseudo-crossed* along the channel while those in **2b** are both *pseudo-crossed* along the channel and *pseudo-slipped-parallel* diagonally across the channel (Figure S3). The CO_2 molecules of **3b** only adopt the *pseudo-slipped-parallel* arrangement diagonally across the channel.

Owing to the remarkable stability of **1b**, **2b** and **3b** to guest-loss under ambient conditions it was possible to analyse each sample using thermogravimetric analysis (TGA) (Figure 3), differential scanning calorimetry (DSC) and Fourier transform infrared spectroscopy (FTIR). Comparative FTIR analysis of the as-synthesized, activated and $scCO_2$ exposed materials confirmed the presence of CO_2 in **1b**, **2b** and **3b** (Figure S4). The evolution ranges for the guest CO_2 in the three frameworks are 40 – 260 °C for **1b**, 30 – 90 °C for **2b** and 30 – 80 °C for **3b** (Figure S5, stoichiometric data obtained from TGA and SQUEEZE[16] calculations are tabulated in Table S1). Thermal stability, defined here as the temperature corresponding to the maximum rate of expulsion of CO_2 from the framework, is inversely related to the size of the channel, with **1b** >> **2b** ≈ **3b** (164, 66 and 64 °C, respectively), implying that CO_2 evolution follows a trend of decreasing steric stabilization.

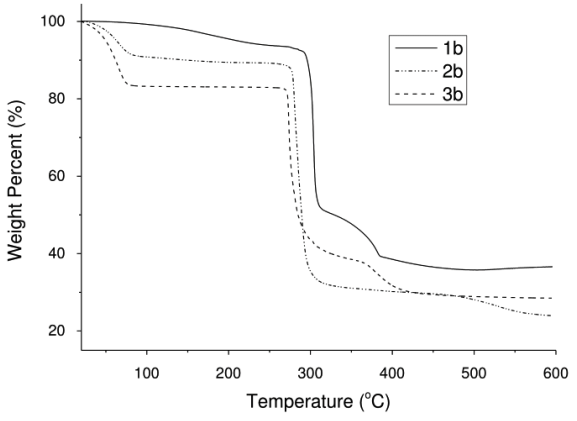

Angewandte Communications

Figure 3. TGA thermograms for **1b**, **2b** and **3b**.

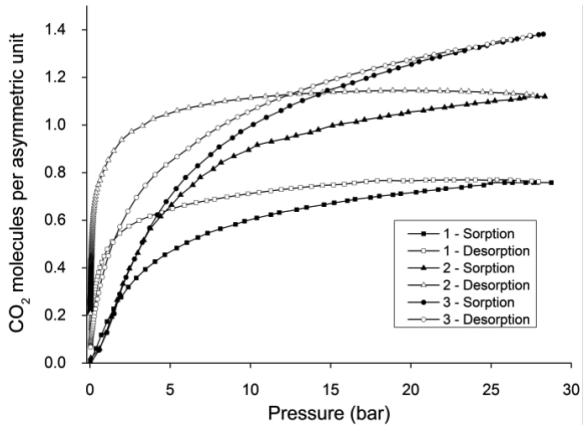

Figure 4. Type-I CO_2 sorption and desorption isotherms, measured at 25 °C, for frameworks **1**, **2** and **3**.

The isotherms shown in Figure 4 are characteristically Type-I, as expected for microporous frameworks.[3b] Furthermore, all three isotherms exhibit hysteresis, with **1** and **2** displaying a combination of H1 and H4 extreme hysteresis, while **3** displays type H3 intermediate hysteresis. For each isotherm we have calculated the extent of hysteresis (as defined in the ESI, and specifically for use in this work), which is expressed as a percentage. The isotherm for **2** exhibits the most extreme hysteresis (21.1%), followed by **1** (13.1%) and **3** (3.3%). It is interesting to note that framework **2**, with intermediate channel dimensions, experiences the most extreme hysteresis while the order of hysteresis experienced by **1** and **3** corresponds inversely to their relative channel dimensions. The results for **2** are also at odds with the thermal stability data determined from TGA and a computational investigation was therefore undertaken in order to explain this apparent anomaly.

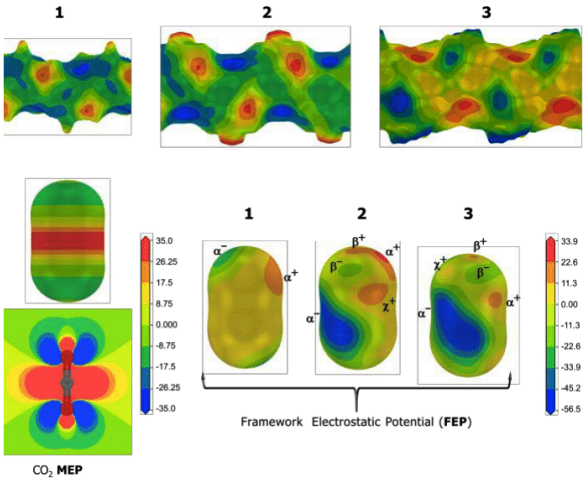

Figure 5. FEP surfaces of **1**, **2** and **3** mapped onto their respective 0.01 $e^- Å^{-3}$ electron density contours. Bottom-left: The molecular electrostatic potential (MEP) of an isolated CO_2 molecule mapped onto the 0.01 $e^- Å^{-3}$ electron density contour (upper) and a 2D slice of the CO_2 electrostatic potential (lower). Bottom-right: FEP surfaces of **1**, **2** and **3** mapped onto the 0.01 $e^- Å^{-3}$ electron density contours of the CO_2 molecule in their crystallographic locations. The gradation on the scale bar is in kcal mol^{-1}, with positive values in red and negative values in blue.

The unusual hysteretic behaviour of **2** cannot be explained by steric interactions (*i.e.* channel topology) alone. We therefore investigated the host-guest electrostatic interactions in order to quantify the stability of CO_2 in frameworks **1**, **2** and **3**. For each framework the electrostatic potential (FEP) was calculated based on a channel three unit cells in length along [001] (Figure S6). Using electron density data obtained from DFT calculations (see ESI for details), three dimensional electron density contours at 0.01 $e^- Å^{-3}$ intervals were calculated for both the CO_2 molecules and the framework channels. The electrostatic potential calculated for each framework was then mapped onto the two electron density contours for each host-guest system (Figure 5). From the channel electron density contours it appears that the three frameworks have similar electrostatic topologies. In order to elucidate how this influences the CO_2 molecules, the FEPs were mapped onto the CO_2 electron density contours in their crystallographically determined positions. For comparison, the molecular electrostatic potential of an isolated CO_2 molecule is shown at the bottom left of Figure 5; negative potentials are present on the oxygen atoms and, consequently, a highly positive potential is centred on the carbon atom. This suggests that a CO_2 carbon atom can form stronger electrostatic interactions as compared to the oxygen atoms.

The significance of the electrostatic potential becomes apparent when we consider the Coulombic interactions between CO_2 molecules and the three frameworks. The FEPs of **1**, **2** and **3** mapped onto the CO_2 molecules provide a detailed representation of their electrostatic interactions with the frameworks. Attractive interactions between the CO_2 molecules and the surrounding framework occur where the MEPs and FEPs display opposite colouring (in the extreme, blue on red). The bottom right-hand side of Figure 5 shows that **1** possesses moderate positive and negative potentials near the oxygen atoms of the CO_2 molecules, as well as a weak positive potential around the carbon atom. Since there is little overall electrostatic stabilization between the CO_2 molecules and the host framework, the CO_2 is mostly stabilized by dispersion interactions (London forces). Frameworks **2** and **3** have strong negative potentials (almost double the magnitude of those of their positive potentials, see Table S2) near the carbon atom of the CO_2 molecule (Figure 5, blue regions). These strong electrostatic interactions therefore determine the positions of the CO_2 molecules within the frameworks of **2** and **3**. Further fine-tuning of the CO_2 position and orientation is achieved through weaker electrostatic interactions between the framework and the oxygen atoms of the CO_2 molecules. The only destabilizing electrostatic interactions in **2** and **3** are due to negative potentials on the oxygen atoms of the CO_2 molecules that are repelled by the negative potentials β^- and χ^- for their respective frameworks (Table S2). Framework **3** has a slightly larger value for the negative potential α^-, thus forming a more stabilizing interaction with the positive potential on the CO_2 as compared to **2**, while β^- and χ^- for **2** are far lower in magnitude than those for **3** (indicating lower electrostatic repulsion and hence less destabilization). Moreover, **2b** shows the largest positive potentials around the oxygen atoms of the CO_2, confirming that framework **2** possesses the most electrostatically stabilized site for CO_2 binding. All of the positive FEP maxima are due to framework hydrogen atoms, while the FEP minima are due to the carboxylate oxygen

Angewandte Communications

atoms (Figure S7). The guest docking sites in **2** and **3** thus appear to be electrostatically complementary to CO_2 molecules. In **1** the CO_2 molecules are bound sterically, whereas those in **2** and **3** are able to adjust their positions in accordance with the electrostatics of the framework, thereby maximizing host-guest interactions.

We have shown that open-channeled MOFs are capable of trapping CO_2 under $scCO_2$ conditions while also being able to sequester CO_2 at room temperature (RT). These MOFs display extreme hysteresis at high pressures and RT and we have shown that framework electrostatic maps (FEPs) provide a powerful means of understanding trends in host-guest binding stability. We have shown that MOFs **1**, **2** and **3** meet two of the three principles of selectivity mentioned earlier: (i) the size/shape exclusion principle and (ii) the thermodynamic effect due to preferential packing, surface interactions and suitable topology. The third principle (i.e. the kinetic effect) is a property of the gas and not of the framework. From our test-case study of three analogous frameworks, we can conclude that the steric and electrostatic topologies of framework **2** provide the most favourable combination of factors for binding CO_2 guest molecules, thus explaining the observed extreme sorption-desorption hysteresis.

Received: ((will be filled in by the editorial staff))
Published online on ((will be filled in by the editorial staff))

Keywords: carbon dioxide sorption • extreme hysteresis • framework electrostatic potential • molecular electrostatic potential • high pressure sorption

[1] D. M. D'Alessandro, B. Smit, J. R. Long, *Angew. Chem.* **2006**, *118*, 1-5; *Angew. Chem. Int. Edit.* **2010**, *49, 6058-6082.*;

[2] a) Y. S. Bae, R. Q. Snurr, *Angew. Chem. Int. Edit.* **2011**, *50,* 11586-11596.; b) K. Sumida, D. L. Rogow, J. A. Mason, T. M. McDonald, E. D. Bloch, Z. R. Herm, T. H. Bae, J. R. Long, *Chem. Rev.* **2012,** *112*, 724-781.; c) Y. Peng, V. Krungleviciute, I. Eryazici, J. T. Hupp, O. K. Farha, T. Yildirim, *J. Am. Chem. Soc.* **2013**, *135*, 11887−11894.

[3] a) Victor Gold, in *Compendium of Chemical Terminology*, 2nd ed. (Eds: A. D. McNaught and A. Wilkinson), Blackwell Scientific Publications, Oxford, **1997**, page 585.; b) S. Brunauer, L. Deming, W. Deming, E. Teller, *J. Am. Chem. Soc.* **1940**, *62*, 1723-1732.; c) A. J. Fletcher, K. M. Thomas, M. J. Rosseinsky, *Solid State Chem*. **2005**, *178*, 2491-2510.; d) J. T. Culp, M. R. Smith, E. Bittner, B. Bockrath, *J. Am. Chem. Soc.* **2008**, *130*, 12427-12434.; e) K. S. Walton, A. R. Millward, D. Dubbeldam, H. Frost, J. J. Low, O. M. Yaghi, R. Q. Snurr, *J. Am. Chem. Soc.* **2008**, *130*, 406-407.; f) M. D. Donohue, G. L. Aranovich, *J. Colloid Interface Sci*. **1998**, *205*, 121–130.

[4] a) Q. Yang, C. Zhong, *ChemPhysChem* **2006**, *7* (7), 1417-1421; b) Q. Yang, D. Liu, C. Zhong, J. Li, *Chem. Rev.* **2013**, *113* (10), 8261-8323; c) Q. Yang, Q. Xu, B. Liu, C. Zhong, S. Berend, *Chin. J. Chem. Eng.* **2009**, *17* (5), 781-790.

[5] a) S. Demir, M. Dinçer, A. Cukurovali, I. Yilmaz, *Int. J. Quantum Chem*. **2012**, *112* (4), 1016-1028; b) J. S. Murray, P. Politzer, *WIREs Comput. Mol. Sci.* **2011**, *1* (2), 153-163; c) G. Náray-Szabó, G. G. Ferenczy, *Chem. Rev*. **1995**, *95* (4), 829-847.

[6] a) R. Bonaccorsi, J. Tomasi, E. Scrocco, A. Pullman, *Chem. Phys. Lett*. **1972**, *12*, 622; b) R. Bonaccorsi, A. Pullman, E. Scrocco, J. Tomasi, *Theor. Chim. Acta* **1972**, *24*, 51-60; b) I. Tuñón, E. Silla, J. Tomasi, *J. Phys. Chem*. **1992**, *96*, 9043-9048; c) J. S. Murray, P. Lane, M. Göbel, T. M. Klapötke, P. Politzer, *J. Chem. Phys.* **2009**, *130*, 104304.

[7] a) E. P. Bishop, R. Rohs, S. C. J. Parker, S. M. West, P. Liu, R. S. Mann, B. Honig, T. D. Tullius, *ACS Chem. Biol.* **2011**, *6*, 1314-1320; b) A. Chang, B. A. Hackett, C. C. Winter, U. J. Buchholz, R. E. Dutch, *J. Virol*. **2012**, *86*, 9843-9853; c) F. S. Dukhovich, M. B. Darkhovskii, *J. Mol. Recognit.* **2003**, *16*, 191-202; d) P. Sjoberg, J. S. Murray, T. Brinck, P. Evans, P. Politzer, *J. Mol. Graph.* **1990**, *8*, 81-85.

[8] a) I. Alkorta, H. O. Villar, *J. Med. Chem.* **1994**, *37*, 210-213; b) N. El Tayar, P. A. Carrupt, H. Van de Waterbeemd, B. Testa, *J. Med. Chem.* **1988**, *31*, 2072-2081.

[9] a) M. Negri, M. Recanatini, R. W. Hartmann, *J. Comput.-Aided Mol. Des.* **2011**, *25*, 795-811; b) J. E. Mendieta-Wejebe, M. C. Rosales-Hernández, H. Rios, J. Trujillo-Ferrara, G. López-Pérez, F. Tamay-Cach, R. Ramos-Morales, J. Correa-Basurto, *J. Mol. Model.* **2008**, *14*, 537-545.

[10] a) M. K. Shukla, A. Kumar, P. C. Mishra, *J. Mol. Struct. (Theochem)* **2001**, *535*, 269-277; b) D. M. Upadhyay, M. K. Shukla, P. C. Mishra, *J. Mol. Struct. (Theochem)* **2000**, *531*, 249-266.

[11] a) K. Kadas, S. Kugler, G. Náray-Szabó, *J. Phys. Chem.* **1996**, *100*, 8462-8467; b) I. Alkorta, J. J. Perez, H. O. Villar, *J. Mol. Graph.* **1994**, *12*, 3-13.

[12] M. Adrover, C. Caldés, B. Vilanova, J. Frau, J. Donoso, F. Muñoz, *New J. Chem.* **2012**, *36*, 1751-1761.

[13] a) B. Chen, Y. Ji, M. Xue, F. R. Fronczek, E. J. Hurtado, J. U. Mondal, C. Liang, Dai, S. *Inorg. Chem.* **2008**, *47*, 5543-5545.; b) R. Dey, R. Haldar, T. K. Maji, D. Ghoshal, *Cryst. Growth Des.* **2011**, *11*, 3905-3911.; c) B. Rather, M. J. Zaworotko, *Chem. Commun.* **2003**, 830-831.

[14] L. J. Barbour, D. Das, T. Jacobs, G. O. Lloyd, V. J. Smith, *Supramolecular Chemistry: From Molecules to Nanomaterials,* John Wiley & Sons, 2012.

[15] A. P. Nelson, O. K. Farha, K. L. Mulfort, J. T. Hupp, *J. Am. Chem. Soc.* **2009**, *131*, 458–460.

[16] PLATON, *A Multipurpose Crystallographic Tool*, Utrecht University: Utrecht, The Netherlands, **2008**.

3.2. SUPPORTING INFORMATION

Materials. All materials were purchased from Sigma Aldrich and used without further processing or purification except for *N,N´-bis*-pyridine-4-ylmethylene-hydrazine, which was synthesized according to the literature procedure.[2]

Synthesis of 1, 2 and 3. The hydrothermal reaction of $Cu(NO_3)_2 \cdot 2.5H_2O$, glutaric acid (H_2glu) and L (where L = 4,4´-bipyridine [bpy], *trans-bis*(4-pyridyl)ethylene [bpe] or *N,N´-bis*-pyridine-4-ylmethylene-hydrazine [bpymh]) in H_2O at 100 °C and 60 °C for bpymh yielded three 3D metal-organic frameworks: $[Cu_2(glu)_2(bpy) \cdot 2.9H_2O]$ = **1a**, $[Cu_2(glu)_2(bpe) \cdot 3H_2O]$ = **2a** and $[Cu_2(glu)_2(bpymh) \cdot 7.5H_2O]$ = **3a**. Green block-shaped crystals of the as-synthesized frameworks were dehydrated by placing them under vacuum at 150 °C for 24 h to afford crystals of the apohosts **1**, **2** and **3**.

Supercritical CO_2 Experiments. Newly synthesized MOF crystals were exposed to supercritical CO_2 ($scCO_2$) for 24 h to obtain the apohost or activated phase. Supercritical CO_2, having properties of both liquid and gas, exerts little or no surface tension on the walls of the channels in the crystal. Depending on the solvent present in the channels and the exact conditions of temperature and pressure ($31.1 < T_c < 44$ °C; $73 < P_c < 110$ bar) (beyond the critical temperature and pressure) $scCO_2$ is able to dissolve the solvent molecules and leave behind the activated phase. Typically, a vial containing the crystals is placed directly onto dry-ice while being moved to the instruments for analysis.

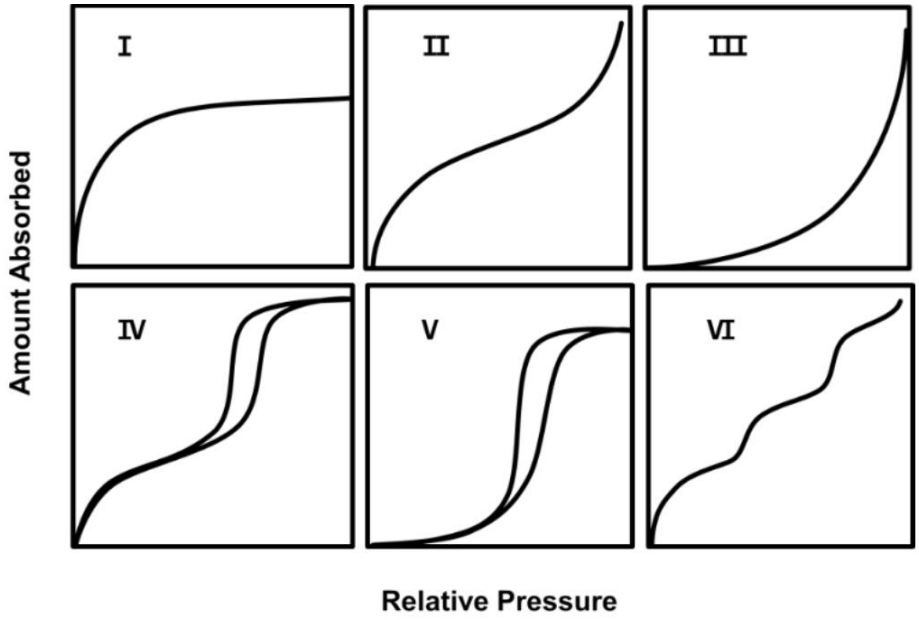

Figure S1. *Types of isotherms as described by Brunauer, Deming, Deming and Teller.*[1]

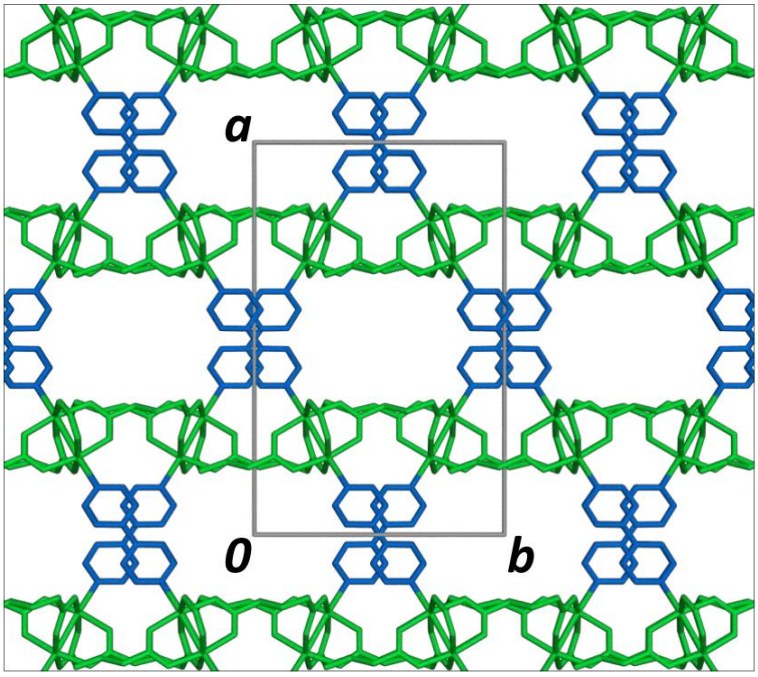

Figure S2. *Framework **1** viewed along [0 0 1] to illustrate the crisscrossed arrangement of the bipyridyl linkers.*

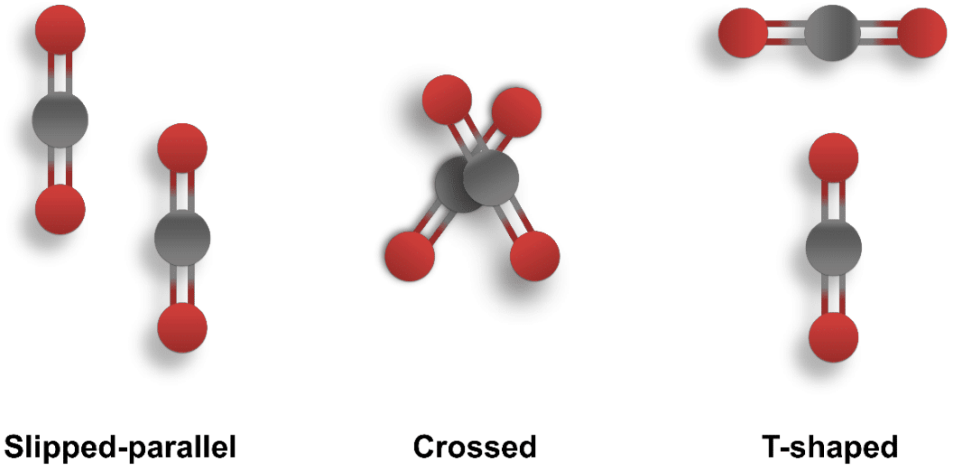

Figure S3. *The different CO_2 arrangements found in dry ice.*

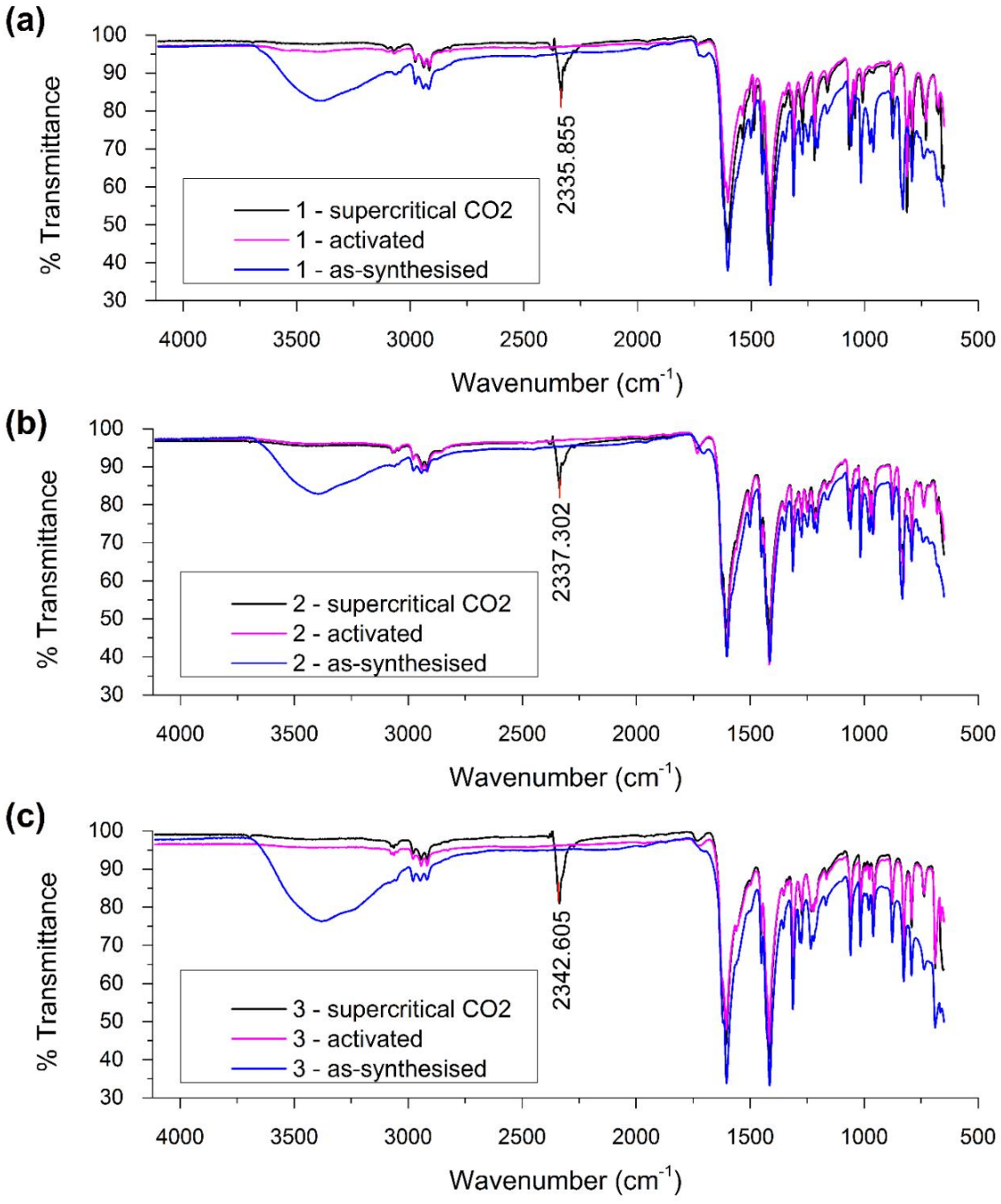

Figure S4. *Fourier transform infrared spectroscopy (FTIR) spectra of the as-synthesized, activated and supercritical CO_2 exposed materials.*

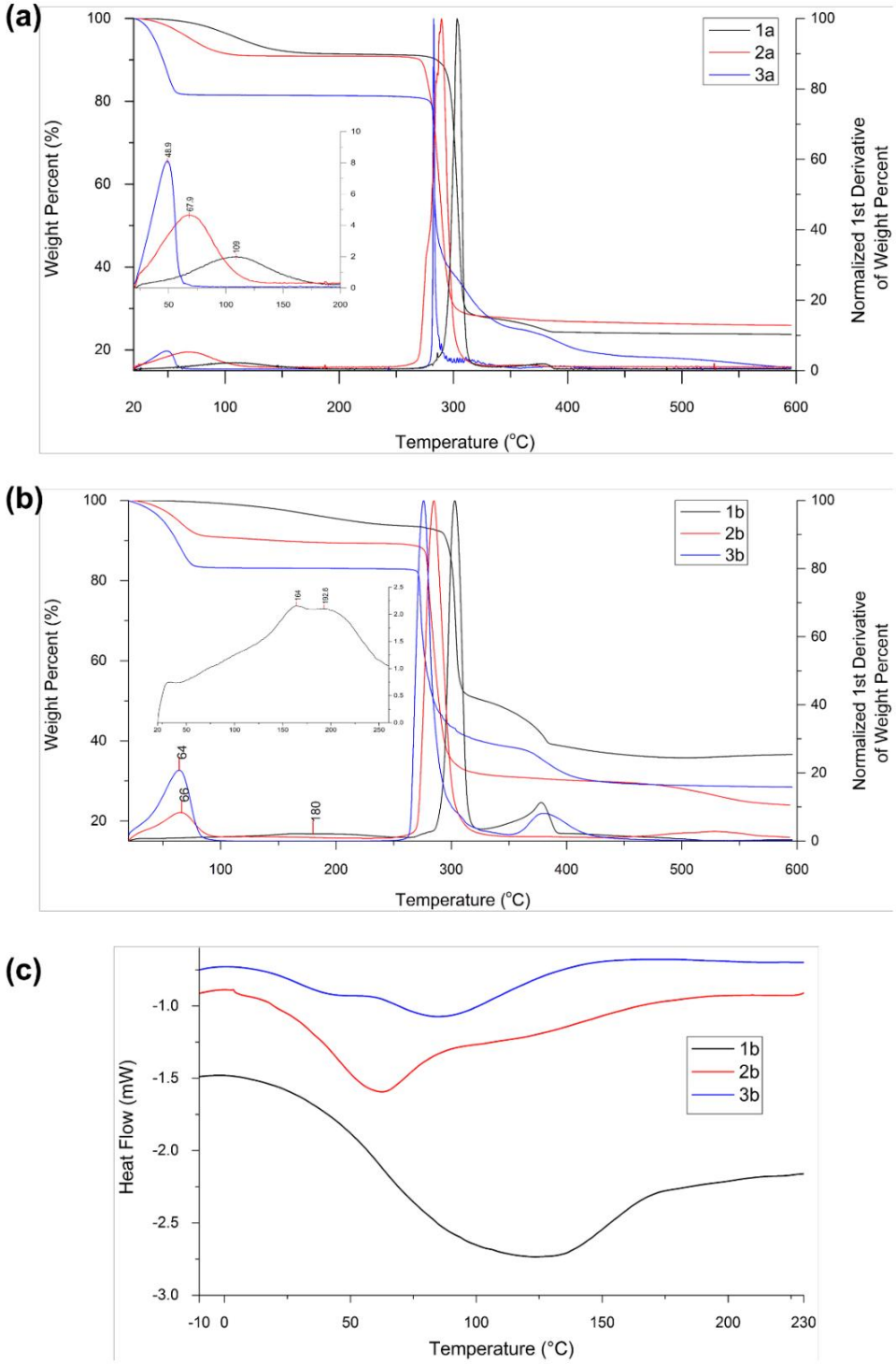

Figure S5. *Thermogravimetric analysis (TGA) and 1st derivatives of the (a) as-synthesized (**1a**, **2a** and **3a**) and (b) supercritical CO_2 exposed material (**1b**, **2b** and **3b**). The temperatures of maximum guest evolution are indicated on the 1st derivative curves. (c) Differential scanning calorimetry (DSC) thermograms of the materials exposed to supercritical CO_2: **1b**, **2b**, **3b**.*

Table S1. *Quantification of CO_2 in the three frameworks after supercritical CO_2 exposure (expressed as number of CO_2 molecules per asymmetric unit).*

	1b	2b	3b
TGA	0.512	0.765	1.39
SQUEEZE	0.505	0.92	1.38

SQUEEZE results are based on an electron count of 22 electrons per CO_2.

$$Extent\ of\ Hysteresis = \frac{AREA_{Desorption\ isotherm} - AREA_{Sorption\ isotherm}}{AREA_{Sorption\ isotherm}} \times 100\%$$

Equation E1. *The formula used for determining the percentage hysteresis of the sorption experiment (OriginPro was used to integrate the isotherm across the same pressure range to yield the areas).*

Computational Modeling. The electrostatic potential is derived from the electron density and nuclear charge as described by Eq. 1:

$$V(\boldsymbol{r}) = \sum_A \frac{Z_A}{|\boldsymbol{R}_A - \boldsymbol{r}|} - \int \frac{\rho(\boldsymbol{r}')d\boldsymbol{r}'}{|\boldsymbol{r}' - \boldsymbol{r}|} \qquad (1)$$

Since $V(\mathbf{r})$ is the interaction energy between the system and a unit positive point charge at **r** it is typically expressed in units of energy. In the case of Eq. 1, $V(\mathbf{r})$ is given in atomic units (au, Hartree), which can easily be converted to any convenient unit (kcal/mol, kJ/mol etc.). $V(\mathbf{r})$ is a 3-dimensional function which can be evaluated at any point **r** within the system with the exception of the nuclei ($\boldsymbol{R}_A \neq \boldsymbol{r}, Eq.1$).[3] These results can be mapped onto 2D planes (slices though the system under investigation) or 3D surfaces of molecules at a particular electron density contour, depending on the relevance and aspect of interest.[4] The contour utilized for the 3D surface can be defined arbitrarily, which may lead to ambiguity in the analysis of the results. In this work we use the 0.0015 au (e^-/Bohr^3, 0.01 e^-/Å^3) outer contour of the molecule's electron density ($\rho(\mathbf{r})$) as suggested by Bader *et al.*[5]

The CO_2 positions determined from the SCD structures of the crystals exposed to supercritical CO_2 were used as initial geometries to construct all the computational models. The hydrogen atoms in the framework and CO_2 molecules were first optimized as part of a periodic system using the CASTEP module of the Materials Studio software suite.[6] The optimization was performed using the GGA PBE functional with Grimme's DFT-D dispersion correction; thresholds for geometry optimization and SCF convergence were chosen as 1×10^{-6} eV. The electrostatic potentials were calculated using the VAMP module of the Materials

Studio Software suite as a single point energy calculation using the NDDO Hamiltonian type and the AM1* Hamiltonian. An SCF convergence threshold of 5×10^{-7} kcal/mol was used and the grid size for the imported electrostatic potential was set to 0.1 Å. A single point energy calculation using CASTEP (with the same parameters) on only the CO_2 molecules was also performed. The electron density data obtained from these calculations were used to construct the three dimensional 0.01 $e^-/Å^3$ electron density contours of the CO_2 molecules. CASTEP electron density data of the three frameworks were used to construct the surface of their channels as 0.01 $e^-/Å^3$ electron density contours. The electrostatic potential calculated for each framework (FEP) was then mapped onto the electron density contours of both a CO_2 molecule for each framework and their respective channel contours. The maximum and minimum values of V(r) on the surfaces, $V_{S,max}$ and $V_{S,min}$, are given in Table S2.

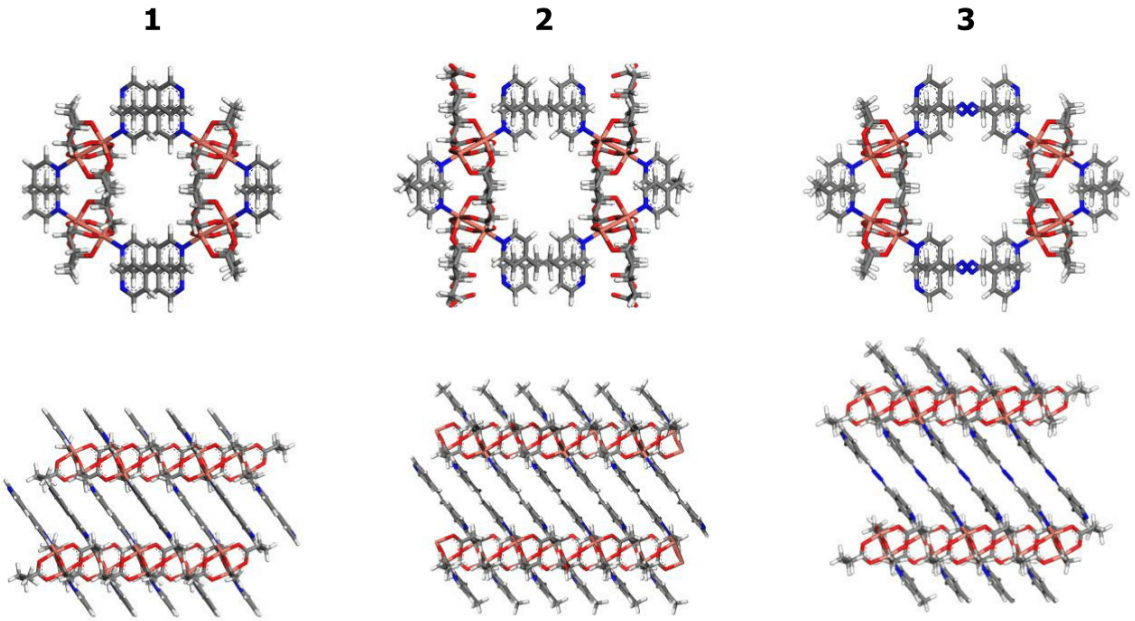

Figure S6. *The computational models used for the VAMP electrostatic potential calculations viewed along the crystallographic c axis (TOP) and the crystallographic a axis (BOTTOM) for all three frameworks.*

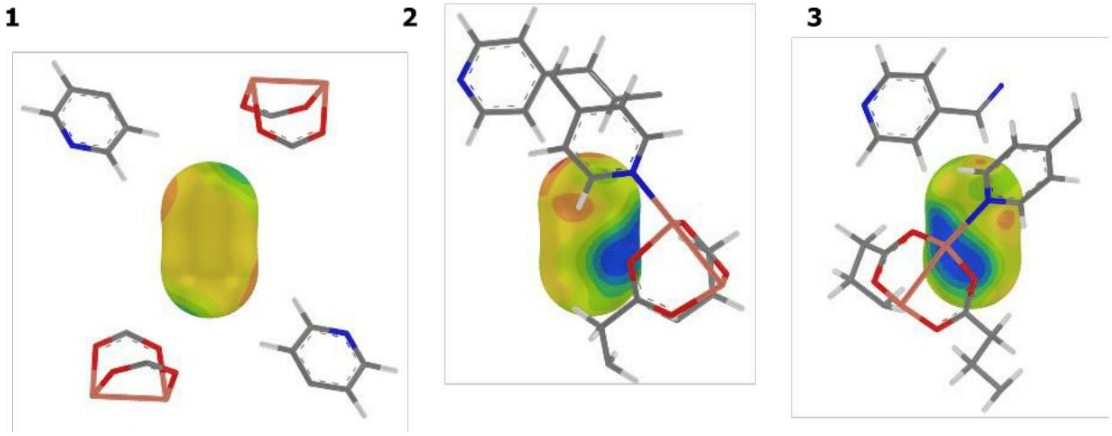

Figure S7. *Portions of the frameworks of **1**, **2** and **3** in stick representation showing the origin of the FEPs mapped onto the 0.01 $e^-/Å^3$ electron density contours of CO_2 molecules.*

Table S2. *Highest values of the electrostatic potentials of the three frameworks as mapped onto the 0.01 $e^-/Å^3$ electron density contours of the included CO_2 guest molecules (in kcal/mol).*

	FEPs (kcal/mol)								
	$V_{S,max}$						$V_{S,min}$		
	α^+	β^+	χ^+	δ^+	ε^+	ϕ^+	α^-	β^-	χ^-
1	20.65	9.73					-34.42		
2	29.70	19.90	17.96	13.10	4.37		-57.99	-16.99	-15.05
3	17.10	14.08	6.67	11.86	4.61	3.82	-61.92	-26.44	-19.41
	MEP (kcal/mol)								
	$V_{S,max}$						$V_{S,min}$		
	α^+						α^-		
CO_2 MEP	35.70						-10.84		

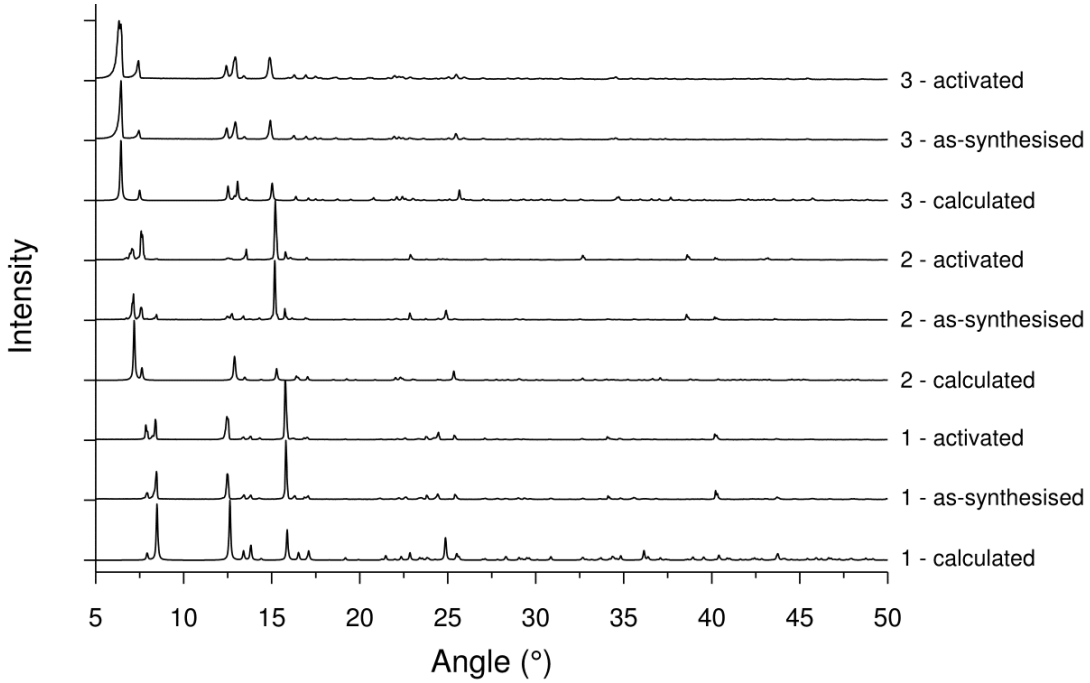

Figure S9. *Powder diffraction data of as-synthesized and activated materials of all three frameworks.*

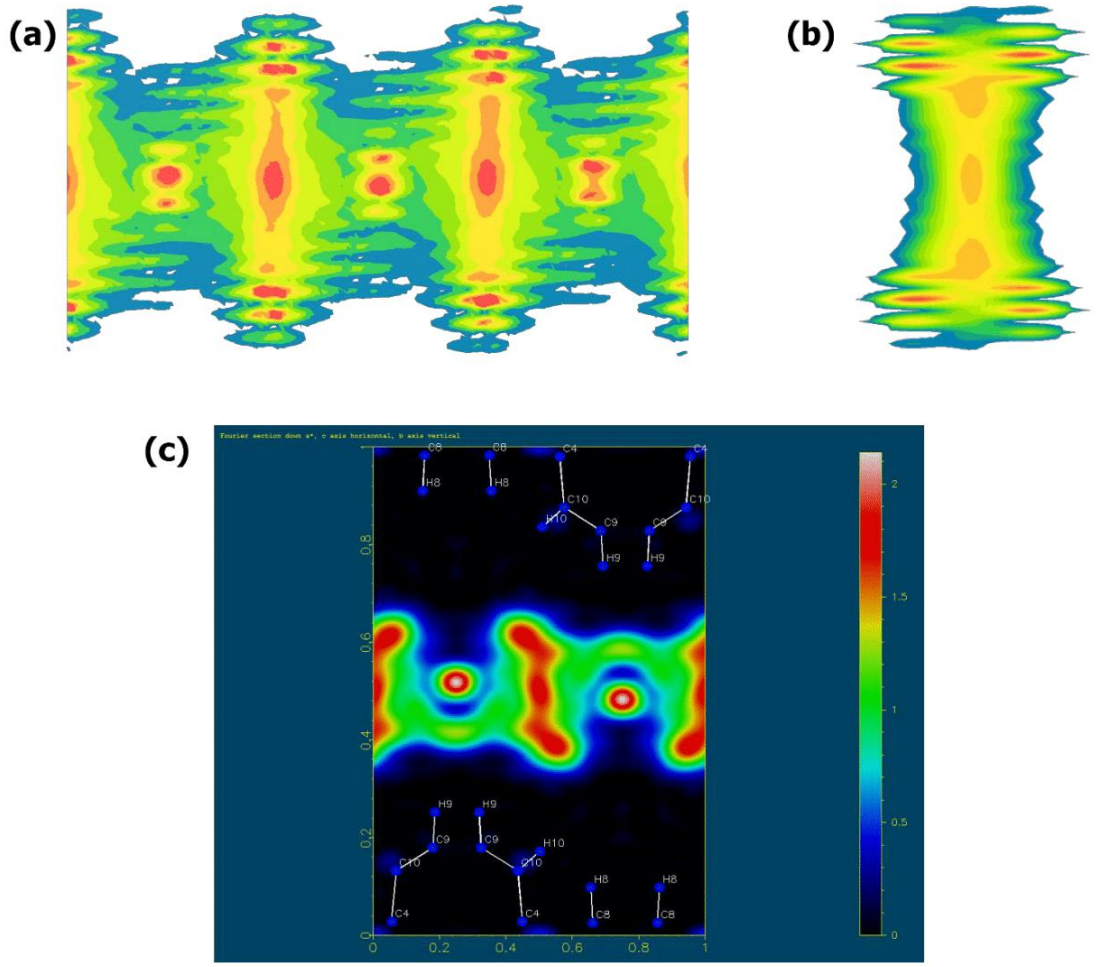

Figure S10. *2-Dimensional electron difference density map of 1b showing the electron density of the CO_2 molecules within the framework (F_o-F_c). (a) Along the crystallographic a-axis. (b) Along the crystallographic c axis. (c) 2-Dimensional electron difference density map of 1b showing the electron density of the CO_2 molecules within the framework. The scale bar on the right is in $e^-/Å^3$. Images (a) and (b) were obtained with Materials Studio using difference density data generated with WinGX V2013.3, whereas (c) was generated using WinGX V2013.3.*

Table S4. *Crystal data and structure refinement of $[Cu_2glu_2L]\cdot XCO_2$ frameworks*

	$[Cu_2(glu)_2(bpy)\cdot 0.51CO_2]$	**$[Cu_2(glu)_2(bpe)\cdot 0.77CO_2]$**	**$[Cu_2(glu)_2(bpymh)\cdot 0.29CO_2]$**
Empirical formula	$C_{10.51}H_{10}CuNO_{4.94}$	$C_{11.77}H_{11}CuNO_{5.55}$	$C_{11.29}H_{11}CuN_2O_{4.58}$
Formula weight	292.93	318.78	311.60
Temperature (K)	101(2)	100(2)	296(2)
Wavelength (Å)	0.71073	0.71073	0.71073
Crystal system	monoclinic	monoclinic	monoclinic
Space group	*C*2/*c*	*C*2/*c*	*C*2/*c*
Unit cell dimensions (Å, °)	a = 20.986(7)	a = 24.241(2)	a = 27.689(6)
	b = 13.152(5)	b = 13.2483(11)	b = 13.176(3)
	c = 8.597(3)	c = 8.5771(7)	c = 8.5800(19)
	β = 100.343(4)	β = 90.080(1)	β = 95.783(3)
Volume (Å^3)	2334.3(14)	2754.6(4)	3114.3(12)
Z	8	8	8
Calculated density (g cm^{-3})	1.667	1.537	1.329
Absorption coefficient (mm^{-1})	1.881	1.604	1.414
F_{000}	1189	1296	1267
Crystal size (mm^3)	0.27 × 0.16 × 0.11	0.35 × 0.27 × 0.25	0.15 × 0.14 × 0.10
θ range for data collection (°)	1.97 to 28.39	1.68 to 28.72	1.71 to 28.68
Miller index ranges	$-27 \le h \le 28$, $-17 \le k \le 17$, $-11 \le l \le 6$	$-19 \le h \le 32$, $-15 \le k \le 17$, $-11 \le l \le 11$	$-36 \le h \le 37$, $-12 \le k \le 17$, $-9 \le l \le 11$
Reflections collected	6800	8740	9575
Independent reflections	2688 [Rint = 0.0175]	3296 [R_{int} = 0.0314]	3690 [R_{int} = 0.0321]
Completeness to θ_{max} (%)	91.5	92.6	91.8
Max. and min. transmission	0.7955 and 0.5110	0.6919 and 0.6030	0.8762 and 0.8127
Refinement method	Full-matrix least-squares on F^2	Full-matrix least-squares on F^2	Full-matrix least-squares on F^2
Data / restraints / parameters	2688 / 23 / 155	3296 / 0 / 182	3690 / 0 / 191
Goodness-of-fit on F^2	1.135	1.077	1.083
Final R indices [$I > 2\sigma(I)$]	*R1 = 0.0357, wR2 = 0.1069*	$R1$ = 0.0320, $wR2$ = 0.0889	$R1$ = 0.0386, $wR2$ = 0.1028
R indices (all data)	*R1 = 0.0399, wR2 = 0.1103*	$R1$ = 0.0357, $wR2$ = 0.0912	$R1$ = 0.0469, $wR2$ = 0.1072
Extinction coefficient	none	none	none
Largest diff. peak and hole (e Å^{-3})	1.451 and -0.431	0.701 and -0.380	1.124 and -0.551

Chapter 4

SOLVENT AND PRESSURE-INDUCED PHASE CHANGES IN TWO 3D COPPER GLUTARATE BASED MOFS VIA GLUTARATE (+*GAUCHE* ⇋ -*GAUCHE*) CONFORMATIONAL ISOMERISM.

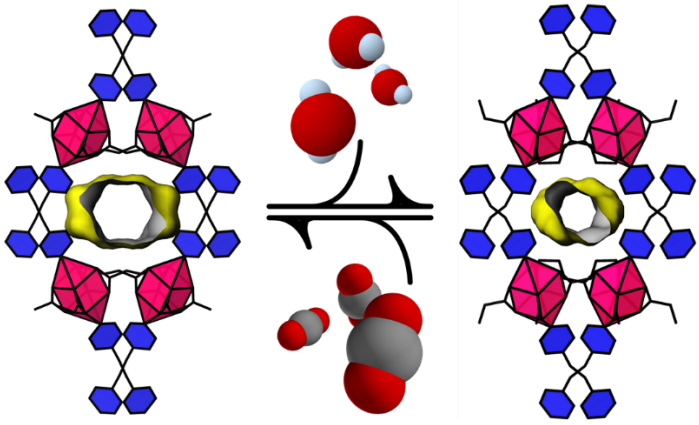

4.1. FULL ARTICLE IN JOURNAL OF THE AMERICAN CHEMICAL SOCIETY (ACCEPTED AND REVISED)

Contributions of the author:

- Design of project with Dr Vincent J. Smith
- Preparation of MOFs
- Supercritical CO_2 experiments
- Collection of single-crystal X-ray data and refinement of single-crystal X-ray structures
- Recording of PXRD patterns, TGA thermograms and FRIR spectra
- Sorption analysis
- Computational modelling
- Interpretation of results with Dr Vincent J. Smith
- Writing the first draft of the article

Solvent and Pressure-Induced Phase Changes in Two 3D Copper Glutarate-Based MOFs via Glutarate (+*gauche* ⇋ –*gauche*) Conformational Isomerism.

Charl X. Bezuidenhout, Vincent J. Smith, Catharine Esterhuysen* and Leonard J. Barbour*

Department of Chemistry and Polymer Science, University of Stellenbosch, Matieland, 7602, South Africa

KEYWORDS: gauche rotamers, phase-change, high pressure sorption, carbon dioxide, potential energy scan.

ABSTRACT: Two isoreticular 3D Cu(II)-glutarate based pillared-layered MOFs with flexible pillars, $[Cu_2(glu)_2(bpa)]$ and $[Cu_2(glu)_2(bpp)]$ (bpa - 1,2-bis(4-pyridyl)ethane, bpp - 1,3-bis(4-pyridyl)propane), undergo spontaneous phase changes upon solvent loss at room temperature. Using single-crystal X-ray diffraction analysis (SCXRD), we show that the phase changes result in new narrow-channel forms that experience a large reduction in solvent-accessible volume. Moreover, the $[Cu_2(glu)_2(bpa)]$ MOF displays a stepped sorption isotherm for the uptake of CO_2 at RT. This is indicative of the framework reverting to the wide-channel form under CO_2 pressure. Supercritical CO_2 was used to isolate the gas-included structures and, by means of single-crystal X-ray diffraction analysis we were able to determine the positions of the CO_2 molecules in the channels of the frameworks. Finally, we report the use of molecular modelling simulations to elucidate the phase-change mechanism, including the energetic changes involved. Structural limitations in both MOFs allow for only direct *gauche-gauche* enantiomeric interconversion of the glutarate moieties.

INTRODUCTION

The vast structural versatility of metal-organic frameworks (MOFs) is due to the myriad potential combinations of metal ions and coordinating organic ligands.[1-5] A variety of metal ions form recurring secondary building unit (SBUs) motifs that allow for rational design of new materials from new and existing organic building blocks (i.e. reticular synthesis).[6-9] These recurring SBUs are essential in the design of isoreticular MOFs and are crucial to the systematic study of the physical properties of MOFs,[8, 10-12] particularly the preparation of stable (rigid), porous MOFs with wide-ranging topologies.[5, 13] Rigid exo-polydentate aromatic carboxylic acids and pyridyl-based ligands are the most widely employed linkers in the exploration of new MOFs.[1, 4, 8, 13-15]

In recent years there has been a shift towards soft porous materials that can distort or even change phase upon gas uptake.[16-20] These types of materials have demonstrated high uptake capacity and selectivity for gases that induce the structural change.[21-23] Bousquet *et al.*[24] and Coudert *et al.*[25] have described different modes of flexibility in MOFs: breathing, swelling, linker rotation, subnetwork displacement (in catenated MOFs) and slippage of interdigitated and stacked layers.[18, 24-27] These modes of flexibility greatly affect the sorption behavior of the materials and generally give rise to stepped sorption profiles.[28-31] An inflection is usually associated with a structural transformation from a narrow-pore to a wide-pore phase and the sudden increase in guest-accessible space results in increased gas uptake.[21, 32-34] For a given material, these gate-opening events tend to depend on three factors: the nature of the gas, the temperature and the pressure.[35-37] The relationship between these factors, as well as the mechanisms that govern gate opening, are still active topics of study.[18, 38-39]

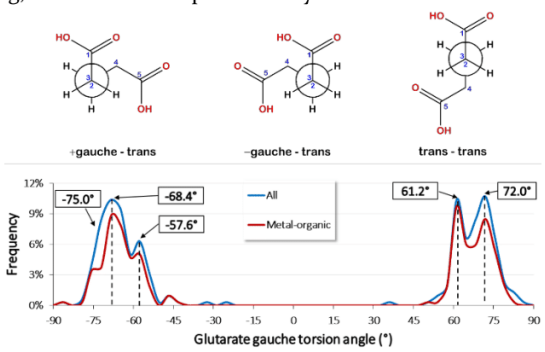

Figure 1. Newman projections (top) of glutaric-acid (H_2glu) rotamers generated around the C2-C3 bond and the frequency plot (bottom) of the glu C2-C3 *gauche* torsion angles from 318 structures in the CSD.[40]

Conformational isomerism of bridging ligands is also possible and is associated with either breathing or linker rotation. Most attempts to produce flexible MOFs using aliphatic dicarboxylic acids generally lead to polymorphs or structural isomers containing different conformations of the organic ligands.[27] Once crystallized, the conformation

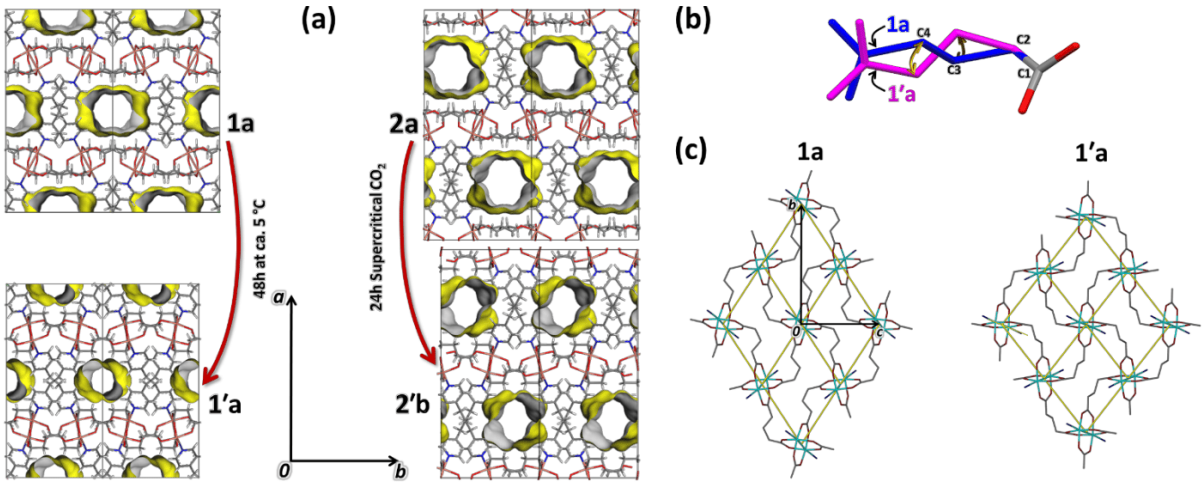

Figure 2. (a) The crystal structures of **1a**, **1′a**, **2a** and **2′b** viewed along [0 0 1] (guest molecules omitted for clarity). The channel Connolly surface, generated with a probe radius of 1.4 Å, is shown in yellow. The structures are shown at the same scale. (b) Overlay of the glu moieties in **1a** and **1′a**. The yellow arrow indicates twisting of the C3-C4 bond as **1a** transforms to **1′a**. (c) Cu-glu 2D layer of **1** and **1′a** viewed along [1 0 0] with a grid (yellow) produced by connecting centroids generated from each paddlewheel copper pair (**2** and **2′b** are similar). Hydrogen atoms have been omitted for clarity in (b) and (c).

of the flexible aliphatic backbone is locked in by close contacts and M-L coordination.[41-42] Recently, Reinsch *et al.* synthesized a MIL-53-type MOF using adipic acid, where the change in pore volume was attributed to conformational isomerism of the adipate linkers. However, in that case the length of the linker in the large-pore structure is shorter than that in the narrow-pore structure,[43] but the authors did not comment on the relationship between conformational isomerism and pore volume.

Glutaric acid is another example of a flexible dicarboxylic acid that could be used as a linker in MOFs. In 2003 Zaworotko *et al.* surveyed the Cambridge Structural Database (CSD)[40] for the conformations of glutarate (glu) anions in coordination compounds.[44] They identified 30 structures and noted that the glutarate moiety exhibits three conformations (or rotamers): *trans-trans* (tt), *gauche-trans* (gt) and *gauche-gauche* (gg), where the *gauche* conformation can either be +*gauche* or –*gauche*, depending on the C1-C2-C3-C4 torsion angle (Figure 1, top).

We repeated the survey using version 5.37 of the CSD (November 2015 with February and May 2016 updates) and identified 318 relevant structures. A plot of the torsion angle frequency distribution (Figure 1, bottom) shows a broad peak with two maxima for both +g and –g. Variation of approximately 30° is evident and serves to highlight the most common angles that the *gauche* rotamers adopt for the reported coordination compounds. The observed behavior of the glu ligand may lead to structural flexibility in MOFs, provided there are no inhibiting constraints. Here we present an investigation of the solvent and pressure-induced phase changes of two previously reported 3D Cu-glu based MOFs that are pillared by flexible bipyridyl ligands.

RESULTS AND DISCUSSION

Synthesis and structural description. The linker 1,2-bis(4-pyridyl)ethane (bpa) was reacted with $Cu(NO_3)_2{\cdot}2.5H_2O$ and glutaric acid (H_2glu) under hydrothermal conditions to yield $[Cu_2(glu)_2(bpa)]_n{\cdot}2.4H_2O$ (**1a**)[45] while 1,3-bis(4-pyridyl)propane (bpp) was reacted with $Cu(NO_3)_2{\cdot}2.5H_2O$ and glutaric acid using the layering method in acetone (ace) to produce $[Cu_2(glu)_2(bpp)]_n{\cdot}2ace$ (**2a**) (Scheme S1).[45-46] Both methods yielded green prismatic crystals from which suitable specimens were selected for single-crystal X-ray diffraction analysis (SCXRD) at 100 K. **1a** crystallizes in the monoclinic space group *C*2/*c* and **2a** crystallizes in the orthorhombic space group *Pccn* (Table S1). In each case the framework structure consists of 2D corrugated layers with Cu-glu paddlewheel SBUs as nodes. The bipyridyl ligands coordinate to the axial sites of the paddlewheel SBUs, crisscrossing one another, and joining adjacent 2D corrugated layers to form a 3D MOF (Figure 2a top). Both frameworks contain 1D corrugated channels and the networks are related to the α-polonium net.

Phase change behavior. Crystals of **1a** were allowed to desolvate at ca 5 °C. A single crystal of sufficient quality was selected for SCXRD analysis, which revealed that the structure had undergone a phase change to **1′a**, $[Cu_2(glu)_2(bpa)]_n{\cdot}0.93H_2O$ (Figure 2a). The same procedure for **2a** yielded a polycrystalline material, **2′a**. However, it was possible to isolate a new phase as single crystals using supercritical CO_2 (SC-CO_2) activation (see ESI for details) and the corresponding crystal structure **2′b**, $[Cu_2(glu)_2(bpp)]_n{\cdot}8.2CO_2$ (Figure 2a) was determined by SCXRD analysis. We refer to the guest-free (virtual)[47] framework structures of **1′a** and **2′b** as **1′** and **2′**, respectively. They are the narrow-channel (nc) forms while **1** and

2 (the host frameworks of **1a** and **2a**, respectively) are the wide-channel (wc) forms (Figure 2a and Table S2). The dimensions of the wide channels are 8.202 × 5.853 Å (**1**) and 9.077 × 7.385 Å (**2**), while those of the narrow channels are 7.026 × 4.711 Å (**1′**) and 7.830 × 6.393 Å (**2′**). There is a relatively large decrease by 44% in the solvent-accessible volume during the conversion of **1** (520 Å^3) to **1′** (281 Å^3), as compared to the 22% change during the conversion from **2** (749 Å^3) to **2′** (490 Å^3) (see Figure 2a and Table S1). The most significant changes in the unit cell dimensions for both **1**→**1′** and **2**→**2′** are evident in the *b* and *c* axes; the *b* axis shrinks while the *c* axis expands in concert with the changes in channel dimensions (Table S1). During the phase change the signs of the torsion angles of the glu *trans* (t) and *gauche* (g) moieties become inverted – i.e. all the negative torsion angles become positive and *vice versa* (Figure 2b and Figure S1). The inversion of the signs of the glu *gauche* torsion angles indicate an enantiomeric conformational change (+g and –g are mirror images, Figure 2b). The glu ±g torsion angles (±57.5 (**1**), ∓75.7 (**1′**), ±59.2 (**2**) and ∓77.1 (**2′**)) compare well with the peak frequencies observed for the glu ±g torsion angles reported here and in the CSD survey of Zaworotko *et al.* (Figure 1 and Table S3).[44] Related changes occur in the orientation of the Cu-glu paddlewheel SBUs (Figure 2c, S2 and Table S3). MOFs isoreticular to **1** and **2** that contain rigid bipyridyl linkers do not appear to undergo phase changes[44-46, 48-55] and it is therefore plausible that the flexibility of the bpa and bpp linkers, compared to rigid analogues, is crucial in accommodating these structural changes. In the case of bpa (**1**→**1′**), an increase in the scissor-angle and ligand inclination (relative to the *ab*-plane) results in shortening of the *a* axis (Figure 3a, b and Table S4). Similarly, during the transformation **2**→**2′**, bpp experiences a decrease in the ligand bend angle and an increase in the scissor angle (Figure 3c, d and Table S4).

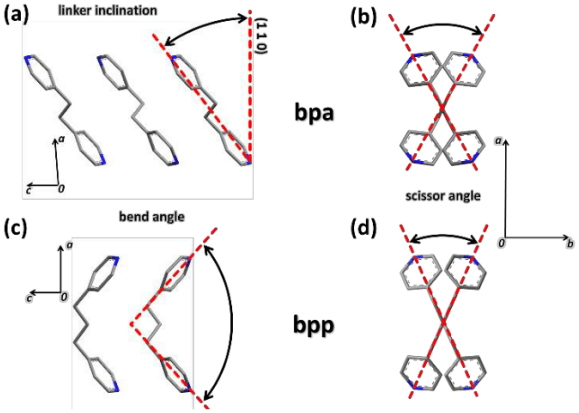

Figure 3. (a) Inclination of the bpa linker relative to (110). (b) Scissor angle formed by the bpa linkers. (c) Bend angle of the bpp linker. (d) Scissor angle formed by the bpp linkers.

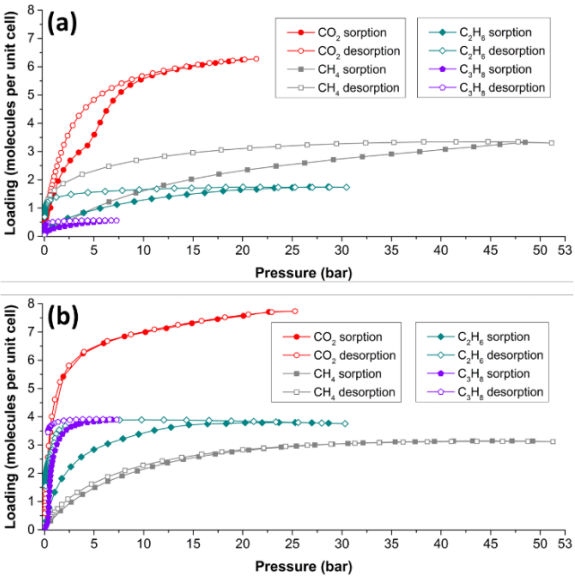

Figure 4. Gas sorption isotherms, recorded at 298 K, for (a) **1′** and (b) **2′**.

Gas sorption studies. Thermogravimetric analysis of **1a** and **2a** showed that complete solvent loss occurs before 100 °C (Figure S3); activation was carried out under dynamic vacuum at 150 °C. Powder X-ray diffraction (PXRD) analysis shows that the activated phases match those simulated for guest-free **1′a** and **2′b** (Figures S4 and S5), confirming that they comprise the nc frameworks **1′** and **2′** (the PXRD traces were indexed using the TOPAS 4.2[56] software package; see Tables S5 and S6). Gas sorption experiments were carried out at 25 °C using **1′** and **2′** (Figure 4). Sorption/desorption hysteresis was observed for all of the investigated gases in the case of **1′** (Figure 4a), and also for C_2H_6 and C_3H_8 in the case of **2′** (Figure 4b). The isotherms for CO_2 and CH_4 sorption by **2'** are characteristic of microporous materials (Figure 4b). For both materials, the maximum molar CO_2 sorption capacity is twice that measured for the other gases. Moreover, **1′** appears to exhibit a gate-opening event between 4 – 5 bar during CO_2 adsorption but, unusually, a corresponding inflection for a gate closing event is not apparent in the desorption isotherm (Figure 4a). The CO_2 loading for **1′** tends towards 4 molecules per unit cell before the gate-opening event, and thereafter towards 8 molecules per unit cell. A gate-opening event is usually associated with a phase change and could be a transformation from **1′** to **1**.[29, 38] The solvent accessible space for **1** is almost double that of **1′**, which is consistent with the observed doubling in CO_2 occupancy after the gate-opening event.

The CO_2 loaded crystal structures, **1b** and **2′b** (Figure 5), were obtained via solvent exchange using SC-CO_2 (see ESI for details), where the presence of CO_2 was confirmed using FTIR spectroscopy[57-58] (Figure S6). The simulated powder pattern for virtual guest-free **1b** matched that recorded for guest-free **1a**, implying that SC-CO_2 exposure does not change the host structure. This observation is consistent with the lack of a gate-closing event in the CO_2

desorption isotherm for **1′**, i.e. **1b** remains in the wc form. According to SCD data recorded for **1b** approximately 5 minutes after removal from SC-CO_2 the CO_2 occupancy, determined using SQUEEZE,[59-60] is ca 1 molecule per unit cell. However, when another crystal was selected and data collected more rapidly, the CO_2 occupancy was determined to be approximately 9 molecules per unit cell. These observations imply that CO_2 is lost rapidly under ambient conditions. The total guest-accessible volume per unit cell of **1** is 503 Å^3. The nc form (**1′**) has significantly less guest-accessible space (281 Å^3 per unit cell), as compared to **1b.**

The simulated PXRD pattern of virtual guest-free **2′b** matches the pattern recorded for **2′** (Figure S5). The absence of a gate-opening event for CO_2 adsorption is consistent with the crystal structure **2′b** (Figure 5b). The SQUEEZE electron count for **2′b** indicates 8.2 CO_2 molecules in the unit cell, which could be modelled over 10 positions with partial occupancies and without any structural constraints. The CO_2 molecules in both **1b** and **2′b** utilize sorption sites and guest-guest orientations similar to those identified in our previous work.[58] Additional slipped-parallel CO_2—CO_2 interactions are also present in the case of **2′b** (Figure 5b and Figure S8). The phase changes occurring in **1** and **2** were further investigated using a computational approach, first by studying the result of rotation around the C1-C2-C3-C4 torsion angle (Figure 1) on an individual glutarate linker, and then by extending this procedure to determine the effect on the crystal structure of the MOF. The gate-opening event in **1′** and absence thereof in **2′** was confirmed using pressure-ramped differential scanning calorimetry P-DSC (Figure S7).

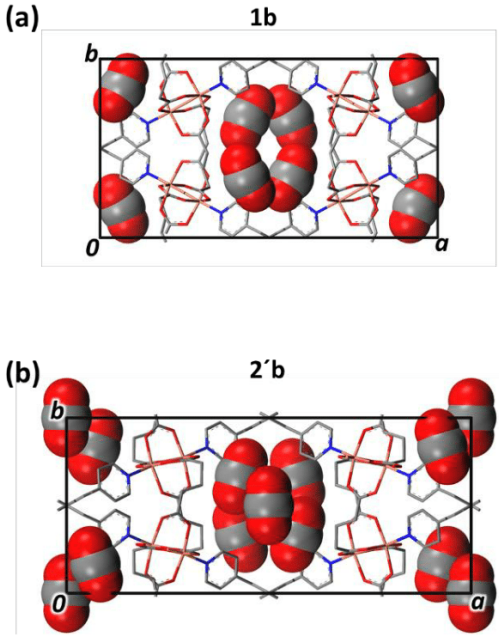

Figure 5. Crystal structures of **1b**, (a), and **2′b**, (b), viewed along the crystallographic *c* axis. Hydrogen atoms have been omitted for clarity and the CO_2 molecules are shown in space-filling representation.

Computational Study. The largest structural changes during the phase transitions involve the glu linkers, particularly the *gauche* torsion angle (Table S3). In order to investigate this further we focused on a single glutaric acid molecule (H_2glu). A conformational scan of the H_2glu *gauche* torsion angle was carried out using DFT methods (see Figure 6a and ESI for details). The scan consisted of a 250° sweep with a 5° step size (Figure 6b). The relative energy plot generated from the scan shows minima at 60° (**B**: +g) and -70° (**D**: −g) with an expected *cis*-barrier at 0° (**C**, when atoms C1 and C4 involved in the torsion angle are eclipsed).[61-63] The torsion angles of the ±g rotamers for the H_2glu molecule compare well with those determined from the crystal structures (Table S3). The *cis*-barriers for moving between the two rotamers are 4.4 kcal mol^{-1} (**B**→**D**) and 5.4 kcal mol^{-1} (**D**→**B**). These energy values are similar to those determined for other molecules with aliphatic backbones (4 – 8 kcal mol^{-1}).[63-64] The asymmetry in the relative potential energy plot is due to the asymmetry in the carboxylic acid functional group (-COOH) (Figure 6a).This indicates that the phase transition could simply be an enantiomeric conversion between the two *gauche* glutarate rotamers.

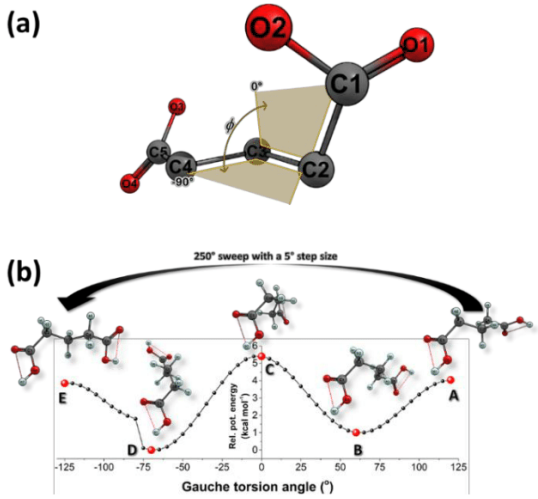

Figure 6. (a) Computational model used in the DFT level calculations for glutaric acid. The C1—C2—C3—C4 *gauche* torsion angle is the scan parameter in these calculations. (b) The relative potential energy plot of a DFT-based torsional scan using a single H_2glu model.

To confirm this, we investigated the effect of the conformational change of the glu moieties on the Cu-glu 2D grid (Figure 2c and Figure S2) using a larger computational model that consists of 4 paddlewheel units connected by 4 glu ions to form a parallelogram (Figure 7). A conformational scan of the glu torsion angles was carried out (similarly to the previous scan) using molecular mechanics (MM, see ESI for details). The scan was only performed through the *cis*-barrier (0°, Figure 7). With reference to Figure 7, the vertical diagonal of the parallelogram is equivalent to the crystallographic *c* axis, whereas the horizontal diagonal corresponds to the *b* axis. The simulation yielded

changes in the vertical (increase) and horizontal (decrease) diagonals that correspond to the changes in the *b* and *c* axes for wc→nc (Figure S9). The molecular models at the minima **A** (±g, wc) and **E** (∓g, nc) (Figure 7) were overlaid, revealing significant differences in the orientations of the paddlewheel SBUs (Figure S10, Video S1). This is consistent with the structural observations from SCXRD (Table S1) and also highlights the requirement for some flexibility within the bridging pyridyl ligands and/or the ability of the metal—ligand coordination bond to deform.

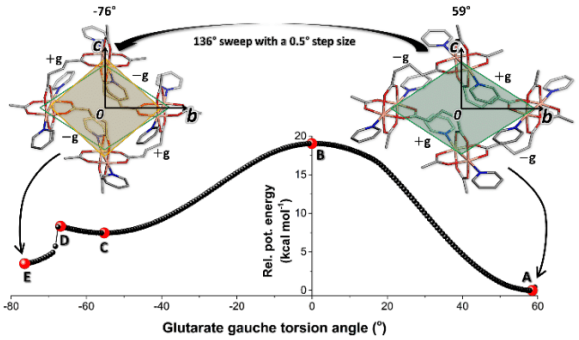

Figure 7. The glutarate ±g↔∓g (+*gauche*→−*gauche* and −*gauche*→+*gauche*) torsional potential energy scan using a larger model and calculated using DMol³. The *gauche* torsion angle, scan sweep and step size used in the computational simulations are indicated. A plot of the relative energies is shown, along with a few key structures (indicated by the **red** spheres). The green and yellow parallelograms represent the wide (59°) and narrow (-76°) channel forms, respectively.

Table 1. Experimental and simulated unit cell parameters of **1**, **1′**, **2** and **2′**, including the relative differences (rel. diff.) between the unit cell parameters of the wc and nc forms.

	Experimental			Simulation		
	1	**1′**	Rel. diff.	**1**(A)	**1′**(E1)	Rel. diff.
	*C*2/*c*	*C*2/*c*		*C*2/*c*	*C*2/*c*	
a /Å	24.717(16)	23.720(9)	-0.997	24.978	24.804	-0.174
b/Å	13.233(8)	11.800(4)	-1.433	12.926	11.484	-1.442
c/Å	8.623(6)	9.239(4)	0.616	8.494	9.099	0.605
β/°	91.837(8)	90.476(4)	-1.361	91.67	90.94	-0.73
	2	**2′**	Rel. diff.	**2** (A)	**2′** (E1)	Rel. diff.
	Pccn	*Pccn*		*Pccn*	*Pccn*	
a/Å	27.615(2)	27.380(6)	-0.285	28.008	27.728	-0.280
b/Å	12.903(1)	11.837(3)	-1.565	12.647	11.485	-1.212
c/Å	8.573(1)	9.119(2)	0.546	8.566	9.066	0.500

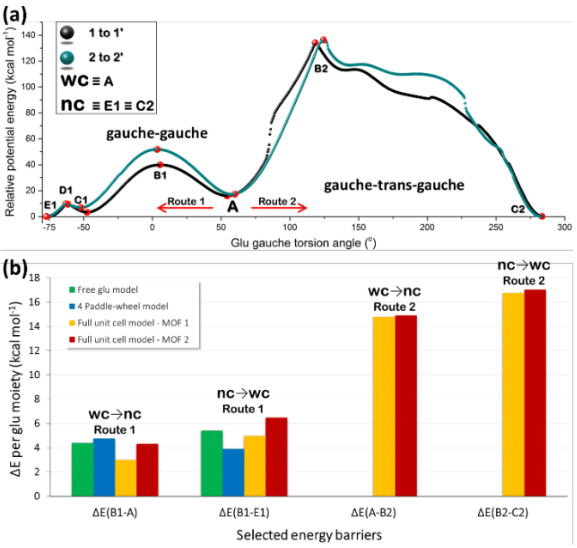

Figure 8. (a) MM simulated glu torsion angle scan using a full unit cell computational model. The two pathways for transforming the wc forms to the nc forms are indicated (**Route 1**: A→E1, **Route 2**: A→C2). A few key positions are indicated by the **red** spheres. (b) Bar graph showing the energy barriers for the potential energy scans of all the computational models.

The *gauche* torsion angle can change from ±g → ∓g via two routes: direct interconversion (±g ⇋ ∓g, Route 1) or via the *trans* route (±g ⇋ t ⇋ ∓g, Route 2). Both of these routes were simulated using a complete unit cell as the computational model (Figure S11). The MM calculations were carried out in the space group *P*1 by scanning the *gauche* glu torsion angles and optimizing the entire unit cell. The unit cell contains eight glu moieties that were scanned simultaneously with a step size of 0.5° for both routes. The unit cell parameters of the experimental and simulated wc (initial minima) and nc (final minima) structures are different but still comparable (Table 1). The relative differences between **1** and **1′** compare very well for the experimental and simulated structures along the *b* and *c* axes. The simulated *a* axis and β angle have relative differences that are smaller in magnitude than those of the experimental structures, but still with the correct trend. In the case of **2** there is good agreement between the experimental and simulated unit cells. The relative differences are similar in both magnitude and direction of change (Table 1). This demonstrates that the phase change is adequately simulated by merely scanning the *gauche* glu torsion angles.

The energy barrier for Route 2 (*trans* route) is significantly higher than for Route 1 (direct route) for both 1 and 2 (Figure 8a). MOF **1** has energy barriers of 2.99 and 4.99 kcal mol⁻¹ for Route 1 and 14.77 and 16.77 kcal mol⁻¹ for Route 2, while MOF **2** has energy barriers of 4.32 and 6.47 kcal mol⁻¹ for Route 1 and 14.9 and 17.04 kcal mol⁻¹ for Route 2 (Figures 8b, Table S7). This indicates that the phase change in each MOF occurs via a direct *gauche*-to-*gauche* interconversion (±g ⇋ ∓g). The ±g ⇋ ∓g energy barriers for **2** are 1.33 kcal mol⁻¹ (**A→B1**: wc→nc) and 1.48 kcal mol⁻¹

(**E1→B1**: nc→wc) higher than those for **1** (Table S7). The higher nc→wc energy barrier of **2** and the efficient packing of CO_2 molecules within the channels of its nc form (**2′b**) explain the absence of a gate-opening event in the CO_2 sorption by **2′**. The wc form (**A**) has a higher relative potential energy compared to the nc forms (**E1** and **C2**). The atoms in the nc form are in closer proximity to one another, resulting in an increase in van der Waals interactions and the stability of the MOFs. Simulations that illustrate how the flexible bpa and bpp ligands distort in order to accommodate the changes in the Cu-glu paddlewheel orientations are provided in the ESI (Videos S2 and S3).

CONCLUSIONS

We have obtained newly identified nc phases for the two previously reported frameworks **1** and **2**. The phase changes occur spontaneously upon solvent loss at room temperature. The crystal structures for both phases reveal an enantiomeric conformational change in the glu moieties through inversion of the *gauche* torsion angles. The distance between the carboxylate functional groups can be different depending on the conformation of the aliphatic chain: for instance, the *trans-trans* conformer of glu is more extended than the *gauche-gauche* conformer. However, even though the +g and –g conformers have the same effective length, the change from +g to –g gives rise to the observed phase change in each MOF. The changes in orientation, bend angles and coordination angle of the 4,4′-bipyridyl linkers suggest that these moieties play a crucial role in accommodating the glu conformational change. The activated MOF **1′** shows a gate-opening event at 4 bar CO_2 gas pressure, opening up from the nc form to the wc form.

Computational simulation revealed that the phase change is due to a direct *gauche-gauche* enantiomeric conversion. The flexible bipyridyl ligands are crucial in accommodating the variations in the Cu-glu paddlewheel orientation and thus allowing the conversion to occur. Furthermore, the energy barrier for Route 1 is ca 10 kcal mol^{-1} (per glu moiety) more stable than for Route 2. Additionally, the energy barriers for Route 1 for MOFs **1** and **2** are in the same range as that of a free H_2glu molecule (3 – 7 kcal mol^{-1}). These energies are comparable to those of reported conformational barriers for molecules such butane and its derivatives, which spontaneously interconvert under ambient conditions.

ASSOCIATED CONTENT

Supporting Information. Experimental details, Computational details, additional analysis, and figures (PDF).

Crystallographic details for **1a** (CIF)

Crystallographic details for **1b** (CIF)

Crystallographic details for **1'a** (CIF)

Crystallographic details for **2a** (CIF)

Crystallographic details for **2'b** (CIF)

Periodic optimized geometries for **1** and **2** (CIF)

This material is available free of charge via the Internet at http://pubs.acs.org.

AUTHOR INFORMATION

Corresponding Authors

*ljb@sun.ac.za, ce@sun.ac.za

ORCID

Charl X. Bezuidenhout: 0000-0002-9956-6279
Vincent J. Smith: 0000-0003-3546-3884
Catharine Esterhuysen: 0000-0002-0135-2118
Leonard J. Barbour: 0000-0002-6453-8331

Notes

The authors declare no competing financial interest.

ACKNOWLEDGMENT

CXB, LJB, CE and VJS thank the National Research Foundation (NRF) of South Africa and Stellenbosch University for financial support, as well as the Centre for High Performance Computing (CHPC) in Cape Town for the use of their resources.

REFERENCES

(1) James, S. L., *Chem. Soc. Rev.* **2003**, *32*, 276-288.
(2) Cook, T. R.; Zheng, Y.; Stang, P. J., *Chem. Rev.* **2013**, *113*, 734-777.
(3) Meek, S. T.; Greathouse, J. A.; Allendorf, M. D., *Adv. Mater.* **2011**, *23*, 249-267.
(4) Qiu, S.; Zhu, G., *Coord. Chem. Rev.* **2009**, *253*, 2891-2911.
(5) Stock, N.; Biswas, S., *Chem. Rev.* **2012**, *112*, 933-969.
(6) Li, H.; Eddaoudi, M.; O'Keeffe, M.; Yaghi, O. M., *Nature* **1999**, *402*, 276-279.
(7) O'Keeffe, M.; Peskov, M. A.; Ramsden, S. J.; Yaghi, O. M., *Acc. Chem. Res.* **2008**, *41*, 1782-1789.
(8) Eddaoudi, M.; Kim, J.; Rosi, N.; Vodak, D.; Wachter, J.; O'Keeffe, M.; Yaghi, O. M., *Science* **2002**, *295*, 469-472.
(9) Eddaoudi, M.; Moler, D. B.; Li, H.; Chen, B.; Reineke, T. M.; O'Keeffe, M.; Yaghi, O. M., *Acc. Chem. Res.* **2001**, *34*, 319-330.
(10) Liu, J.; Lukose, B.; Shekhah, O.; Arslan, H. K.; Weidler, P.; Gliemann, H.; Bräse, S.; Grosjean, S.; Godt, A.; Feng, X.; Müllen, K.; Magdau, I.-B.; Heine, T.; Wöll, C., *Sci. Rep.* **2012**, *2*, 921.
(11) Furukawa, H.; Go, Y. B.; Ko, N.; Park, Y. K.; Uribe-Romo, F. J.; Kim, J.; O'Keeffe, M.; Yaghi, O. M., *Inorg. Chem.* **2011**, *50*, 9147-9152.
(12) Ma, L.; Falkowski, J. M.; Abney, C.; Lin, W., *Nat. Chem.* **2010**, *2*, 838-846.
(13) Deng, H.; Doonan, C. J.; Furukawa, H.; Ferreira, R. B.; Towne, J.; Knobler, C. B.; Wang, B.; Yaghi, O. M., *Science* **2010**, *327*, 846-850.
(14) Li, M.; Li, D.; O'Keeffe, M.; Yaghi, O. M., *Chem. Rev.* **2014**, *114*, 1343-1370.
(15) Eddaoudi, M.; Li, H.; Yaghi, O. M., *J. Am. Chem. Soc.* **2000**, *122*, 1391-1397.
(16) Li, J.; Sculley, J.; Zhou, H., *Chem. Rev.* **2012**, *112*, 869-932.
(17) Alhamami, M.; Doan, H.; Cheng, C., *Materials* **2014**, *7*, 3198-3250.
(18) Schneemann, A.; Bon, V.; Schwedler, I.; Senkovska, I.; Kaskel, S.; Fischer, R. A., *Chem. Soc. Rev.* **2014**, *43*, 6062-6096.
(19) Thallapally, P. K.; Tian, J.; Radha Kishan, M.; Fernandez, C. A.; Dalgarno, S. J.; McGrail, P. B.; Warren, J. E.; Atwood, J. L., *J. Am. Chem. Soc.* **2008**, *130*, 16842-16843.
(20) Tian, J.; Saraf, L. V.; Schwenzer, B.; Taylor, S. M.; Brechin, E. K.; Liu, J.; Dalgarno, S. J.; Thallapally, P. K., *J. Am. Chem. Soc.* **2012**, *134*, 9581-9584.
(21) Henke, S.; Schmid, R.; Grunwaldt, J.-D.; Fischer, R. A., *Chem. Eur. J.* **2010**, *16*, 14296-14306.
(22) Kong, L.; Zou, R.; Bi, W.; Zhong, R.; Mu, W.; Liu, J.; Han, R. P. S.; Zou, R., *J. Mater. Chem. A* **2014**, *2*, 17771–17778.

(23) Lama, P.; Aggarwal, H.; Bezuidenhout, C. X.; Barbour, L. J., *Angew. Chem. Int. Ed.* **2016**, *55*, 13271-13275.
(24) Bousquet, D.; Coudert, F.; Fossati, A. G. J.; Neimark, A. V.; Fuchs, A. H.; Boutin, A., *J. Chem. Phys.* **2013**, *138*, 174706.
(25) Coudert, F.; Boutin, A.; Fuchs, A. H.; Neimark, A. V., *J. Phys. Chem. Lett.* **2013**, *4*, 3198-3205.
(26) Ortiz, A. U.; Boutin, A.; Fuchs, A. H.; Coudert, F., *J. Chem. Phys.* **2013**, *138*, 174703.
(27) Murdock, C. R.; McNutt, N. W.; Keffer, D. J.; Jenkins, D. M., *J. Am. Chem. Soc.* **2014**, *136*, 671-678.
(28) Uemura, K.; Kitagawa, S.; Kondo, M.; Fukui, K.; Kitaura, R.; Chang, H.-C.; Mizutani, T., *Chem. Eur. J.* **2002**, *8*, 3586-3600.
(29) Kitaura, R.; Seki, K.; Akiyama, G.; Kitagawa, S., *Angew. Chem. Int. Ed.* **2003**, *42*, 428-431.
(30) Uemura, K.; Kitagawa, S.; Fukui, K.; Saito, K., *J. Am. Chem. Soc.* **2004**, *126*, 3817-3828.
(31) Uemura, K.; Matsuda, R.; Kitagawa, S., *J. Solid State Chem.* **2005**, *178*, 2420-2429.
(32) Walton, K. S.; Millward, A. R.; Dubbeldam, D.; Frost, H.; Low, J. J.; Yaghi, O. M.; Snurr, R. Q., *J. Am. Chem. Soc.* **2008**, *130*, 406-407.
(33) Boutin, A.; Coudert, F.-X.; Springuel-Huet, M.-A.; Neimark, A. V.; Férey, G.; Fuchs, A. H., *J. Phys. Chem. C* **2010**, *114*, 22237-22244.
(34) Deria, P.; Gómez-Gualdrón, D. A.; Bury, W.; Schaef, H. T.; Wang, T. C.; Thallapally, P. K.; Sarjeant, A. A.; Snurr, R. Q.; Hupp, J. T.; Farha, O. K., *J. Am. Chem. Soc.* **2015**, *137*, 13183-13190.
(35) Kitagawa, S.; Matsuda, R., *Coord. Chem. Rev.* **2007**, *251*, 2490-2509.
(36) Fletcher, A. J.; Thomas, K. M.; Rosseinsky, M. J., *J. Solid State Chem.* **2005**, *178*, 2491-2510.
(37) Fairen-Jimenez, D.; Moggach, S. A.; Wharmby, M. T.; Wright, P. A.; Parsons, S.; Düren, T., *J. Am. Chem. Soc.* **2011**, *133*, 8900-8902.
(38) Hyun, S.-m.; Lee, J. H.; Jung, G. Y.; Kim, Y. K.; Kim, T. K.; Jeoung, S.; Kwak, S. K.; Moon, D.; Moon, H. R., *Inorg. Chem.* **2016**, *55*, 1920-1925.
(39) Pakhira, S.; Takayanagi, M.; Nagaoka, M., *J. Phys. Chem. C* **2015**, *119*, 28789-28799.
(40) Groom, C. R.; Bruno, I. J.; Lightfoot, M. P.; Ward, S. C., *Acta Crystallogr. Sect. B-Struct. Sci.* **2016**, *72*, 171-179.
(41) Draguta, S.; Fonari, M. S.; Bejagam, S. N.; Storms, K.; Lindline, J.; Timofeeva, T. V., *Struct. Chem.* **2016**, *27*, 1303-1315.
(42) Hsu, Y.-F.; Hu, H.-L.; Wu, C.-J.; Yeh, C.-W.; Proserpio, D. M.; Chen, J.-D., *CrystEngComm* **2009**, *11*, 168-176.
(43) Reinsch, H.; Pillai, R. S.; Siegel, R.; Senker, J.; Lieb, A.; Maurin, G.; Stock, N., *Dalton Trans.* **2016**, *45*, 4179-4186.
(44) Rather, B.; Zaworotko, M. J., *Chem. Commun.* **2003**, 830-831.
(45) Hwang, I. H.; Bae, J. M.; Kim, W.; Jo, Y. D.; Kim, C.; Kim, Y.; Kim, S.; Huh, S., *Dalton Trans.* **2012**, *41*, 12759-12765.
(46) Seco, J. M.; Fairen-Jimenez, D.; Calahorro, A. J.; Mendez-Linan, L.; Perez-Mendoza, M.; Casati, N.; Colacio, E.; Rodriguez-Dieguez, A., *Chem. Commun.* **2013**, *49*, 11329-11331.
(47) Barbour, L. J., *Chem. Commun.* **2006**, 1163-1168.
(48) Chen, B.; Ji, Y.; Xue, M.; Fronczek, F. R.; Hurtado, E. J.; Mondal, J. U.; Liang, C.; Dai, S., *Inorg. Chem.* **2008**, *47*, 5543-5545.
(49) Martin, D. P.; Supkowski, R. M.; LaDuca, R. L., *Cryst. Growth Des.* **2008**, *8*, 3518-3520.
(50) Sposato, L. K.; LaDuca, R. L., *Polyhedron* **2010**, *29*, 2239-2249.
(51) Dey, R.; Haldar, R.; Maji, T. K.; Ghoshal, D., *Cryst. Growth Des.* **2011**, *11*, 3905-3911.
(52) Uebler, J. W.; Pochodylo, A. L.; LaDuca, R. L., *Inorg. Chim. Acta* **2013**, *405*, 31-42.
(53) Bhattacharya, B.; Haldar, R.; Dey, R.; Maji, T. K.; Ghoshal, D., *Dalton Trans.* **2014**, *43*, 2272-2282.
(54) Yang, Z.; Zhao, S.; Han, S.; Zheng, L.; Li, B.-L.; Wu, B., *Inorg. Chem. Commun.* **2014**, *46*, 24-28.
(55) Yang, Z.; Han, S.; Zheng, L.; Peng, Y.; Li, B.; Li, H., *J. Coord. Chem.* **2015**, *68*, 1213-1223.
(56) Bruker *TOPAS*, 4.2; AXS: Karlsruhe, 2009.
(57) Nelson, A. P.; Farha, O. K.; Mulfort, K. L.; Hupp, J. T., *J. Am. Chem. Soc.* **2009**, *131*, 458-460.
(58) Bezuidenhout, C. X.; Smith, V. J.; Bhatt, P. M.; Esterhuysen, C.; Barbour, L. J., *Angew. Chem. Int. Ed.* **2015**, *54*, 2079-2083.
(59) Spek, A., *J. Appl. Crystallogr.* **2003**, *36*, 7-13.
(60) Utrecht, A. L. S. *PLATON*, the Netherlands, 1998.
(61) Herres, J. P.; Moran, C. A.; Forman, M. A.; Hall, J. E.; McCauley, J. P.; Pivonka, D. E.; Wesolowski, S. S., *J. Org. Chem.* **2016**, *81*, 6862-6866.
(62) Marchessault, R. H.; Perez, S., *Biopolymers* **1979**, *18*, 2369-2374.
(63) Mo, Y., *J. Org. Chem.* **2010**, *75*, 2733-2736.
(64) Murcko, M. A.; Castejon, H.; Wiberg, K. B., *J. Phys. Chem.* **1996**, *100*, 16162-16168.

4.2. SUPPORTING INFORMATION

Solvent and Pressure-Induced Phase Changes in Two 3D Copper Glutarate-Based MOFs via Glutarate (+*gauche* ⇋ −*gauche*) Conformational Isomerism.

Charl X. Bezuidenhout, Vincent J. Smith, Catharine Esterhuysen* and Leonard J. Barbour*

Department of Chemistry and Polymer Science, University of Stellenbosch, Matieland, 7602, South Africa

Contents

1. Synthesis and characterization

Materials

All materials were purchased from a commercial source and used without further purification.

Synthesis

$[Cu_2(glu)_2(bpa)]_n \cdot 2.4H_2O$ (**1a**) $Cu(NO_3)_2$ (1 mmol), glutaric acid (1 mmol) and 1,2-bis(4-pyridyl)ethane (bpa, 0.5 mmol) were mixed in 100 ml H_2O. 1 molar eqv. of NaOH was added dropwise with swirling to prevent precipitation. The blue solution was placed in an oven preheated to 80 °C. Green block shaped crystals were obtained after 24 – 48 hours.

$[Cu_2(glu)_2(bpp)]_n \cdot 2$acetone (2a) 50 ml of a H_2O/acetone (1:1) buffer solution was layered on a solution of glutaric acid (1 mmol), 1 eqv NaOH (1M) and 1,3-bis(4-pyridyl)propane (bpp, 0.5 mmol) in 50 ml H_2O/acetone (2:1). A solution of $Cu(NO_3)_2$ (1 mmol) in 50 ml acetone (ace) was then layered on the buffer solution. The vessel was carefully placed and allowed to diffuse in an oven heated to 50-55 °C. Green block and plate like crystals were collected after 48 hours.

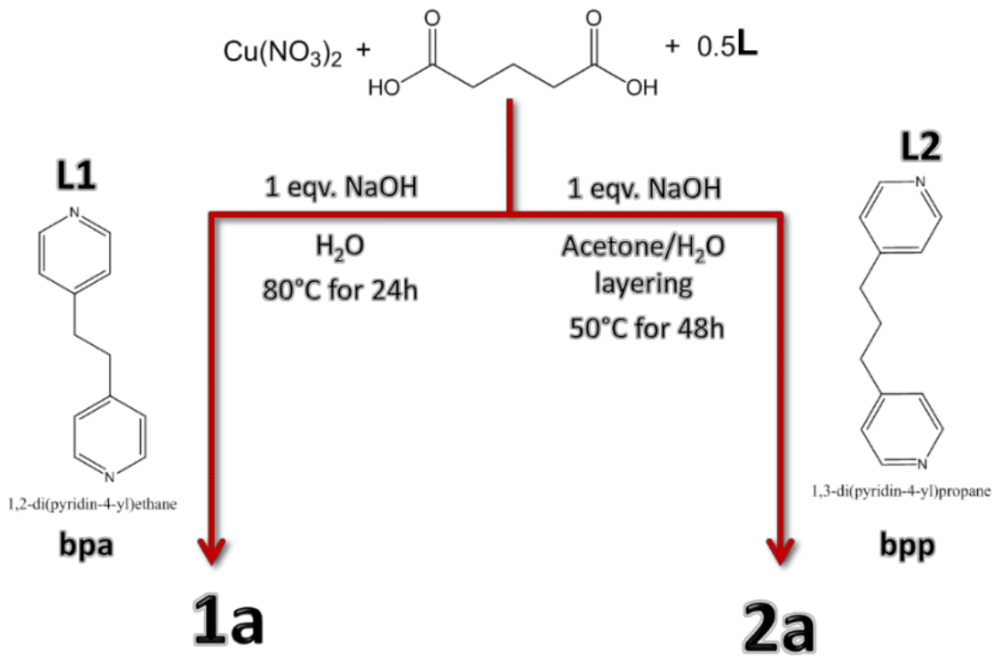

Scheme S1. Synthesis of $[Cu_2(glu)_2(bpa)]_n \cdot 2.4H_2O$ (**1a**) and $[Cu_2(glu)_2(bpp)]_n \cdot 2$ace (**2a**).

2. Methods

Thermogravimetric analysis (TGA)

Thermogravimetric analysis was carried out using a TA Instruments Q500 analyzer. The sample was loaded in an aluminum pan and heated at 10 °C/min from room temperature up 600 °C.

Supercritical CO_2 Experiments

Newly synthesized MOF crystals were exposed to supercritical CO_2 ($scCO_2$) for 24 h to obtain the apohost or activated phase. Supercritical CO_2, having properties of both liquid and gas, exerts little or no surface tension on the walls of the channels in the crystal. Depending on the solvent present in the channels and the exact conditions of temperature and pressure ($31.1 < T_c < 44$ °C; $73 < P_c < 110$ bar) $scCO_2$ is able to dissolve the solvent molecules and leave behind the activated phase. Typically, a vial containing the crystals was placed directly onto dry-ice while being transported for analysis.

Single-crystal X-ray Diffraction

Suitable single crystals were selected and mounted onto a diffractometer using a MiTeGen MicroCrystal mount. Single-crystal X-ray diffraction data were collected using a Bruker SMART diffractometer equipped with an APEX-II CCD area-detector, and an Oxford Cryosystems 700Plus cryostat for temperature control. X-rays were generated from a sealed tube (MoKα radiation λ = 0.71073 Å) fitted with a multilayer monochromator. All data were collected at 100 K.

Data reduction was carried out by means of the standard procedure using the Bruker software package SAINT2 and the absorption corrections and the correction of other systematic errors were performed using SADABS.3. Using X-Seed [S1] and Olex2 [S2], the structure was solved with the SHELXS [S3] structure solution program using Direct Methods and refined with the SHELXL [S4] refinement package using least squares minimization. Hydrogen atoms were placed in calculated positions using riding models.

3. Computational Methods

Density functional theory (DFT)

DFT calculations was carried out using the Guassian09 software package.[S5] This software was used to compute the gauche torsional scan of a single glutaric acid. All optimizations were carried out at mPW1PW91/6-311+G(d,p) (hybrid Hartree–Fock density functional) level of theory. The *SCF=QC* option was used to manage conversion difficulties and consequently a larger DFT integration grid (*Int=UltraFine*) was chosen.

Atomic charges

Only the hydrogen atoms of the frameworks were optimized as part of a periodic system using the CASTEP module of the Materials Studio software suite.[S6] The optimization was performed using the GGA PBE functional with Grimme's DFT-D dispersion correction; thresholds for geometry optimization and SCF convergence were chosen as 1×10^{-6} eV. The Milliken charges were calculated at the end of the optimization process (this is given as an option in the properties tab of the calculation setup). These atomic charges were used in all the molecular mechanics calculations.

Molecular Mechanics (MM)

All MM calculations were performed using the Forcite-Plus module within the Biovia Materials Studio software suite.[S6]

Forcite energy parameters (Materials Studio)

Quality	Ultra-fine
Force field	COMPASS
Charges	Current (obtained from CASTEP)
Summation method	
Electrostatic	Ewald
van der Waals	Ewald
Ewald accuracy	1.0e-5 kcal/mol

Forcite Geometry optimization parameters (Materials Studio)

Geometry optimization	
Algorithm	Smart
Energy tolerance	2.0e-5 kcal/mol
Force	0.001 kcal/mol/Å
Max iterations	800
Keep motion groups rigid	

4. Crystallographic tables and structural analysis

Table S1. Crystallographic table of **1a**, **1´a**, **2a** and **2´b**. PXRD indexed unit cells for **1´** and **2´**.

	1b	**1a**	**1´a**	**1´**	**2a**	**2´b**	**2´**
Experimental Method	SCXRD	SCXRD	SCXRD	PXRD	SCXRD	SCXRD	PXRD
Temperature	100.15	100.15	100.15	RT	100.15	100.15	RT
Crystal system	monoclinic	monoclinic	monoclinic	monoclinic	orthorhombic	orthorhombic	orthorhombic
Space group	C2/c	C2/c	C2/c	*C2/c*	*Pccn*	*Pccn*	*Pccn*
a/Å	24.556(2)	24.4258(11)	23.720(9)	23.970	12.9025(11)	27.255(9)	27.378
b/Å	12.9794(12)	13.1097(6)	11.800(4)	11.888	27.615(2)	11.819(4)	12.065
c/Å	8.6609(8)	8.6242(4)	9.239(4)	9.121	8.5728(7)	9.148(3)	9.151
β/°	91.796(2)	91.627(2)	90.476(4)	91.845			
Volume/Å^3	2759.1(4)	2760.5(2)	2585.7(17)	2597.7	3054.6(4)	2946.6(17)	3022.6
Void volume per cell/Å^3	466.89*	520.43*	281.27 *		645.25*	490.65*	

*The void volumes were calculated using the Materials Studio Visualizer with a probe radius of 1.4 Å.

5. Structural phase classification

We refer to the guest-free (i.e. virtual)[7] framework structures of **1a** and **2a** as **1** and **2**, respectively. These structures are the *wide-channel* (wc) forms. We refer to the guest-free (virtual) framework structures of **1'a** and **2'b** as **1'** and **2'**, respectively. These structures with the "*prime*" notation are the *narrow-channel* (nc) forms.

Table S2. Classification of the different structural phases of **1** and **2**.

	Wide-channel	**Narrow-channel**	**Wide-channel**	**Narrow-channel**
Crystal structures	**1a and 1b**	**1´a**	**2a**	**2´b**
Host framework structures Guest-free (virtual)	**1**	**1´**	**2**	**2´**
Activated forms		**1´**		**2´**

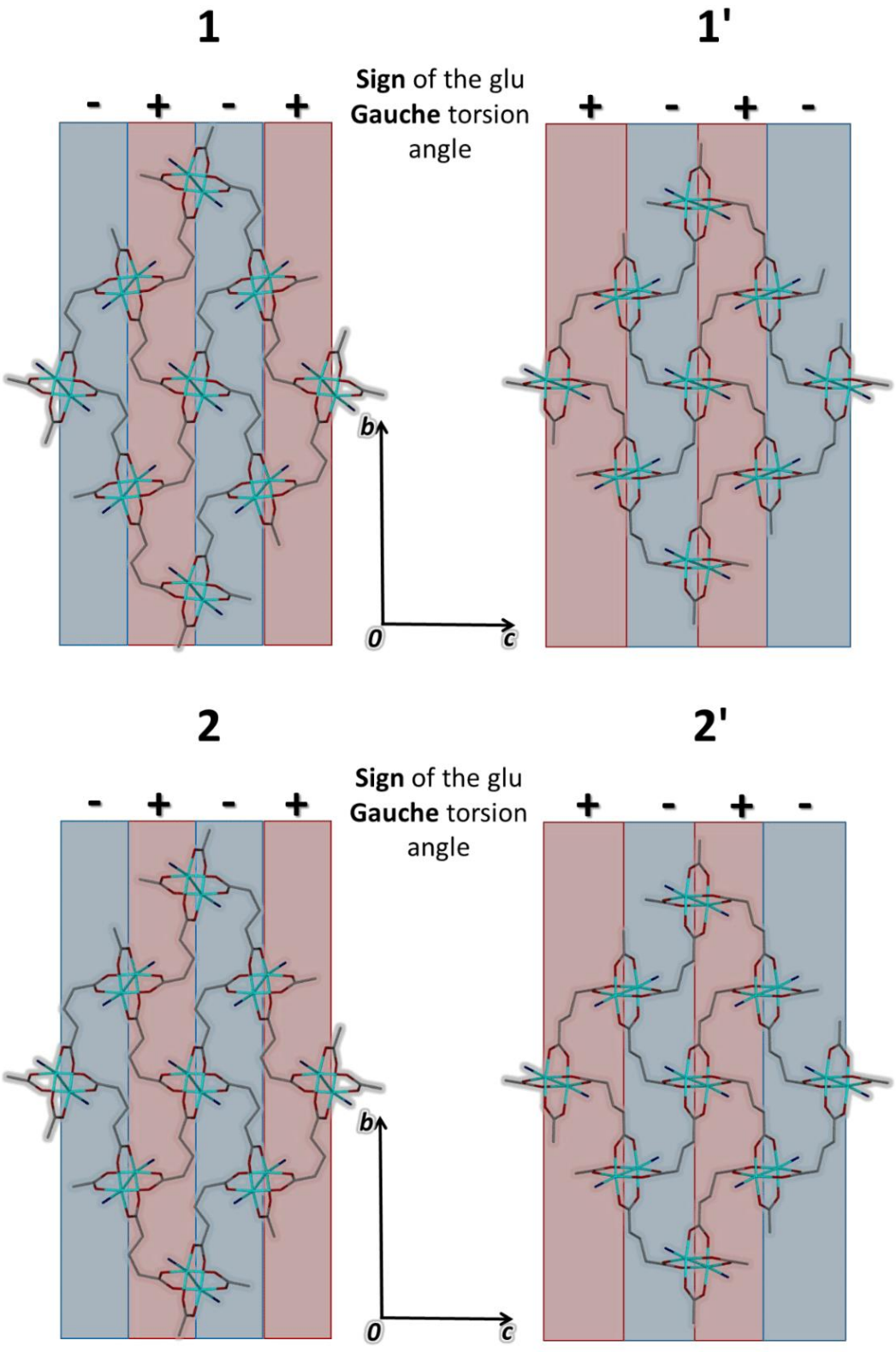

Figure S1. The Cu-glutarate 2-D grids for **1**, **1´**, **2** and **2´** viewed along the crystallographic *c*-axis. The **blue** and **red** bands indicate the sign of the glu gauche torsion angles. Hydrogen atoms have been omitted for clarity.

Table S3 The glutarate *anti* and *gauche* torsion angles (in degrees) of **1**, **1´**, **2** and **2´**. The copper paddle-wheel axial orientations relative the *bc*, *ab* and *ac* planes.

	1	**1´**	**Relative Difference**	**2**	**2´**	**Relative Difference**
Glu **Gauche** torsion angle (°)	±57.5	∓75.7	*133.2*	±59.2	∓77.1	*136.3*
Glu **Anti** torsion angle (°)	∓176.0	±161.9	*22.1*	∓172.0	±162.3	*25.7*
Cu-paddlewheel axial orientation (°)						
Relative to *bc* plane	56.91	53.79	*3.12*	54.79	54.44	0.35
Relative to *ab* plane	23.93	34.10	*10.17*	19.97	32.85	12.88
Relative to *ac* plane	25.67	11.86	*13.81*	27.72	12.11	15.61

The *gauche*- and *anti*-torsion angles exist with both + and - signs within the crystal structures in an ABAB fashion. The positive angle changes to negative while the negative angle changes to positive. Thus we use ± and ∓ to denote the inversion.

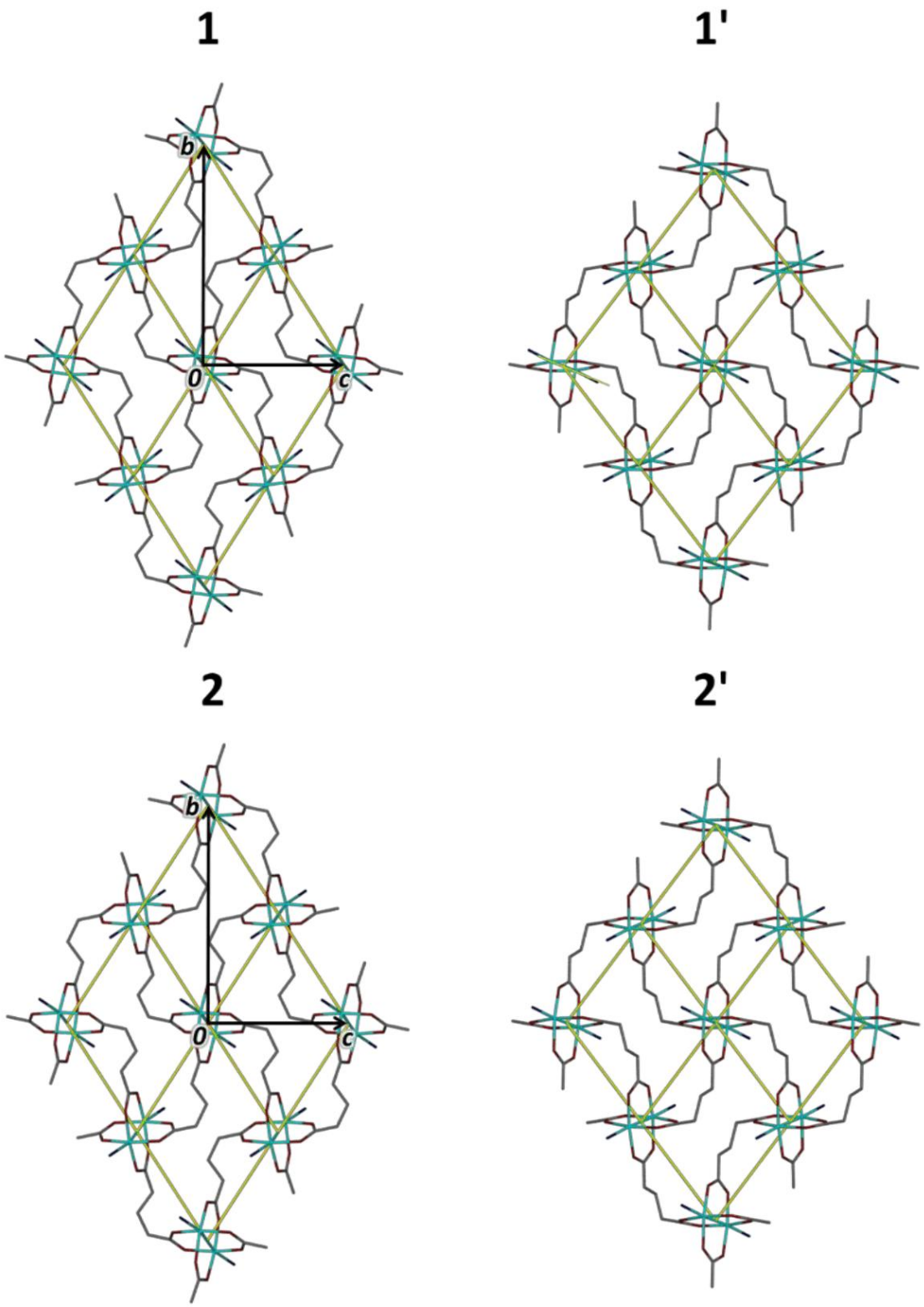

Figure S2. The Cu-glutarate 2-D grids for **1**, **1´**, **2** and **2´** viewed along the crystallographic *c* axis. The yellow lines connect centroids of each paddle-wheel SBU in order to show the grid topology. Hydrogen atoms have been omitted for clarity.

Table S4. The *ab* plane inclination, bend angles and scissor angles formed by both linkers.

	1a (Bpa)	1'a (Bpa)	Relative Difference	2a (Bpp)	2'b (Bpp)	Relative Difference
ab plane inclination (°)	35.73	38.05	2.32			
Scissor angle (°)	58.75	61.85	3.10	47.37	51.48	4.11
Bend angle (°)				94.12	84.03	-10.09

All the angles were measured using the Mercury CSD 5.3.1. software.

6. TGA thermograms

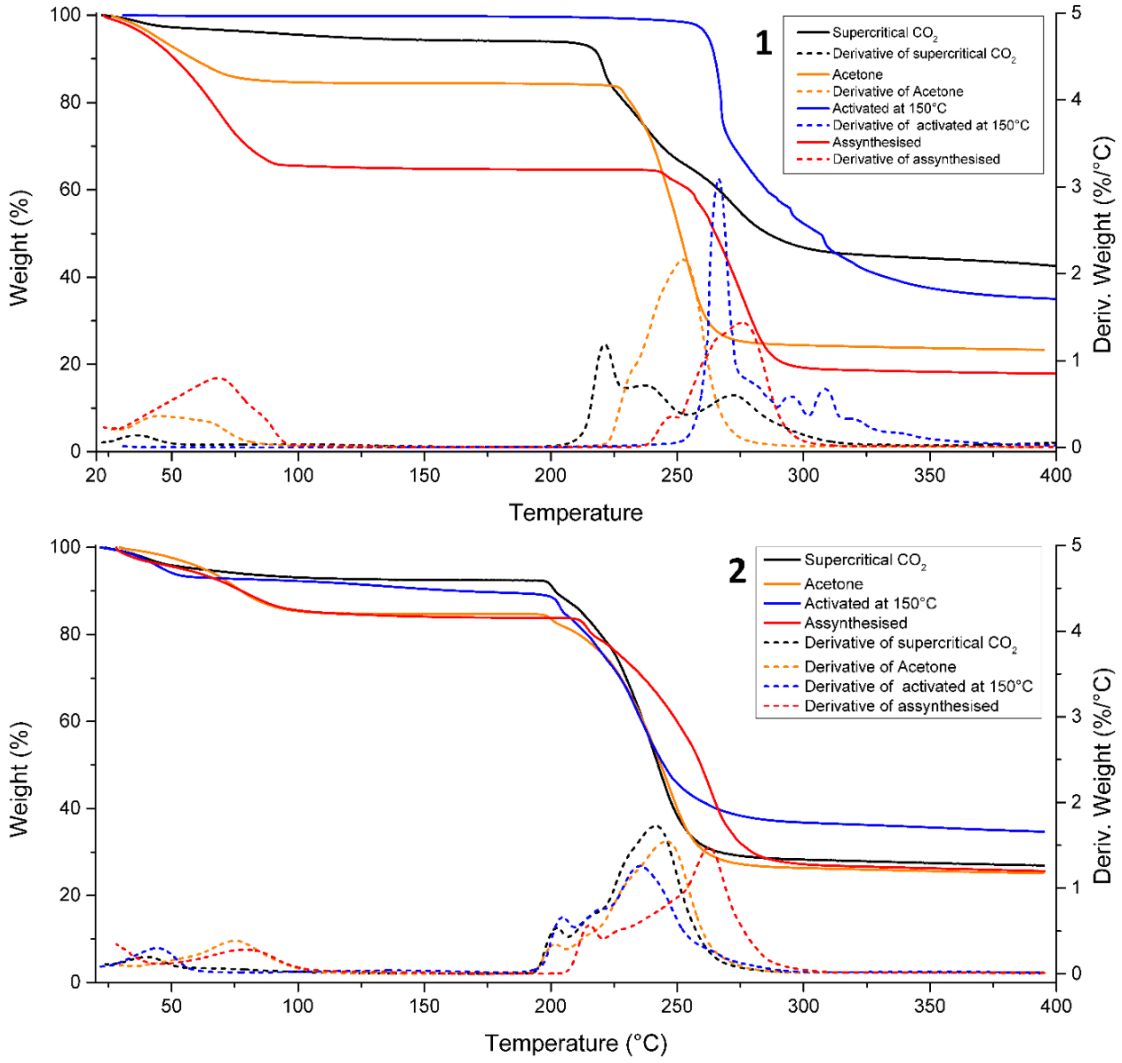

Figure S3. Thermogravimetric analysis of various solvates and the activated materials of **1** and **2**. The weight % and its derivative are shown. The large mass loss for as-synthesised **1** (**1a**) is not reliable owing to the presence surface solvent, which could not be avoided. Our interest lies in the temperature at which the guest/solvent evolution is complete.

7. Powder X-ray diffraction

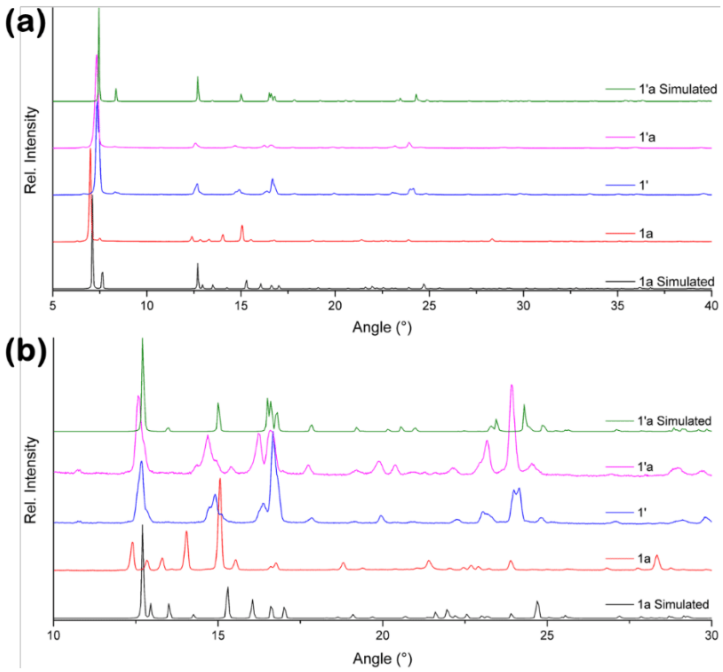

Figure S4. PXRD traces for MOF **1**. (a) Full scale PXRD trace. (b) Zoomed in at 10° to 30° for better comparison of the PXRD traces. Crystal structures determined at 100 K were used to generate the simulated PXRD traces.

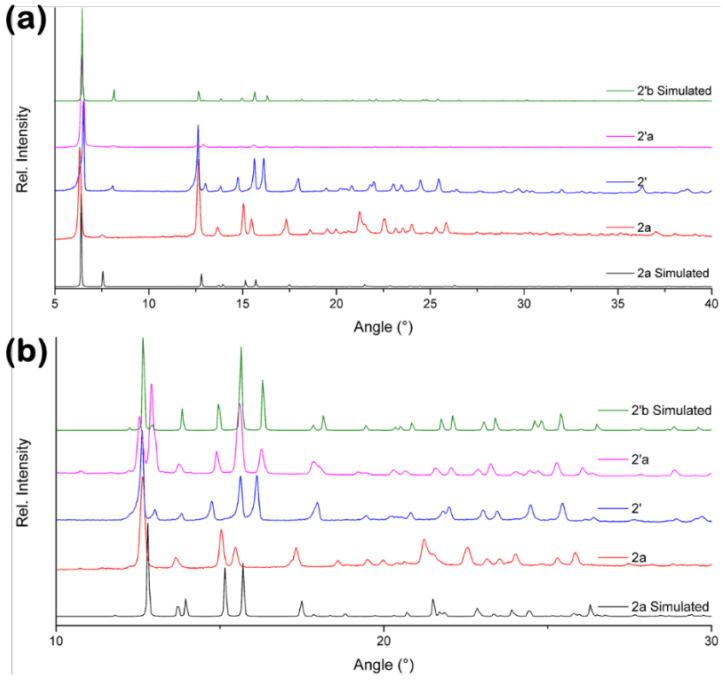

Figure S5. PXRD traces for MOF **2**. (a) Full scale PXRD trace. (b) Zoomed in at 10° to 30° for better comparison of the PXRD traces. Crystal structures determined at 100 K were used to generate the simulated PXRD traces.

Table S5. Crystallographic tables for **1a** and **1´a**. PXRD indexed unit cells for **1a**, **1´** and **1´a**.

	1a	**1a**	**1´**	**1´a**	**1´a**
Experimental Method	SCD	PXRD	PXRD	PXRD	SCD
Temperature	100.15	RT	RT	RT	100.15
Crystal system	monoclinic	monoclinic	monoclinic	monoclinic	monoclinic
Space group	*C2/c*	*C2/c*	*C2/c*	*C2*	*C2/c*
a/Å	24.4258(11)	25.318	23.970	23.989	23.720(9)
b/Å	13.1097(6)	13.284	11.888	11.922	11.800(4)
c/Å	8.6242(4)	8.731	9.121	9.203	9.239(4)
β/°	91.627(2)	94.62	91.84	91.81	90.476(4)
Volume/Å^3	2760.5(2)	2926.9	2597.7	2630.5	2585.7(17)

Table S6. Crystallographic tables for **2a** and **2´b**. PXRD indexed unit cells for **2a**, **2´** and **2´a**.

	2a	**2a**	**2´**	**2´a**	**2´b**
Experimental Method	SCD	PXRD	PXRD	PXRD	SCD
Temperature	100.15	RT	RT	RT	100.15
Crystal system	orthorhombic	orthorhombic	orthorhombic	orthorhombic	orthorhombic
Space group	*Pccn*	*Pccn*	*Pccn*	*Pccn*	*Pccn*
a/Å	12.9025(11)	28.220	27.3778	27.270	27.255(9)
b/Å	27.615(2)	13.012	12.065	11.836	11.819(4)
c/Å	8.5728(7)	8.725	9.151	9.200	9.148(3)
Volume/Å^3	3054.6(4)	3203.6	3022.6	2969.4	2946.6(17)

8. FTIR

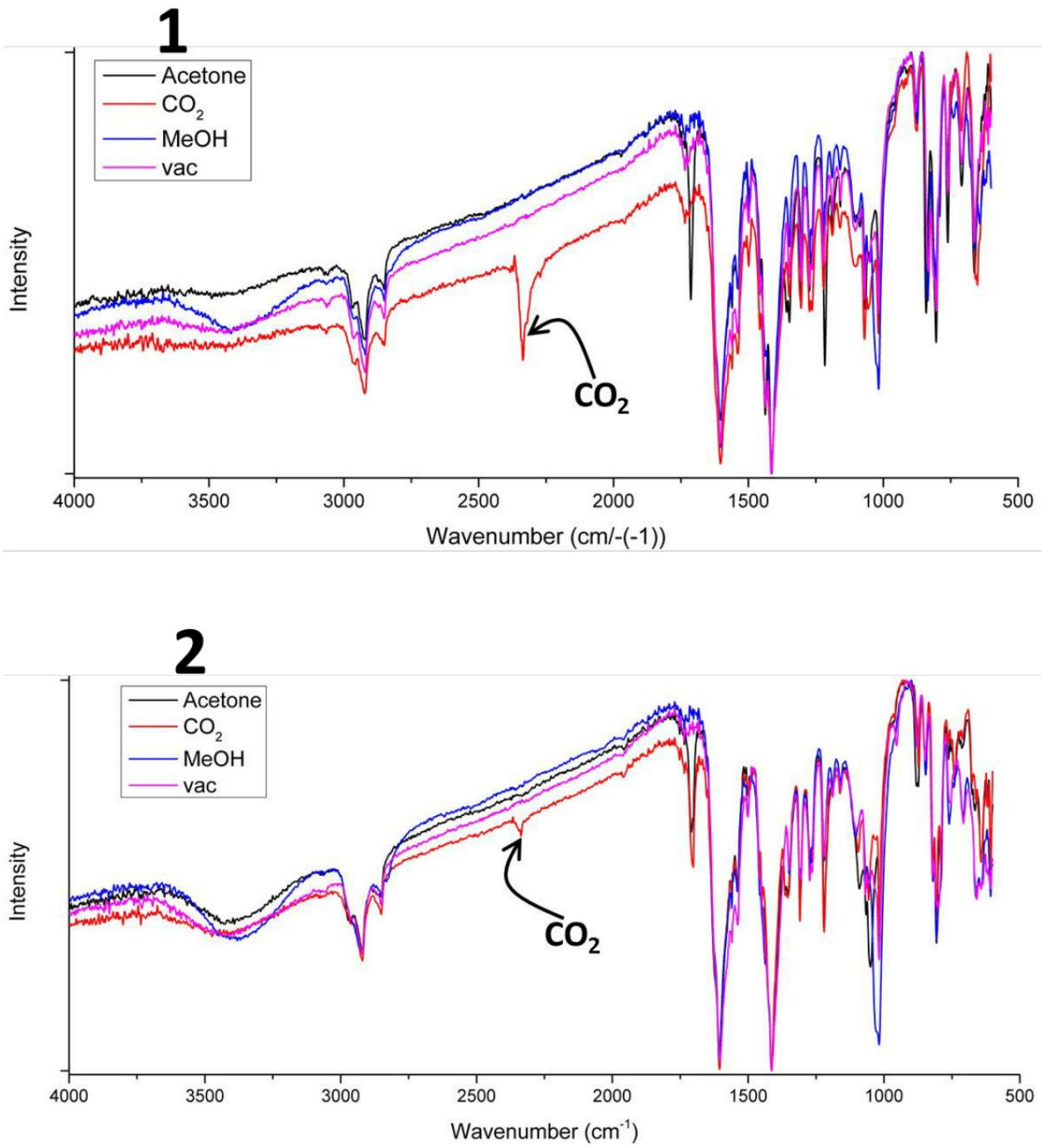

Figure S6. FTIR spectra, recorded at RT, of **1** and **2** with different guests. The band associated with the CO_2 anti-symmetric stretch is indicated.

9. Pressure-ramped differential scanning calorimetry (P-DSC)

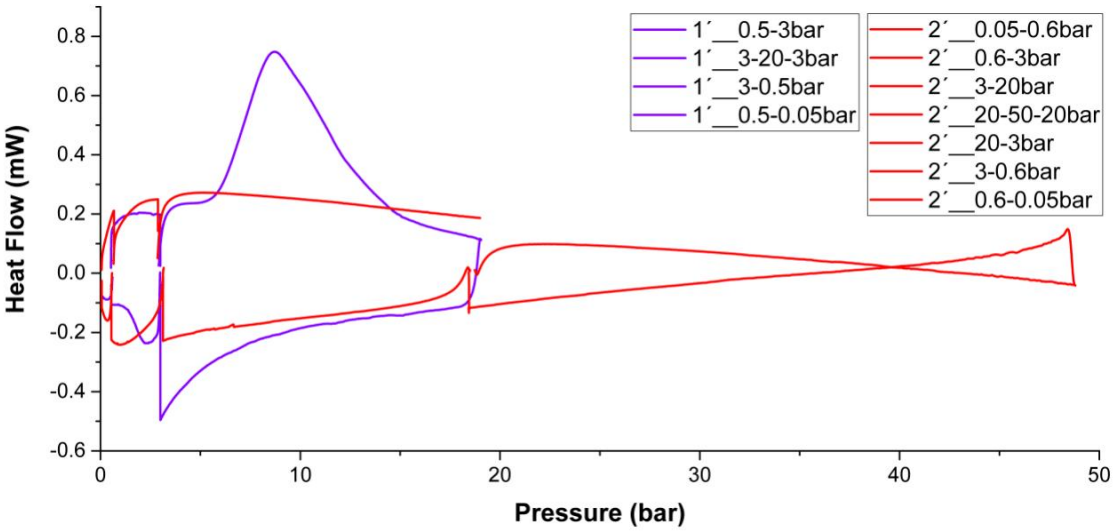

Figure S7. P-DSC scans for **1**' and **2**' with CO_2 at 25 °C.

10. CO_2—CO_2 interactions in MOF 2.

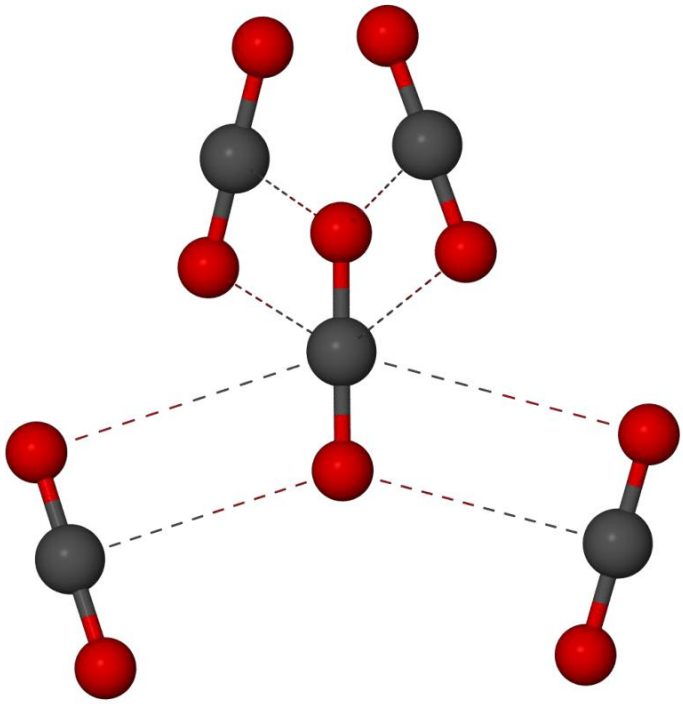

Figure S8. The arrangement of CO_2 molecules in the crystal structure of **2**'**b**. The central molecule forms slipped-parallel electrostatic interaction with the surrounding CO_2 molecules.

11. Computational models and data

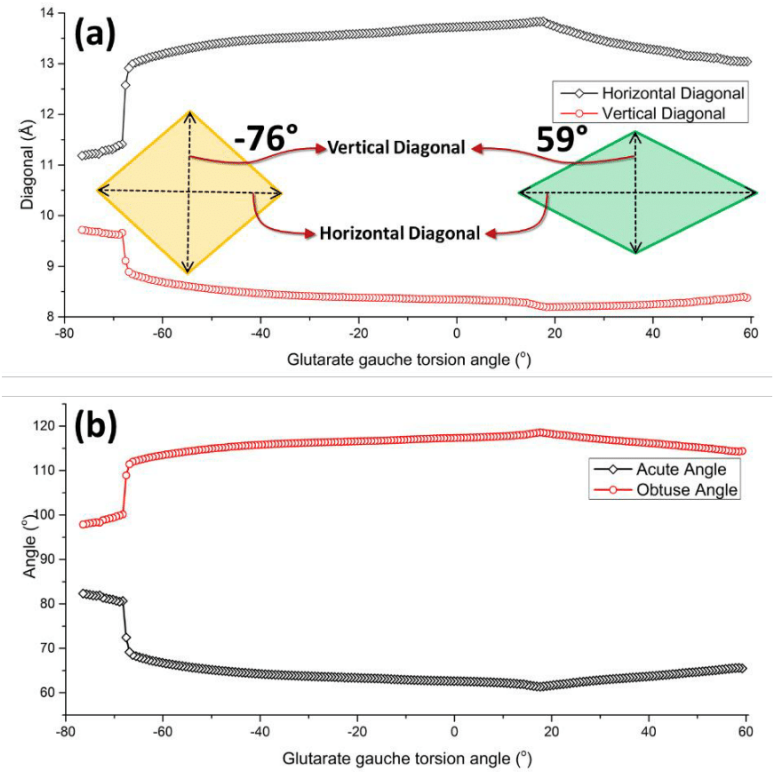

Figure S9. Data obtained from the four paddle-wheel computational simulation. A parallelogram is drawn by connecting centroids generated for each paddlewheel unit. (a) The horizontal (acute) and vertical (obtuse) diagonals of the parallelogram. (b) The acute and obtuse angles of the parallelogram.

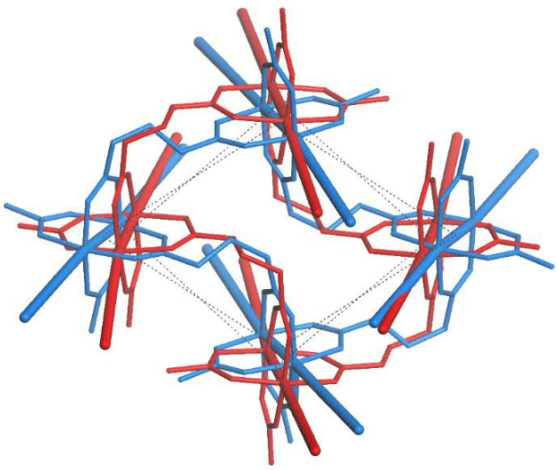

Figure S10. Overlay of the initial (red, wc) and final (blue, nc) structures of the glutarate ±g↔∓g torsional potential energy scan.

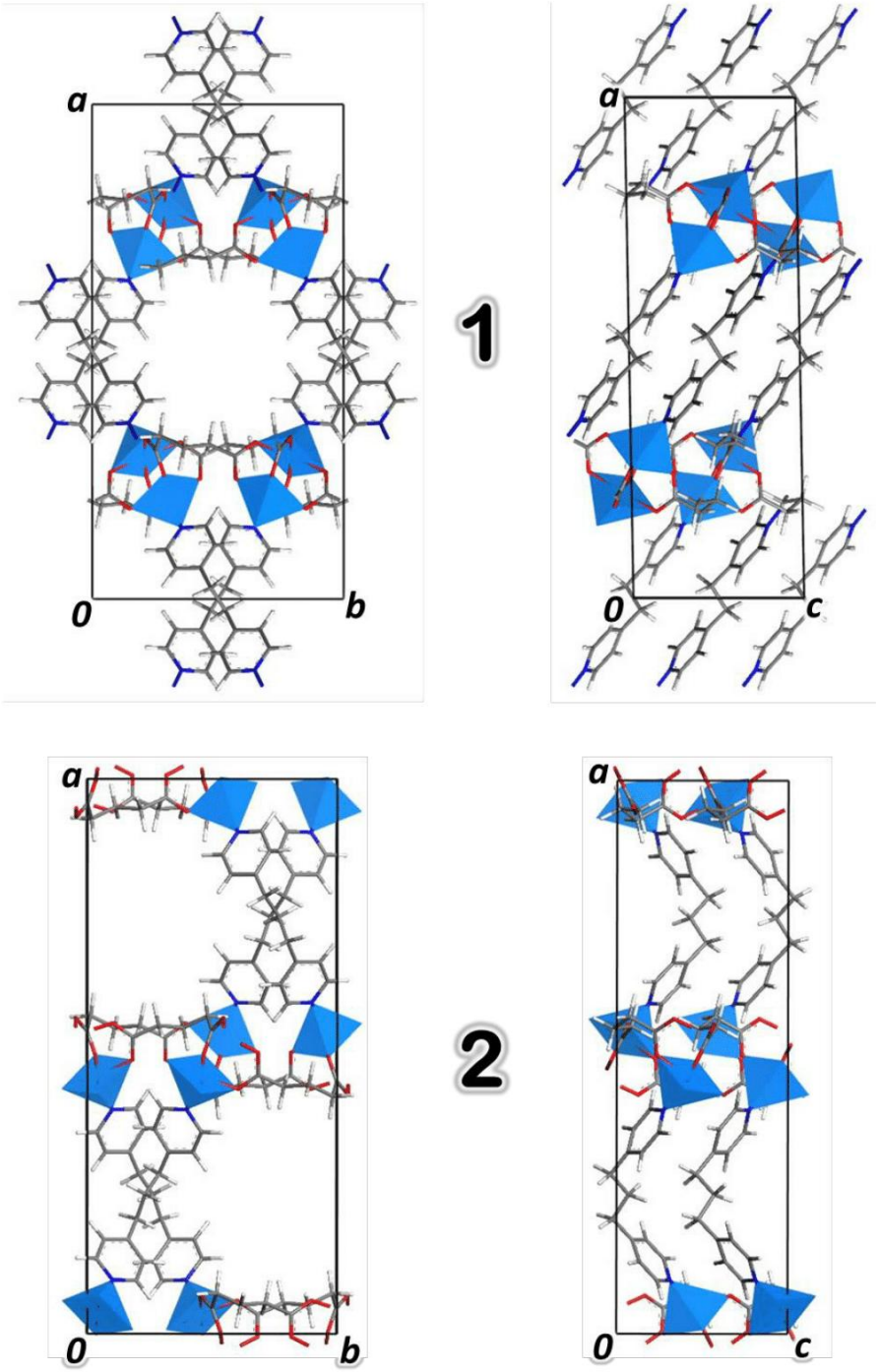

Figure S11. Full unit cell computational models for **1** and **2** used in the molecular mechanics simulations for the potential energy scans.

Table S7. The energy barriers (kcal/mol) for all the computational models and potential energy scan.

Free Glu model		4 Paddle-wheel model			Full unit cell model - MOF 1	Full unit cell model - MOF 2
ΔE(C-B)	4.4	ΔE(A-B)	4.76	ΔE(B1-A1)	2.99	4.32
ΔE(A-B)	3.03	ΔE(C-B)	2.9	ΔE(B1-C1)	4.57	5.61
ΔE(C-D)	5.41	ΔE(E-B)	3.89	ΔE(B1-E1)	4.99	6.47
ΔE(E-D)	3.85	ΔE(D-C)	0.22	ΔE(D1-C1)	0.76	0.36
ΔE(B-D)	1.01	ΔE(D-E)	1.22	ΔE(D1-E1)	1.18	1.23
				ΔE(A-B2)	14.77	14.9
				ΔE(B2-C2)	16.77	17.04

12. Full crystallographic table

Table S8. Crystal data and structure refinement.

	1b	1a	1'a	2a	2'b
Empirical formula	$C_{11.5}H_{12}CuNO_{5.44}$	C11H12CuNO4	$C_{11}H_{12}Cu_4N_1O_4$	$C_{14.5}H_{19}NO_5Cu$	$C_{12.31}H_{13}NO_{5.62}Cu$
Formula weight	314.80	285.76	285.76	350.85	328.31
Temperature/K	100.15	100.15	100.15	100.15	100.15
Crystal system	monoclinic	monoclinic	monoclinic	orthorhombic	orthorhombic
Space group	*C2/c*	*C2/c*	*C2/c*	*Pccn*	*Pccn*
a/Å	24.556(2)	24.4258(11)	23.720(9)	12.9025(11)	27.255(9)
b/Å	12.9794(12)	13.1097(6)	11.800(4)	27.615(2)	11.819(4)
c/Å	8.6609(8)	8.6242(4)	9.239(4)	8.5728(7)	9.148(3)
α/°	90	90	90	90.00	90.00
β/°	91.796(2)	91.627(2)	90.476(4)	90.00	90.00
γ/°	90	90	90	90.00	90.00
Volume/Å^3	2759.1(4)	2760.5(2)	2585.7(17)	3054.6(4)	2946.6(17)
Z	8	4	2	8	8
ρ_{calc}g/cm^3	1.516	1.375	1.468	1.526	1.480
μ/mm^{-1}	1.599	1.583	1.690	1.451	1.502
F(000)	1284.0	1168.0	1168.0	1456.0	1342.0
Crystal size/mm^3	0.625 × 0.177 × 0.088	0.542 × 0.081 × 0.056	0.173 × 0.096 × 0.067	0.652 × 0.228 × 0.098	0.21 × 0.155 × 0.05
Radiation	MoKα (λ = 0.71073)	MoKα (λ = 0.71073)	MoKα (λ = 0.71073)	MoKα (λ = 0.71073)	MoKα (λ = 0.71073)
2Θ range for data collection/°	3.318 to 56.586	3.336 to 49.426	3.434 to 53.978	2.94 to 56.88	2.98 to 55.12
Index ranges	-32 ≤ h ≤ 32, -17 ≤ k ≤ 17, -11 ≤ l ≤ 11	-28 ≤ h ≤ 28, -13 ≤ k ≤ 15, -10 ≤ l ≤ 7	-30 ≤ h ≤ 22, -15 ≤ k ≤ 13, -11 ≤ l ≤ 11	-12 ≤ h ≤ 17, -36 ≤ k ≤ 36, -11 ≤ l ≤ 11	-35 ≤ h ≤ 34, -15 ≤ k ≤ 13, -11 ≤ l ≤ 7
Reflections collected	24894	10270	7007	18023	16238
Independent reflections	3422 [R_{int} = 0.0392, R_{sigma} = 0.0236]	2341 [Rint = 0.0366, Rsigma = 0.0275]	2793 [R_{int} = 0.0726, R_{sigma} = 0.0977]	3676 [R_{int} = 0.0209, R_{sigma} = 0.0172]	3372 [R_{int} = 0.0556, R_{sigma} = 0.0448]
Data/restraints/parameters	3422/0/187	2341/0/152	2793/0/154	3676/0/197	3372/0/200
Goodness-of-fit on F^2	1.118	1.075	0.949	1.050	1.044
Final R indexes [I>=2σ (I)]	R_1 = 0.0371, wR_2 = 0.1078	R1 = 0.0265, wR2 = 0.0669	R_1 = 0.0482, wR_2 = 0.0808	R_1 = 0.0228, wR_2 = 0.0570	R_1 = 0.0385, wR_2 = 0.0895
Final R indexes [all data]	R_1 = 0.0437, wR_2 = 0.1114	R1 = 0.0280, wR2 = 0.0678	R_1 = 0.0875, wR_2 = 0.0910	R_1 = 0.0254, wR_2 = 0.0583	R_1 = 0.0609, wR_2 = 0.0995
Largest diff. peak/hole / e Å^{-3}	0.99/-0.37	0.51/-0.34	0.50/-0.64	0.38/-0.46	0.48/-0.45

13. Absolute energies for single H_2glu torsional scan.

C1-C2-C3-C4 dihedral angle (°)	E (Hartree)	Relative E (kcal mol^{-1})	C1-C2-C3-C4 dihedral angle (°)	E (Hartree)	Relative E (kcal mol^{-1})
-120	-496.30894	2.440	5	-496.30444	5.263
-115	-496.30904	2.377	10	-496.30486	4.999
-110	-496.30929	2.220	15	-496.30545	4.629
-105	-496.30966	1.988	20	-496.30617	4.177
-100	-496.31013	1.694	25	-496.30698	3.669
-95	-496.31067	1.355	30	-496.30783	3.136
-90	-496.31125	0.991	35	-496.30867	2.609
-85	-496.31181	0.640	40	-496.30945	2.120
-80	-496.3123	0.332	45	-496.31013	1.694
-75	-496.31266	0.107	50	-496.31067	1.355
-70	-496.31283	0.000	55	-496.31104	1.123
-65	-496.31279	0.025	60	-496.31123	1.004
-60	-496.31253	0.188	65	-496.31122	1.010
-55	-496.31204	0.496	70	-496.31104	1.123
-50	-496.31137	0.916	75	-496.31069	1.342
-45	-496.31053	1.443	80	-496.31021	1.643
-40	-496.30959	2.032	85	-496.30963	2.007
-35	-496.30859	2.660	90	-496.30899	2.409
-30	-496.30758	3.293	95	-496.30834	2.816
-25	-496.30661	3.901	100	-496.30773	3.199
-20	-496.30574	4.447	105	-496.30719	3.538
-15	-496.30502	4.899	110	-496.30677	3.801
-10	-496.3045	5.225	115	-496.30649	3.977
-5	-496.30422	5.401	120	-496.3064	4.033
0	-496.30422	5.401			

14. References

1. (a) Atwood, J. L.; Barbour, L. J., *Cryst. Growth Des.* **2003**, *3*, 3-8; (b) Barbour, L. J., *J. Supramol. Chem.*, **2001**, *1*, 189-191.
2. Dolomanov, O.V., Bourhis, L.J., Gildea, R.J, Howard, J.A.K. & Puschmann, H., *J. Appl. Cryst.* **2009**, *42*, 339-341.
3. Sheldrick, G.M., *Acta Cryst.* **2008**, *A64*, 112-122.
4. Sheldrick, G.M., *Acta Cryst.* **2015**, *C71*, 3-8.
5. Frisch, M. J.; Trucks, G. W.; Schlegel, H. B.; Scuseria, G. E.; Robb, M. A.; Cheeseman, J. R.; Scalmani, G.; Barone, V.; Mennucci, B.; Petersson, G. A.; Nakatsuji, H.; Caricato, M.; Li, X.; Hratchian, H. P.; Izmaylov, A. F.; Bloino, J.; Zheng, G.; Sonnenberg, J. L.; Hada, M.; Ehara, M.; Toyota, K.; Fukuda, R.; Hasegawa, J.; Ishida, M.; Nakajima, T.; Honda, Y.; Kitao, O.; Nakai, H.; Vreven, T.; Montgomery Jr., J. A.; Peralta, J. E.; Ogliaro, F.; Bearpark, M. J.; Heyd, J.; Brothers, E. N.; Kudin, K. N.; Staroverov, V. N.; Kobayashi, R.; Normand, J.; Raghavachari, K.; Rendell, A. P.; Burant, J. C.; Iyengar, S. S.; Tomasi, J.; Cossi, M.; Rega, N.; Millam, N. J.; Klene, M.; Knox, J. E.; Cross, J. B.; Bakken, V.; Adamo, C.; Jaramillo, J.; Gomperts, R.; Stratmann, R. E.; Yazyev, O.; Austin, A. J.; Cammi, R.; Pomelli, C.; Ochterski, J. W.; Martin, R. L.; Morokuma, K.; Zakrzewski, V. G.; Voth, G. A.; Salvador, P.; Dannenberg, J. J.; Dapprich, S.; Daniels, A. D.; Farkas, Ö.; Foresman, J. B.; Ortiz, J. V.; Cioslowski, J.; Fox, D. J., Gaussian 09, Gaussian, Inc.: Wallingford, CT, USA, **2009**.
6. Materials Studio Modeling Environment v8.0.0; Accelrys Software Inc.: San Diego, **2015**.
7. Barbour, L. J., *Chem. Commun.* **2006**, 1163-1168.

Chapter 5

SOLVATOCHROMISM AS A PROBE TO OBSERVE THE SOLVENT EXCHANGE PROCESS IN A 1-D POROUS COORDINATION POLYMER WITH 1-D SOLVENT ACCESSIBLE CHANNELS.

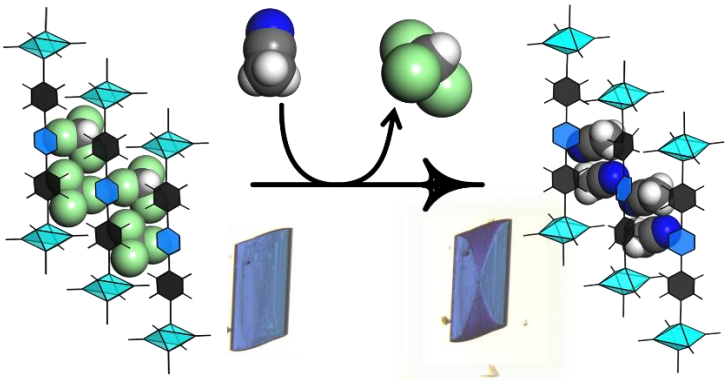

5.1. COMMUNICATION IN CHEMICAL COMMUNICATIONS

Contributions of the author:

- Design of project
- Synthesis of Ligand and PCP
- Collection of single-crystal X-ray data solution and refinement of single-crystal X-ray structures
- TGA thermograms
- Optical microscopy experiments
- Computational modelling
- Interpretation of results
- Writing the first draft of the article

Journal Name

COMMUNICATION

Solvatochromism as a probe to observe the solvent exchange process in a 1-D porous coordination polymer with 1-D solvent accessible channels.

Received 00th January 20xx,
Accepted 00th January 20xx

DOI: 10.1039/x0xx00000x

www.rsc.org/

Charl X. Bezuidenhout, Catharine Esterhuysen* and Leonard J. Barbour*

A one-dimensional porous coordination polymer (PCP) {[Cu_2(acetate)$_2$(3,6-di(pyridin-4-yl)-1,2,4,5-tetrazine)]•2$CHCl_3$}$_n$ possesses pleochroic properties. Solvent exchange with acetonitrile and nitromethane reveals that single crystals of the PCP are also solvatochromic, with the solvent exchange process occurring in an unexpected double V-shaped pattern. Crystal surface adsorption modeling shows that the origin of this effect is preferential sorption at two faces of the crystal.

The development of new porous coordination polymers (PCPs) is a rapidly growing area, primarily owing to the remarkable diversity of potential building blocks and preparative procedures.[1] PCPs comprise 1D, 2D and 3D porous polymeric networks and frameworks consisting of metal ions/clusters tethered by organic linkers.[1e,1f,2] The potential to incorporate the functionalities and properties of the separate components into a functional material provides a very attractive platform for studying gas and small molecule storage, separation or sensing.[1b-e,3] Systematic modification of the individual components (metal ion, organic linker, solvent, etc.) or synthetic conditions allows for tuning of these properties.[1a,1e,4]

Chromophoric organic linkers are often used to obtain PCPs that exhibit solvatochromism or other optical properties.[4c,5] It is well known that most chromophores exhibit colour changes when dissolved in different polar solvents.[6] Hence, building this property into a PCP can turn the material into a functional sensor for small-molecules.[5] Optical properties can also arise from the presence of metal clusters that may become distorted through guest-induced structural changes, or from the interaction of guest molecules with the organic ligands, in turn affecting the electronic structure of the metal.[4c]

Department of Chemistry and Polymer Science, University of Stellenbosch, Matieland, 7602, South Africa, E-mail: ljb@sun.ac.za

† Electronic Supplementary Information (ESI) available: Crystallographic Information Files CCDC 1541488-1541490, synthesis, experimental methods, TGA, Optical microscopy images and computational details. See DOI: 10.1039/x0xx00000x

Tetrazine-based chromophores have recently been used for the synthesis of PCPs;[5b,7] their optical properties are derived from the transitions between the HOMO and LUMO centered on the tetrazine ring. If the linker is conjugated then interactions with the tetrazine rings could influence the optical properties of the metal centres to which they are coordinated.[5b,7a,8] In order to utilise the solvatochromism of a PCP for sensing small molecules, shifts in the λ_{max} values in the solid-state UV-vis spectra of different solvates of the PCP would potentially differentiate between the solvents (small molecules). Generally a λ_{max} shift of 10 nm or more is considered suitable.[9]

A visible colour change of solvatochromic crystals can facilitate the observation of the solvent exchange process (the colours and contrast of the observed crystals can be enhanced by using a polariser). Polarised-light optical microscopy of thin rock slices, i.e. optical mineralogy within petrology, is commonly employed by geologists to study the growth morphology and features of rocks.[10] Time-lapse polarised-light optical microscopy experiments, using single crystals of a solvatochromic material, can visually reveal how a newly introduced solvent permeates the crystals, in addition to showing the preferred crystal face (facet) of entry.[11] The study of crystal features such as morphology, structure, surface electrostatic potential, and dimensionality of porosity (1D, 2D or 3D) can provide insight into the solvent exchange process.

Here we report a 1D Cu(II)(acetate)$_2$ paddlewheel based PCP which undergoes twisting of the organic linkers upon exchange of solvent. The organic chromophoric ligand 3,6-di(pyridin-4-yl)-1,2,4,5-tetrazine (dptz) was used to link the Cu(II)(acetate)$_2$ paddlewheel units into a 1D chain. The solvatochromic and pleochroic properties of this material enable the observation of the solvent exchange process and elucidation of a possible mechanism for the observed solvent-exchange pattern.

Layering Cu(acetate)$_2$ in methanol and dptz in chloroform, with a 1:1 methanol:chloroform buffer, at 50°C afforded dark purple crystals of {[Cu_2(acetate)$_2$(dptz)]•2$CHCl_3$}$_n$ (**1a**). Single-crystal X-ray diffraction (SCD) shows that the PCP crystallises in

the space group $P\bar{1}$. The Cu(acetate)$_2$ paddlewheel secondary building units are linked by dptz to form a 1D coordination polymer (Fig. 1, top). These 1D chains form weak C–H···N contacts between the tetrazine nitrogen atoms of dptz and the pyridyl C–H moieties of each neighbouring dptz linker to form 2D sheets similar to those observed by Lu *et al.*[7a] (Fig. 1, bottom left). These 2D sheets stack together to form 1D open channels with chloroform as included solvent (Fig. 1, top left).

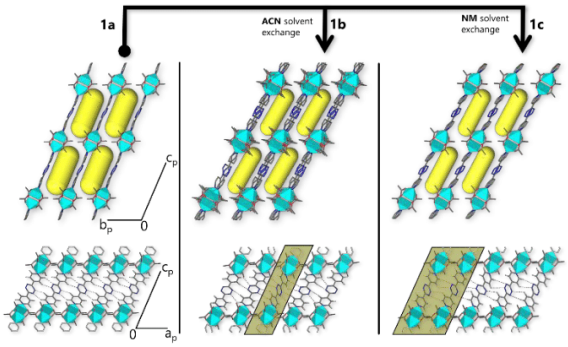

Fig. 1 Top: perspective views along the channels of 1a, 1b and 1c running parallel to [100]. The guest-accessible space is represented by the yellow "capsules" and hydrogen atoms have been omitted for clarity. Bottom: A projection along [010] with the yellow parallelograms indicating the dptz linkers rotated out of the hydrogen-bonded (101) plane. The copper acetate paddlewheel motifs are shown as coordination polyhedra.

Thermogravimetric analysis of **1a** showed complete solvent loss by 120 °C (Fig. S1). The apohost crystal structure could not be obtained owing to insufficient quality of desolvated single crystals. On the other hand, solvent exchange with pure acetonitrile (ACN) and nitromethane (NM) yielded solvates **1b** (ACN) and **1c** (NM) as intact single crystals (Fig. 1, top). SCD analysis reveals that **1b** and **1c** also pack in space group $P\bar{1}$ with host structures similar to that of **1a**. However, the exchanged guest molecules induce distinctive changes in the dptz linker orientations with respect to the channel walls parallel to (101). In **1a** all of the dptz linkers are only slightly tilted towards the channel. In the case of **1b** one in three linkers is tilted significantly further in towards the channel while for **1c** two out of three linkers are tilted towards the channel (Fig. 1, bottom). The solvent accessible volumes decrease from **1a** to **1c**, with increasing number of tilted dptz linkers as opposed to the size of the included guest (*i.e.* the trend is not due to host-guest fit, Table 1). Tilting of the dptz linkers consequently reduces the D—H···A interactions between the adjacent dptz linkers (Fig. S2, Table S1). The D—A distances increase and the D—H···A angles decrease from **1a** - **1c**, resulting in weakening of these interactions (Table S1).

Table 1. Framework and guest molecular volumes.

	1a	**1b**	**1c**
guest	CF	ACN	NM
Guest-accessible space	246 Å^3	181 Å^3	177 Å^3
Guest volume	73.5 Å^3	46.4 Å^3	53.9 Å^3

All volumes were determined with a probe radius of 1.5 Å using the Materials Studio software suite.

In **1a** the chloroform (CF) guest molecules interact with the π-system of the tetrazine moiety through all three chlorine atoms. The partially positive hydrogen atom of CF is directed towards the pyridyl nitrogen atom of a second dptz linker across the channel (Fig. S3). In the cases of **1b** and **1c**, the ACN and NM guest molecules form dimers (through anti-parallel dipole-dipole interactions) and then interact with neighbouring dimers via head-to-tail dipole-dipole interactions along the channel axis (Fig. S4). The ACN and NM molecules interact with both the tetrazine and pyridyl moieties of dptz in a side-on fashion. ACN adopts a head-on alignment to the tetrazine moieties in every third dptz linker (Fig. S5). This interaction could be the reason for the dptz linker rotating out of the plane of each 2D layer of **1b**. Furthermore, ACN forms weak C–H···N interactions with the pyridyl and acetate moieties, whereas the nitro groups of the NM molecules in **1c** form weak C–H···O interactions with the acetate moieties (Fig. S6). **1a** is the only solvate that remains stable when removed from the mother liquor, while **1b** and **1c** desolvate rapidly upon drying, losing their single-crystal nature.

The crystals of **1a** grow as rectangular slabs, with only one set of large crystal faces, (01-1) and (0-11). One of these faces was observed using an optical microscope with a polariser (but not an analyser) to enhance the observation of pleochroism. Upon rotating the stage the crystal appears blue when the long side of the crystal (Fig. S7) is perpendicular to the direction of polarisation and yellow when aligned with it. Additional colours are observed when different crystal faces are viewed, *i.e.* depending on the orientation of the crystal (see Fig. S8). Videos illustrating the pleochroism of **1a** upon rotation of the crystals are available in the ESI (**1b** and **1c** desolvate rapidly in air, thus only **1a** could be studied).

Solid-state UV-Vis analysis of the three solvates reveals two dominant reflectance peaks at ca 450 (blue) and 600 nm (yellow) [Fig. S9]; these colours correspond to those observed by optical microscopy (Fig. S7). The blue peak can be ascribed to the presence of Cu(II) ions in the PCP. Uncoordinated dptz is red, owing to the transition between the HOMO and LUMO orbitals situated on the tetrazine ring.[12] Therefore, coordination of the linker to the metal, along with the D—H···A interaction between dptz linkers and the host-guest interactions could combine to yield the yellow colour. The difference in colour from **1a** to **1c** is due to blue-shifting of the peaks in the spectra**.** The colour change was initially thought to be due to tilting of the pyridyl and tetrazine rings, but the measured tilt angles (Fig. S10) do not correlate with the blue-shift trend. However, the simulated UV-Vis spectra of the dptz linkers show that the systematic weakening of the C-H···N interactions from **1a** to **1c** results in changes in the energies of the LUMO, HOMO and HOMO-1 molecular orbitals, leading to a lowering of the HOMO-1→LUMO transition and a consequent blue-shift in the UV-vis spectra (Fig. S11). Additionally, the simulated UV-vis spectra of a paddlewheel moiety with two coordinated bptz linkers in the presence of CF, ACN and NM also produce a blue-shift trend from **1a** > **1b** > **1c** (Fig. S12, see ESI for computational details). Therefore, the overall observed blue shift upon guest exchange results from a combination of weakening of the C-H···N interactions due to ligand rotation, and changes in host-guest interactions.

Owing to the blue-shift and the solvatochromism of **1a,** the solvent exchange process from **1a** to **1b** or to **1c** could be

studied visually. The change in colour was not easily discernible when viewed with normal light, and polarised light was therefore used to enhance the observations. Each crystal was oriented with its large (01-1) facet facing the camera and, because blue provides a better contrast than yellow, its long axes normal to the direction of polarisation. The crystals were doused with ACN or NM and time-lapse photography was used to record the solvent exchange process in each case. The initial colour darkens when CF is exchanged with ACN and NM, and is suitable for visually tracking the progress of the solvent through the crystal (Fig. 2). For both ACN and NM the solvent enters via facets (212) and (-2-1-2), forming an hourglass-shaped pattern reminiscent of the arrangement of polar molecules diffused into organic crystals containing 1D channels.[13] The latter is not due to a difference in rate of diffusion (or exchange), but is rather a result of a systematically decreasing probability of the alignment of the polar molecules away from the centre of the crystal. Similarly, the hourglass patterns observed for sectional zoning, which results from the facet-selective inclusion of organic dyes into calcite crystals during their growth,[14] as well as a reported case of a thermally induced structural transition[15] arise from variations in the process of crystallisation. That is, they are due to different physical properties and not the diffusion of solvent molecules into the crystal.

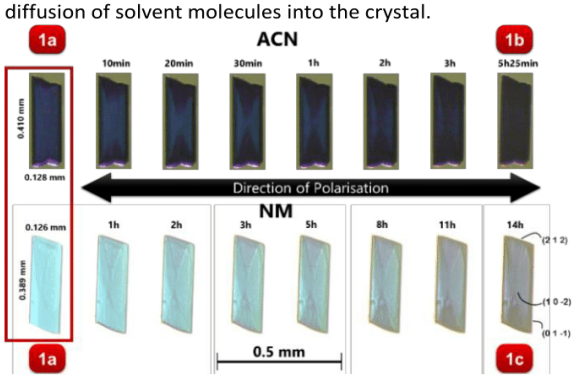

Fig. 2 Time-lapse photomicrographs of the solvent exchange processes of ACN and NM from 1a to 1b and 1c with the lapsed time for each photograph indicated above the crystals. The colour difference in 1a is due to optimisation of the lighting conditions for optimum contrast. The crystal faces determined by face-indexing (using SCD) are indicated on the bottom-left photograph.

For similarly sized crystals complete darkening requires about 5.5 hours for ACN and 14 hours for NM. We can gain further insight into the solvent exchange process by overlaying the crystal habit with the crystal structure and mapped channels of **1a** (Fig. S13; facets used to determine the habit were identified by face-indexing several crystals using Bruker's APEX II software, see ESI). The channels are angled relative to both the (212) and (10-2) facets, thereby opening onto both surfaces, but they do not protrude through the (01-1) facet (Fig. 2 and Fig. S13). Although this implies that guest molecules can enter the crystal at both the (212) and (10-2) facets, Fig. 2 shows that the solvent only enters from (212) facet.

The Adsorption Locator module of the Biovia Materials Studio 7.0 Software Suite uses simulated annealing (molecular dynamics simulating heating and cooling) and Monte Carlo searches of the configurational space of the substrate-adsorbate system during the cooling process to simulate the adsorption of molecules onto a specified surface of a crystal (see ESI for details). This has the effect of allowing the guest molecules to be released from and reattached to the crystal surface; the process is repeated a number of times to ensure that statistically meaningful results are obtained (parameters given in the ESI, Fig. S14). The $\Delta H_{adsorption}$ values (Fig. S15) are in the range of moderate to weak *metal—ligand* bond dissociation energies,[16] suggesting that the values are slightly high, nevertheless, the relative differences and trends are still relevant. ACN and NM both have a significantly higher $\Delta H_{adsorption}$ for (212) compared to (10-2) (relative $\Delta H_{adsorption}$ of 6.07 and 3.75 kcal mol^{-1} for ACN and NM, respectively). Moreover the $\Delta H_{adsorption}$ for ACN is always higher than that for NM (relative $\Delta H_{adsorption}$: 0.65 and 2.97 kcal mol^{-1} for (10-2) and (212), respectively) (Fig. S15). This could be attributed to ACN having a higher dipole moment (4.5 D)[17] as compared to NM (3.56 D),[18] thus increasing the electrostatic interaction of ACN with the crystal surfaces. Furthermore, the (212) facet comprises open metal sites and free pyridyl moieties, resulting in strong positive and negative electrostatic potential sites not present on (10-2). This yields stronger solvent interactions with (212) compared to (10-2) and subsequently a higher $\Delta H_{adsorption}$ for (212) relative to (10-2) (Fig. S15). This difference in calculated $\Delta H_{adsorption}$ values explains the slower solvent-exchange rate observed in the optical microscopy experiments for NM (taking 5 hours to produce the hourglass pattern, while ACN requires only 30 minutes, Fig. 2), although differences in diffusion rates within the channels are also expected to play a role. The large difference in adsorption enthalpies between (212) and (10-2) for both ACN and NM is responsible for the surface recognition effect and supports the optical microscopy observations that solvent entry occurs first via (212), and then via (10-2) over a longer period of time. Similarly, surface recognition is a key factor in the elucidation of the sectional zoning phenomenon of dye-included calcite crystals[14] and the formation of polarity in crystals by polar molecules diffusing into 1D channels.[13] Nevertheless, it is not obvious why the solvent-exchange process yields the observed hourglass-shaped pattern in this case. Overlaying the crystal structure of **1a** with its crystal habit (Fig 3a) reveals a solvent exchange pattern with only the two opposite corners involved in the exchange process. This solvent exchange pattern arises from the channels being angled relative to both the (212) and the (10-2) facets (Fig 3a). The pattern produced is thus inconsistent with the observation of the hourglass shape (Fig. 3a), indicating that a single crystal of **1a** cannot produce the observed solvent exchange pattern.

A closer examination of single crystals of **1a** -revealed that only the larger crystals have an elongated double ribbon shape (Fig. 3b). This growth morphology is indicative of twinning although no evidence of twinning was observed in the SCD data. The observed crystal morphology and twinning features are consistent with the "two re-entrant corner effect" (Fig. 3b),[19] which results in a crystal with four domains where the corner-opposite domains are identical (Fig. 3c). Combining this with the knowledge that the solvent enters (212) first, we can construct

the proposed model shown in Fig. 3d. This model is similar to intergrowth structures reported for zeolite crystals.[20] With the channels angled in towards the centre of the crystal, the solvent can enter via facet (212), thus producing the hourglass-shaped pattern observed using optical microscopy.

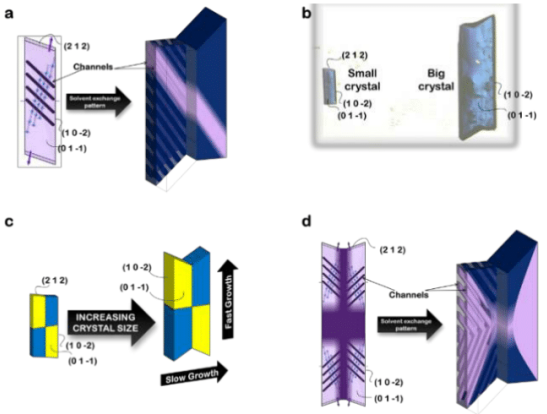

Fig. 3 a) The expected solvent exchange pattern of a single crystal of 1a. b) Actual crystals with facets indicated. c) A diagrammatic representation of a two re-entrant corner effect resulting in a growth-twinned crystal with four domains and an elongated ribbon shape. d) The solvent exchange pattern expected for the proposed twinned morphology. The face-indexed facets are indicated on the crystals and diagrams.

In conclusion, a 1D PCP (**1a**) with channels occupied by chloroform molecules has been prepared using the chromophore dptz as a linker. **1a** was shown to undergo a phase change and solvatochromism upon solvent exchange with acetonitrile and nitromethane. The solvatochromism allowed tracking of the solvent progress through a single crystal using time-lapse polarised light optical microscopy. Observation of the solvent-exchange process revealed an hourglass-shaped pattern with solvent entering through facet (212) first, and after considerably more time, through (10-2). MM adsorption simulations showed that the difference in exchange rate between the two crystal-faces is due to (212) having a larger $\Delta H_{adsorption}$ compared to (10-2). The observed solvent-exchange pattern is inconsistent with a pattern that would result from a single crystal. We have proposed a twinned crystal with a two re-entrant corner effect, which results in a growth morphology consistent with **1a** single crystals and reproduces the observed solvent-exchange pattern. The unique combination of surface selectivity and solvatochromism exhibited by **1a** has therefore provided us with a means of explaining the mechanism by which it undergoes solvent exchange, and has allowed us to identify the presence of an unusual mode of crystal growth (yielding twinning) that would otherwise have gone unnoticed.

We thank the National Research Foundation (NRF) of South Africa and Stellenbosch University for financial support, as well as the Centre for High Performance Computing (CHPC) in Cape Town, South Africa for computational resources.

Notes and references

1 (a) Q.-L. Zhu, Q. Xu, *Chem. Soc. Rev*., 2014, **43**, 5468; (b) J. Li, J. Sculley, H. Zhou, *Chem. Rev.*, 2012, **112**, 869; (c) S. Chaemchuen, N. A. Kabir, K. Zhou, F. Verpoort, *Chem. Soc. Rev.*, 2013, **42**, 9304; (d) B. Li, H. Wang, B. *Chen, Chem. Asian J.*, 2014, **9**, 1474; (e) S. Qiu, G. Zhu, Coord. *Chem. Rev*., 2009, **253**, 2891; (f) H. Deng, C. J. Doonan, H. Furukawa, R. B. Ferreira, J. Towne, C. B. Knobler, B. Wang, O. M. Yaghi, *Science*, 2010, **327**, 846; (g) Z. Wang, S. M. Cohen, *Chem. Soc. Rev*., 2009, **38**, 1315.

2 (a) N. Stock, S. Biswas, *Chem. Rev.,* 2012, **112**, 933; (b) X.-L. Tong, H.-L. Lin, J.-H. Xin, F. Liu, M. Li, X.-P. Zhu, *J Nanomater.,* 2013, **2013**, 11.

3 (a) M. Bosch, M. Zhang, H.-C. Zhou, *Adv. Chem.,* 2014, **2014**, 8; (b) M. L. Foo, R. Matsuda, S. Kitagawa, *Chem. Mater.,* 2014, **26**, 310; (c) S. Kitagawa, R. Kitaura, S.-i. Noro, *Angew. Chem. Int. Ed.,* 2004, **43**, 2334.

4 (a) J.-R. Li, Y. Ma, M. C. McCarthy, J. Sculley, J. Yu, H.-K. Jeong, P. B. Balbuena, H.-C. Zhou, *Coord. Chem. Rev.,* 2011, **255**, 1791; (b) B. Chen, S. Xiang, G. Qian, *Acc. Chem. Res.,* 2010, **43**, 1115; (c) Y. Cui, Y. Yue, G. Qian, B. Chen, *Chem. Rev.,* 2011, **112**, 1126.

5 (a) Q. Zhou, P. Audebert, G. Clavier, R. Méallet-Renault, F. Miomandre, Z. Shaukat, T.-T. Vu, J. Tang, *J. Phys. Chem. C,* 2011, **115**, 21899; (b) J. Li, D. Jia, S. Meng, J. Zhang, M. P. Cifuentes, M. G. Humphrey, C. Zhang, *Chem. Eur. J.,* 2015, **21**, 7914; (c) Y. Takashima, V. M. Martínez, S. Furukawa, M. Kondo, S. Shimomura, H. Uehara, M. Nakahama, K. Sugimoto, S. Kitagawa, *Nat. Commun.*, 2011, **2**, 168.

6 (a) C. J. Hawker, K. L. Wooley, J. M. J. Frechet, *J. Am. Chem. Soc.,* 1993, **115**, 4375; (b) F. Würthner, G. Archetti, R. Schmidt, H.-G. Kuball, *Angew. Chem. Int. Ed.,* 2008, **47**, 4529; (c) L. G. S. Brooker, G. H. Keyes, *J. Am. Chem. Soc.,* 1951, **73**, 5356.

7 (a) Z.-Z. Lu, R. Zhang, Y.-Z. Li, Z.-J. Guo, H.-G. Zheng, *J. Am. Chem. Soc.,* 2011, **133**, 4172; (b) C.-Y. Sun, X.-L. Wang, C. Qin, J.-L. Jin, Z.-M. Su, P. Huang, K.-Z. Shao, *Chem. Eur. J.,* 2013, **19**, 3639.

8 C. She, S. J. Lee, J. E. McGarrah, J. Vura-Weis, M. R. Wasielewski, H. Chen, G. C. Schatz, M. A. Ratner, J. T. Hupp, *Chem. Commun.,* 2010, **46**, 547.

9 A. D. McFarland, R. P. Van Duyne, *Nano Letters,* 2003, **3**, 1057.

10 (a) M. A. Geday, W. Kaminsky, J. G. Lewis, A. M. Glazer, *J. Microsc.,* 2000, **198**, 1; (b) H. Honda, H. Kimura, Y. Sanada, *Carbon,* 1971, **9**, 695; (c) C. D. Gribble, A. J. Hall, Optical Mineralogy: Principles and Practice, UCL Press, Taylor and Francis Group, London, 1992.

11 S. Takamizawa, *Angew. Chem. Int. Ed.,* 2015, **54**, 7033.

12 M. Plugge, V. Alain-Rizzo, P. Audebert, A. M. Brouwer, *J. Photochem. Photobiol., A: Chem.,* 2012, **234**, 12.

13 (a) A. Batagiannis, T. Wüst, J. Hulliger, *J. Math. Chem.,* 2009, **45**, 869; (b) A. Quintel, J. Hulliger, M. Wübbenhorst, *J. Phys. Chem. B,* 1998, **102**, 4277.

14 B. Kahr, R. W. Gurney, *Chem. Rev.,* 2001, **101**, 893.

15 D. Bahat, *Am. Mineral.,* 1974, **59**, 139.

16 (a) G. Pilcher, *Pure Appl. Chem.,* 1989, **61**, 855; (b) S. Strömberg, M. Svensson, K. Zetterberg, *Organometallics,* 1997, **16**, 3165.

17 T. Ohba, S. Ikawa, *Mol. Phys.,* 1991, **73**, 985.

18 J. F. Coetzee, T.-H. Chang, *Pure & Appl. Chem.,* 1986, **58**, 1541.

19 (a) R. I. Kostov, *Mineralogical Magazine,* 2006, **70**, 129; (b) H. Miyahara, S. Nara, K. Ogi, in *Photovoltaic Energy Conversion, Conference Record of the 2006 IEEE 4th World Conference on, Vol. 1*, 2006, pp. 1219.

20 L. Karwacki, E. Stavitski, M. H. F. Kox, J. Kornatowski, B. M. Weckhuysen, *Angew. Chem. Int. Ed.,* 2007, **46**, 7228.

5.2. SUPPORTING INFORMATION

Materials and synthesis

All chemicals were obtained from commercial sources (mainly Sigma Aldrich) and used without further purification. The 3,6-di(pyridin-4-yl)-1,2,4,5-tetrazine (dptz) linker was synthesised according to reported procedures[S1].

Single-crystal X-ray Diffraction

Suitable single-crystals were selected and loaded onto the diffractometer using a MiTeGen MicroCrystal mounts. Single-crystal X-ray diffraction data were collected using a SMART diffractometer with an APEX-II CCD area-detector using an Oxford Cryosystems 700Plus cryostat for temperature control. X-rays were generated from a sealed tube (MoKα radiation λ = 0.71073 Å) fitted with a multilayer monochromator. All data were collected at 100 K.

Data reduction was carried out by means of the standard procedure using the Bruker software package SAINT2 and the absorption corrections and the correction of other systematic errors were performed using SADABS.3. Using Xseed [S2] and Olex2 [S3], the structure was solved with the ShelXS [S4] structure solution program using Direct Methods and refined with the ShelXL [S5] refinement package using least squares minimisation. Hydrogen atoms were placed in calculated positions using riding models.

Thermogravimetric analysis (TGA)

Thermogravimetric analysis was conducted using a TA Instrument Q500. The sample is loaded in an aluminium pan and heated from room temperature at 10 °C/min up to 600°C.

Time-Lapsed Polarized-light Optical Microscopy

Single crystals of the chloroform solvate (**1a**) were immersed in acetonitrile and nitromethane and sealed within a chamber with windows at the top and bottom. Adjustment (lighting, crystal position, polarizer, etc.) were made very quickly and pictures were taken every 10 seconds.

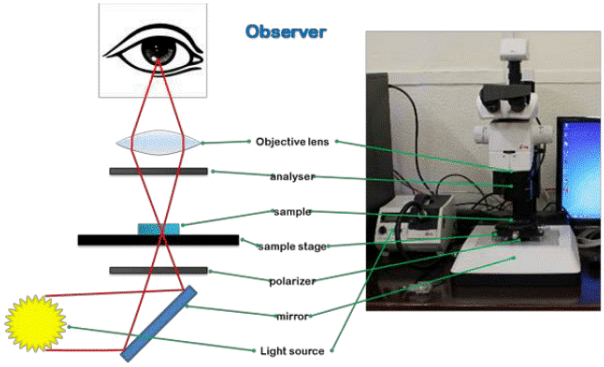

Scheme 1. The Leica optical microscope setup used in the solvent-exchange experiments.

Computational Methods

Geometry Optimizations and Atomic charges

Only the hydrogen atoms of the frameworks are optimized as part of a periodic system using the CASTEP module of the Materials Studio software suite.[S6] The optimization was performed using the GGA PBE functional with Grimme's DFT-D dispersion correction; thresholds for geometry optimization and SCF convergence were chosen as 1×10^{-6} eV. The Milliken charges were calculated at the end of the optimisation process (this is given as an option in the properties tab of the calculation setup). These atomic charges are used in all the subsequent molecular mechanics calculations.

DMol^3 UV-vis calculations

UV-vis data was calculated at the end of the optimization step using the DMol^3 module within the Biovia Materials Studio software suite.[S6-S8] The optimization was performed using the The Perdew et al.[S9] generalized gradient approximation (GGA/PBE) for the exchange–correlation functional [S10] and the dispersion corrected with Grimme's DFT-D. The thresholds for the geometry optimizations and SCF convergence were chosen as 1×10^{-6} eV. An all-electron core treatment with the TNP basis (Triple Numerical plus polarization) was chosen to describe the electronic structure for the organic models and the Effective Core Potentials with a DNP (Double Numerical plus polarization) basis was chosen for the models containing copper cations.[S11] The UV-vis spectra were calculated at the GGA/PBE level using TD-DFT with the ALDA (adiabatic local exchange functional approximation) approach that is recommended by the DMol^3 author as a cost-efficient implementation of TD-DFT.[S12] The TD-DFT excitations were calculated using the **ALDA** kernel with exchange-correlation terms included, other options include: **ALDAx** - calculates TD-DFT excitations using a modified ALDA kernel with the exchange term only; **RPA** - no exchange-correlation response, only electrostatic response included) for calculating the 50 lowest singlet states.[S13, S14] Only the grid data for 10 orbitals above and below the Fermi level were calculated for visualization.

Adsorption calculations

All adsorption calculations were performed using the Adsorption Locator module within the Biovia Materials Studio software suite.[S6] This module allows for the simulation of pure and mixed adsorbates, with fixed composition, onto a substrate. The Adsorption Locator module identifies possible adsorption sites by carrying out Monte Carlo searches of the configurational space of the substrate-adsorbate system as the temperature is slowly decreased within the simulated annealing process of a molecular dynamics run. [S15-S18] In this work we simulated the adsorption of a solvent molecules onto particular crystal facets in order to acquire relative interaction strengths of the different solvents with the different crystal facets. This can provide insight into the facet preferences of solvent exchange processes. The adsorption locator is essentially a simulated annealing simulation with geometry optimizations in-between successive heat-cool cycles. A model several unit cells in size were constructed and cleaved along a plane ([10-2] and (2 1 2)) to create the appropriate crystal face onto which a vacuum slab is added. One hundred adsorbate molecules were introduced into the vacuum as part of the simulated annealing calculation. The isosteric heat, or enthalpy of adsorption, can be extracted from the adsorption calculation and is an average over all the lowest energy configurations (obtained using Monte Carlo simulations) returned after each annealing cycle of the MD run. 30 cycles containing 1 000 000 steps per cycle with annealing temperatures of 298 to 500 K were used for reproducible results. The Monte Carlo parameters were set to a probability of 0.29 (ratio = 1) for 'conformer', 'rotate' and 'translate' while 'regrow' was set to 0.14 (ratio = 0.5). The

COMPASS force field (COMPASS II 1.0)[S19] was used in conjunction with atomic charges calculated using CASTEP single point energy calculations. Ewald and group based summation methods were chosen for the electrostatic and van der Waals energy components respectively with the cut-off's set at 25 Å. The parameterisation and validation of COMPASS for metal oxides was performed by Zhao and co-workers. [S20] The list of models covered by the COMPASS II 1.0 force field is given below:

Table S1. All the models covered by the COMPASS II 1.0 force field.

COMPASS II 1.0 - Group A - Covalent Model			
Alkanes	C_nH_{2n+2}	Carbamates/urethanes	-OCONH-
Alkenes	C_nH_{2n}	Siloxanes	-Si-O-Si-
Alkynes	C_nH_n	Silanes	-Si-Si-
Benzenes/Aromatics	C_6H_6, -C_6H_5, $C_{12}H_{10}$	Small molecules	O_2, N_2, H_2, H_2O, CO, CO_2, CS_2, SO_2, SO_3, NO, NO_2, NH_3, He, Ne, Ar, Kr, Xe
Cycloalkanes	C_nH_{2n}	Alkyl halides	R-X (X=F, Cl)
Ethers	-R-O-R-	Phosphazenes	-N=PX_2- (X=F, Cl, NR, OR, R)
Acetals	-$C(OR)_2$-	Nitro groups	-NO_2
Alcohols	-R-OH	Nitriles	R-CN
Phenols	Ar-OH	Isocyanides	RNCO
Amines	-NR_2	Sulfides	RSR
Ammonia	NH_3	Thiols	RSH
Aldehyde/ketone	-CO-	Amineoxides	NR_3O
Acids	-COOH	Aromatic halides	Ar-Cl, Ar-F
Esters	-COO-	Cyanamides	-N=C=O
Carbonates	-OCOO-	Nitrates	R-O-NO_2
Amides	-CONH-	Sulfates	-SO_4-
		Sulfonates	RSO_2O-
COMPASS II 1.0 - Group B - Ionic Model			
Metals	Al, Na, Pt, Pd, Au, Ag, Sn, K, Li, Mo, Fe, W, Ni, Cr, Cu, Pb, Mg		
Metal halides	Li^+, Na^+, K^+, Rb^+, Cs^+, Mg^{2+}, Ca^{2+}, Fe^{2+}, Cu^{2+}, Zn^{2+}, F^-, Cl^-, Br^-, I^-		
Silica/Aluminosilicates	SiO_2, AlO_2		
Metal oxides	Li_2O, Na_2O, K_2O, MgO, CaO, SrO, BaO, TiO_2, Fe_2O_3, Al_2O_3, SnO_2, SiO_2, CuO		

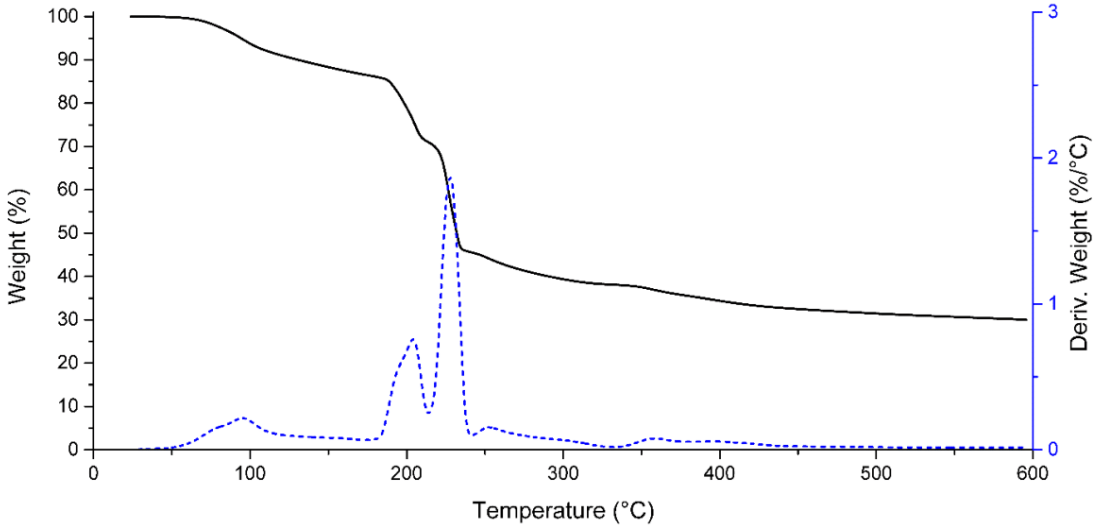

Fig. S1 TGA of **1a** from RT to 600 °C.

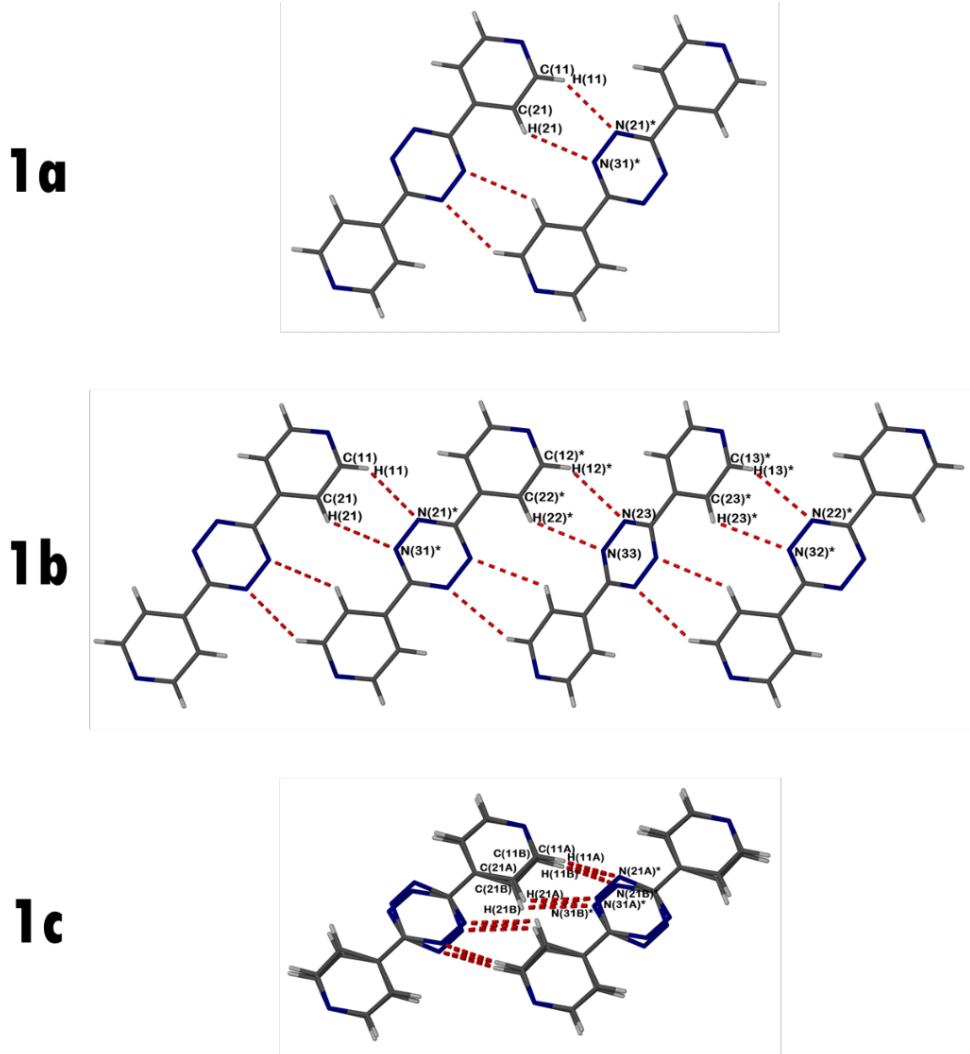

Fig. S2. The C—H···N contacts for the dptz ligands of **1a**, **1b** and **1c**.

Table S2. C—H···N contacts for the dptz ligands of **1a**, **1b** and **1c**.

	D—H···A	Distance (D—A)	Angle (D—H···A)
1a	C(11)—H(11)···N(21)*	3.469(2)	142.52
	C(21)—H(21)···N(31)*	3.440(2)	134.87
1b	C(11)—H(11)···N(21)*	3.494(4)	126.14
	C(12)*—H(12)*···N(23)	3.573(4)	139.76
	C(13)*—H(13)*···N(22)*	3.518(4)	128.97
	C(21)—H(21)···N(31)*	3.481(4)	117.14
	C(22)*—H(22)*···N(33)	3.547(4)	130.97
	C(23)*—H(23)*···N(32)*	3.475(4)	122.26
1c ($A_{S.O.F}$– 0.6301) ($B_{S.O.F}$– 0.3699)	C(11A)—H(11A)···N(21A)*	3.595(6)	124.50
	C(11A)—H(11A)···N(21B)*	3.382(6)	127.54
	C(11B)—H(11B)···N(21A)*	3.677(6)	112.06
	C(11B)—H(11B)···N(21B)*	3.437(6)	116.02
	C(21A)—H(21A)···N(31A)*	3.602(6)	135.61
	C(21A)—H(21A)···N(31B)*	3.372(6)	141.20
	C(21B)—H(21B)···N(31A)*	3.689(6)	124.84
	C(21B)—H(21B)···N(31B)*	3.429(6)	131.00

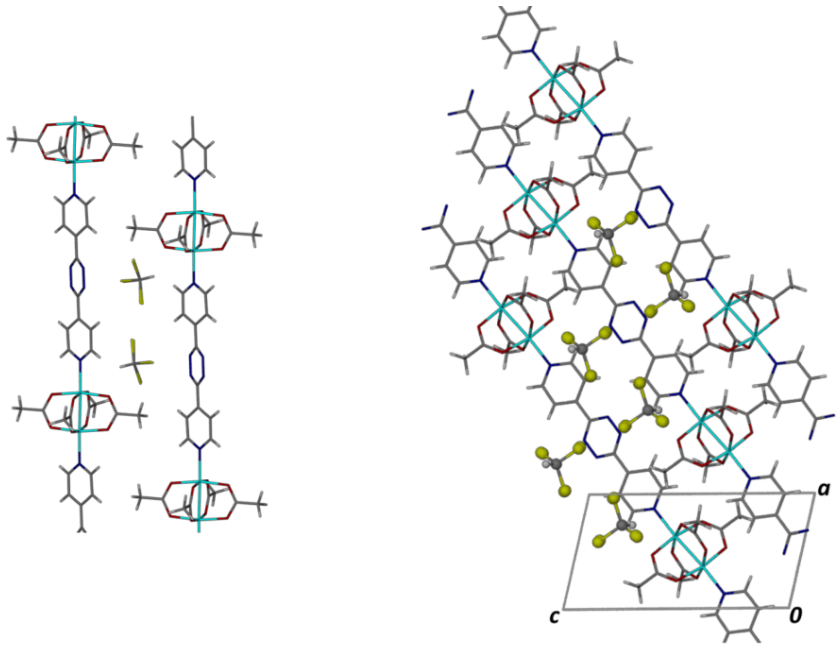

Fig. S3 The interactions of chloroform with the dptz linkers in **1a**.

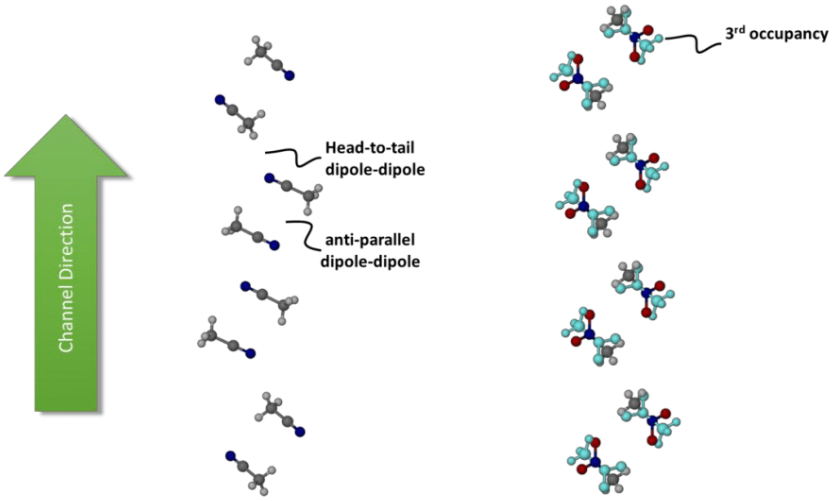

Fig. S4 Left – the acetonitrile guest molecule arrangement within the 1D channel with the channel direction along [0 1 1]. Right – disordered nitromethane which can also form head-to-tail and anti-parallel dipole-dipole interactions (channel direction along [1 0 0]).

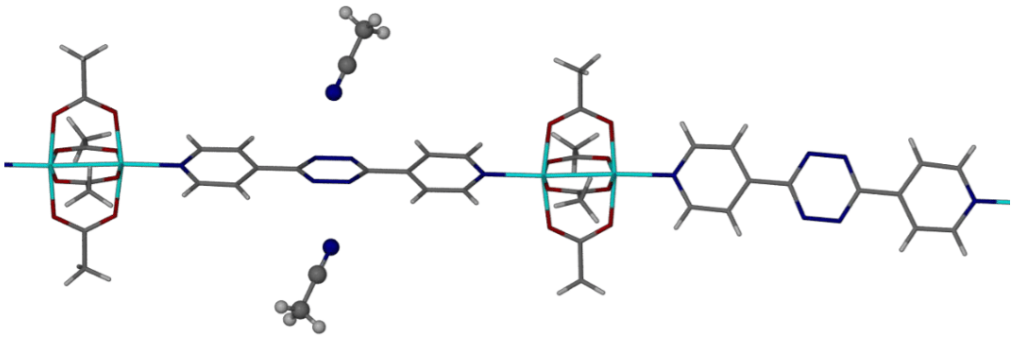

Fig. S5 Head-on interaction of acetonitrile molecules with every 3rd out-of-plane twisted dptz linker.

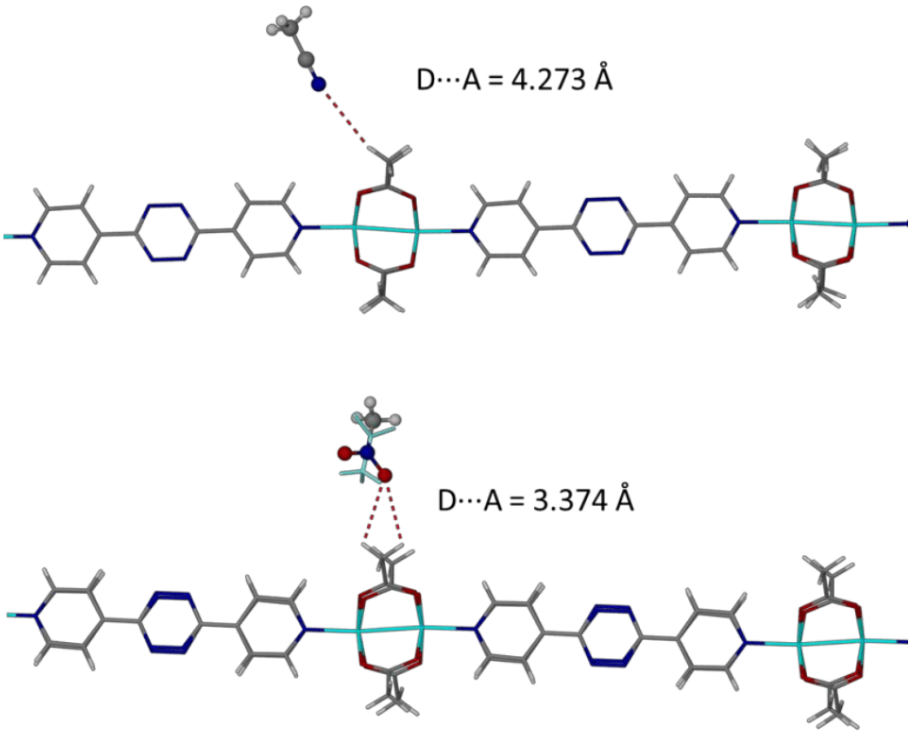

Fig. S6 The hydrogen bonding (electrostatic interaction) of acetonitrile and nitromethane with the methyl-group of the acetate moiety.

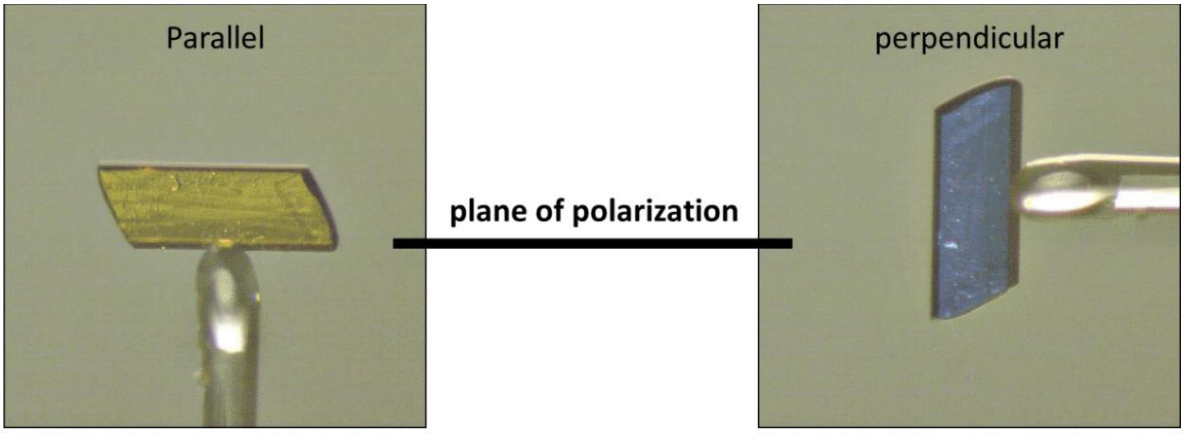

Fig. S7 The colour of a **1a** single crystal parallel and normal to the plane of polarization as viewed through an optical microscope.

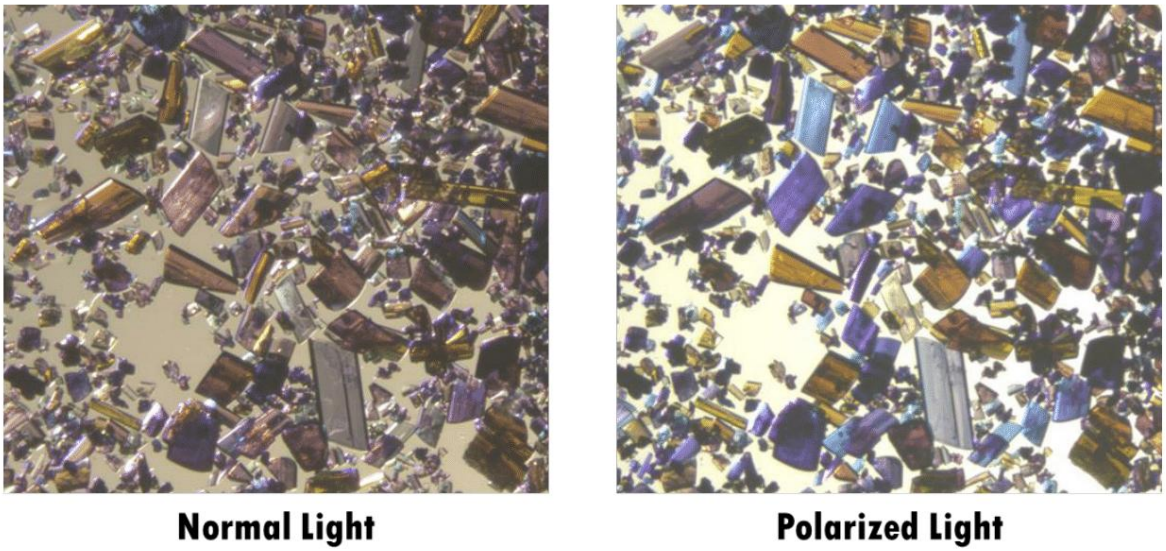

Fig. S8 Left - Crystals of **1a** viewed without a polarizer (the mirror at the bottom of the microscope could slightly polarize the light). Right – Crystals of **1a** viewed with polarized light showing the colour enhancement. The colour of the crystals vary depending on the orientation of the crystals thus illustrating the pleochroism of **1a**.

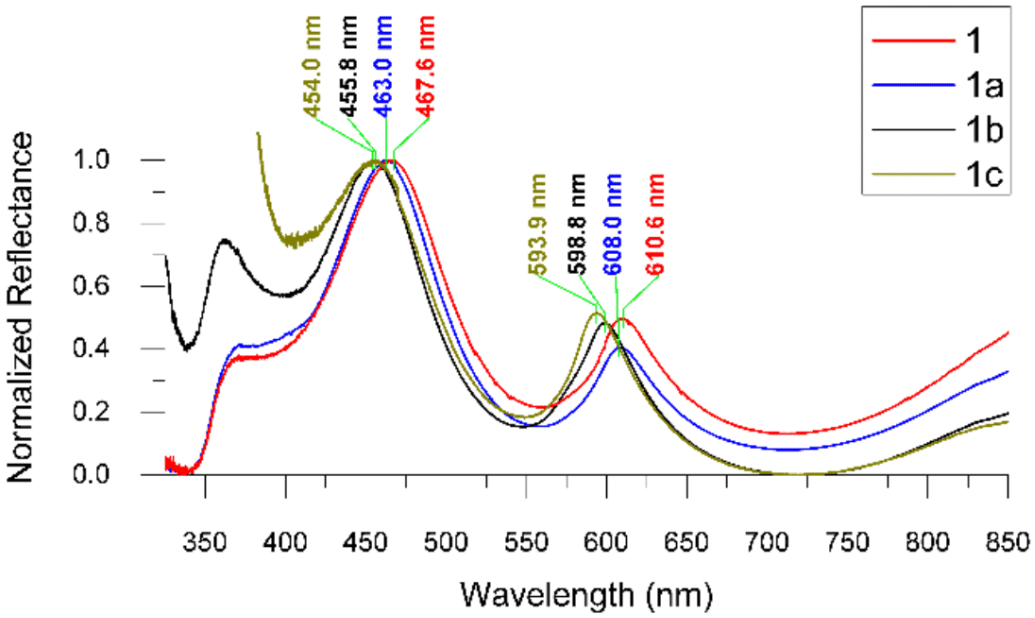

Fig. S9 Normalized reflectance UV-vis spectra of the activated PCP and the three solvates. The peaks of interest are indicated with the green lines.

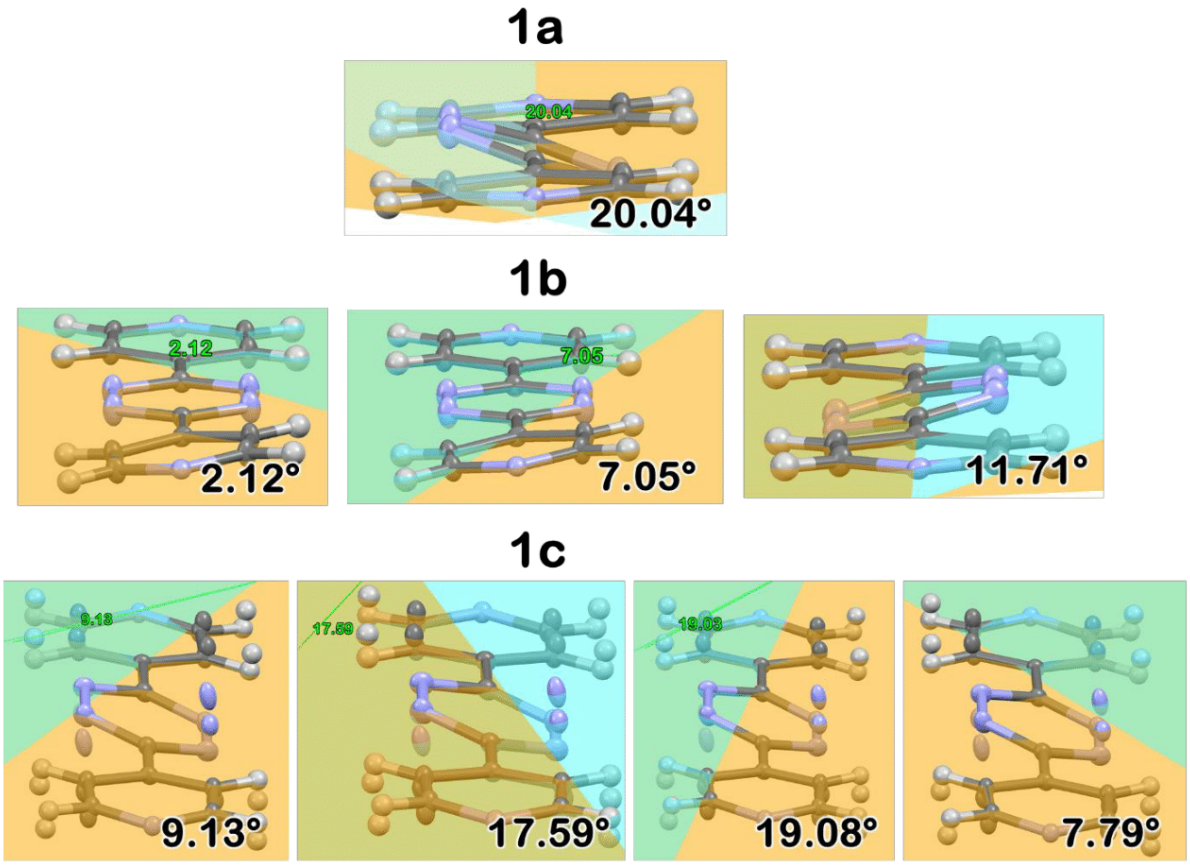

Fig. S10 The tilt angles between the tetrazine and pyridyl rings measured using the Mercury 3.7 software.[S21]

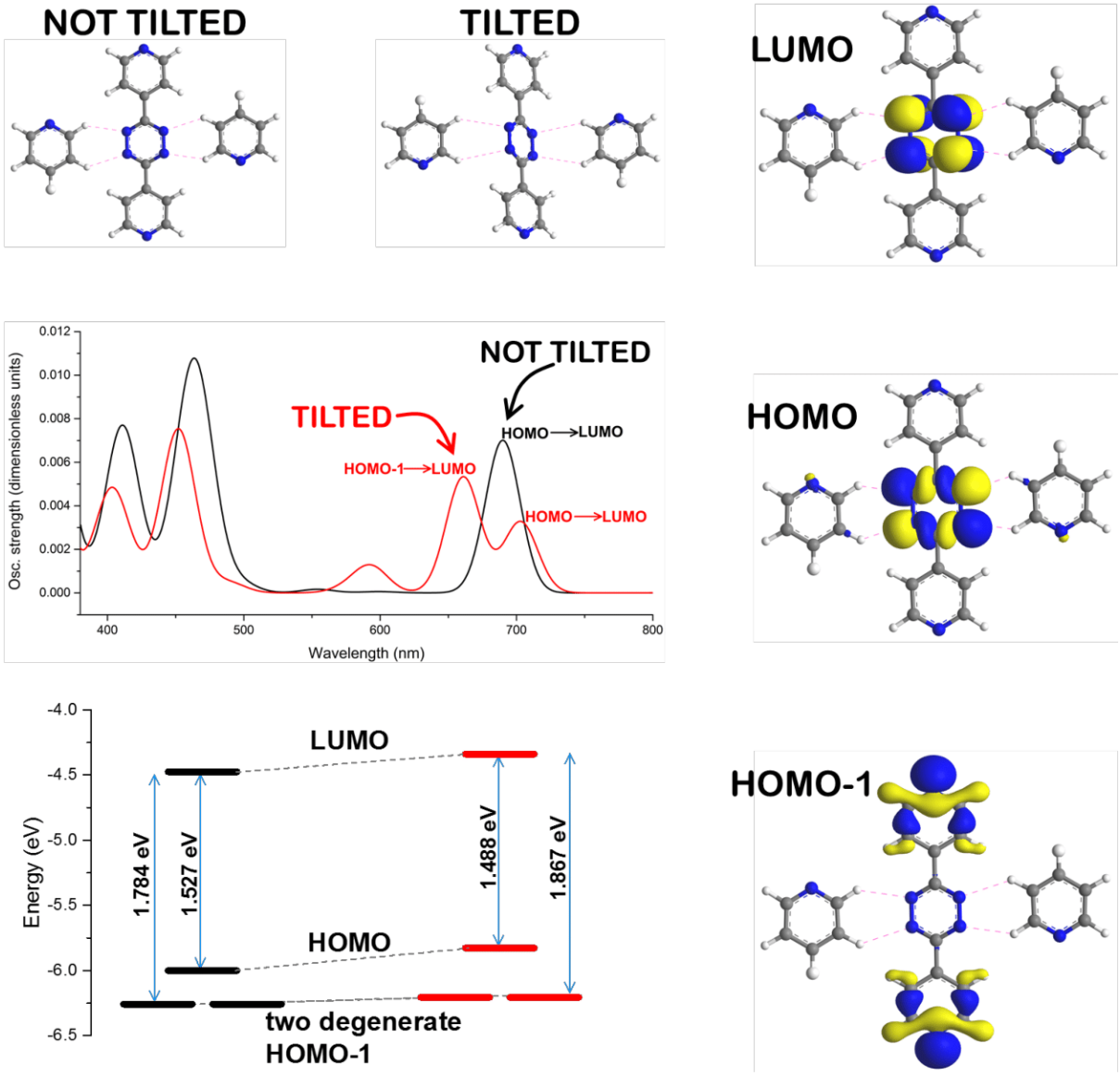

Fig. S11. UV-vis calculations using a single dptz molecule surrounded by 2 pyridine molecules forming C–H···N electrostatic interactions. The dptz molecule was tilted by 45° with respect to its original orientation. The UV-vis spectra and frontier orbitals was calculated for both scenarios. Bottom-Left: the energy diagram for the frontier orbitals. Left: visualization of the frontier orbitals of interest. These calculation were performed using the DMol^3 module in the Materials Studio software package.[S6]

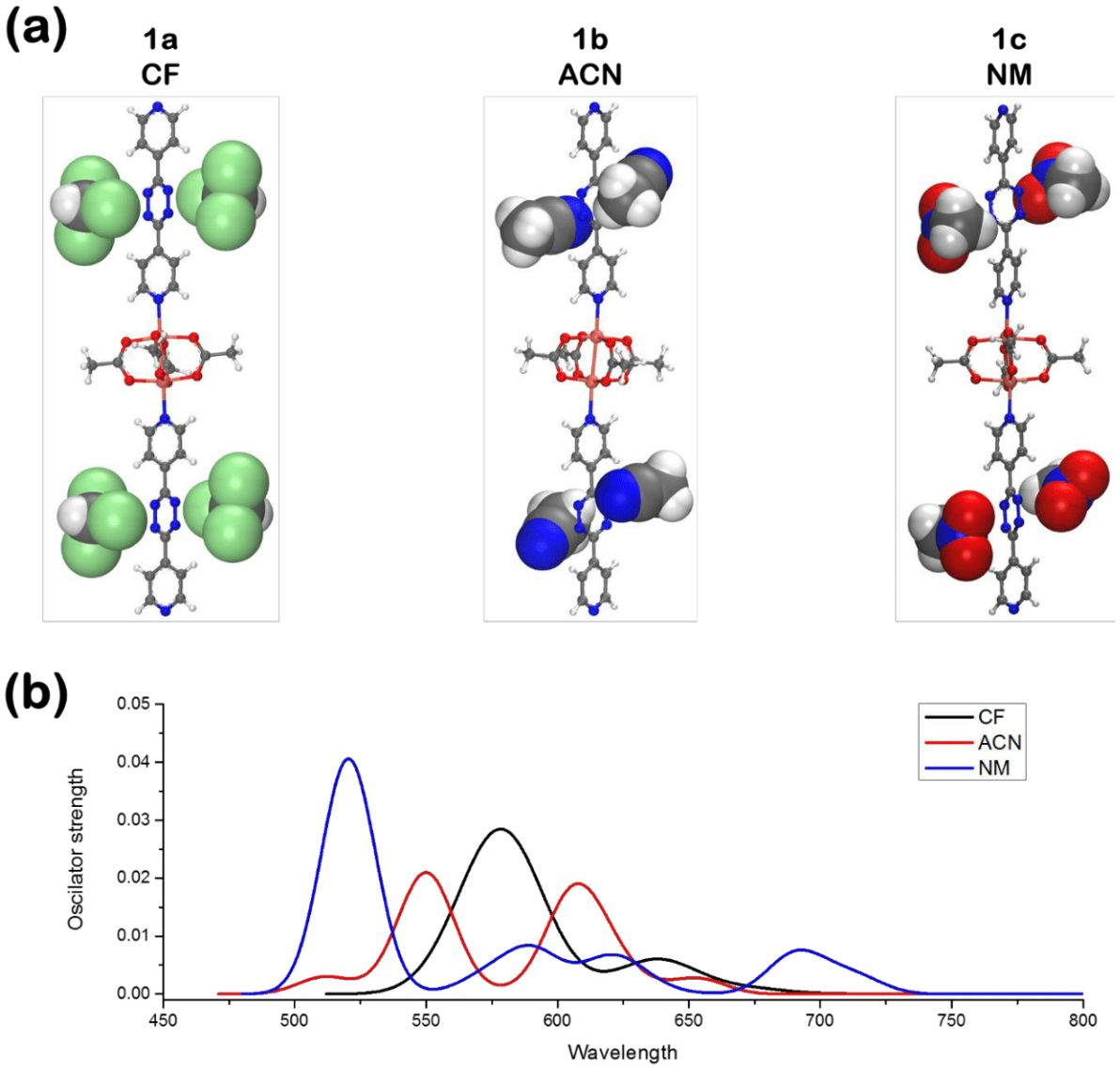

Fig. S12. UV-vis calculations using a paddlewheel moiety with two coordinated dptz linkers and the three solvents. (a) The computational models used for the UV-vis calculations. The solvent molecules is shown in space filling representation. (b) The UV-vis absorption spectra generated using these models. These calculation were performed using the DMol^3 module in the Materials Studio software package.[S6]

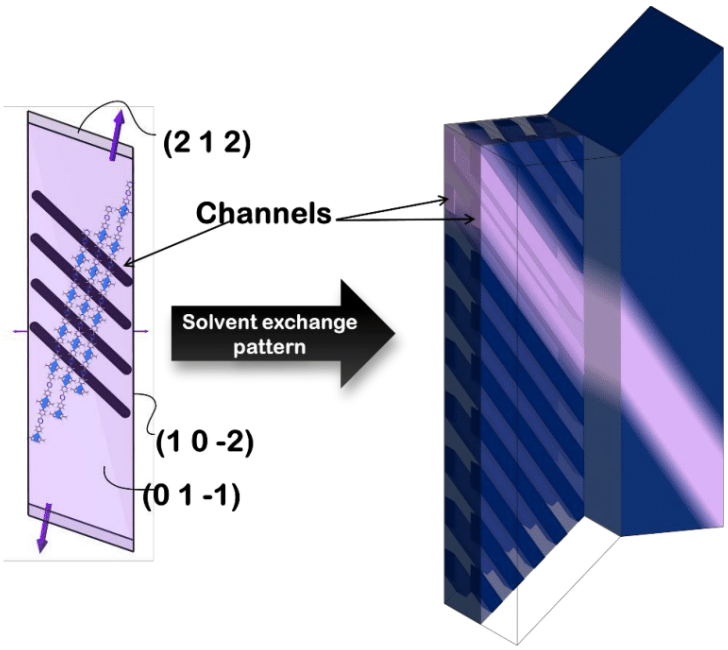

Fig. S13. Left: Overlay of the crystal structure and crystal habit with the channels and facets indicated. Right: Tthe resulting solvent exchange pattern of a single crystal with channels as shown in the overlay. The size and direction of the purple arrows indicate the growth rate of the facets.

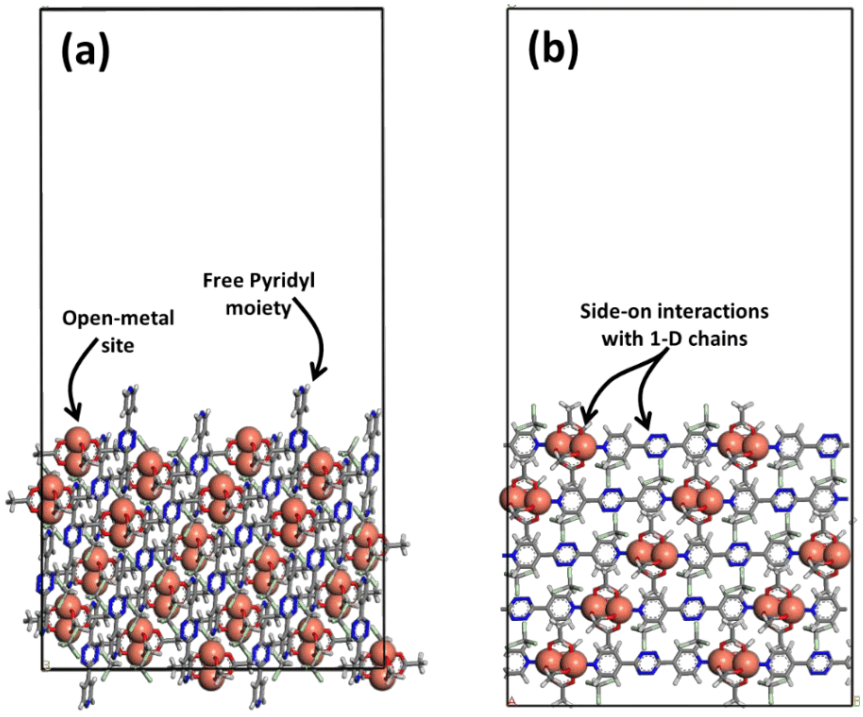

Fig. S14. The models used for the Adsorption Locator simulations with the copper atoms shown in space-filling representation and the rest of the model shown in stick representation. (a) (212) and (b) (10-2).

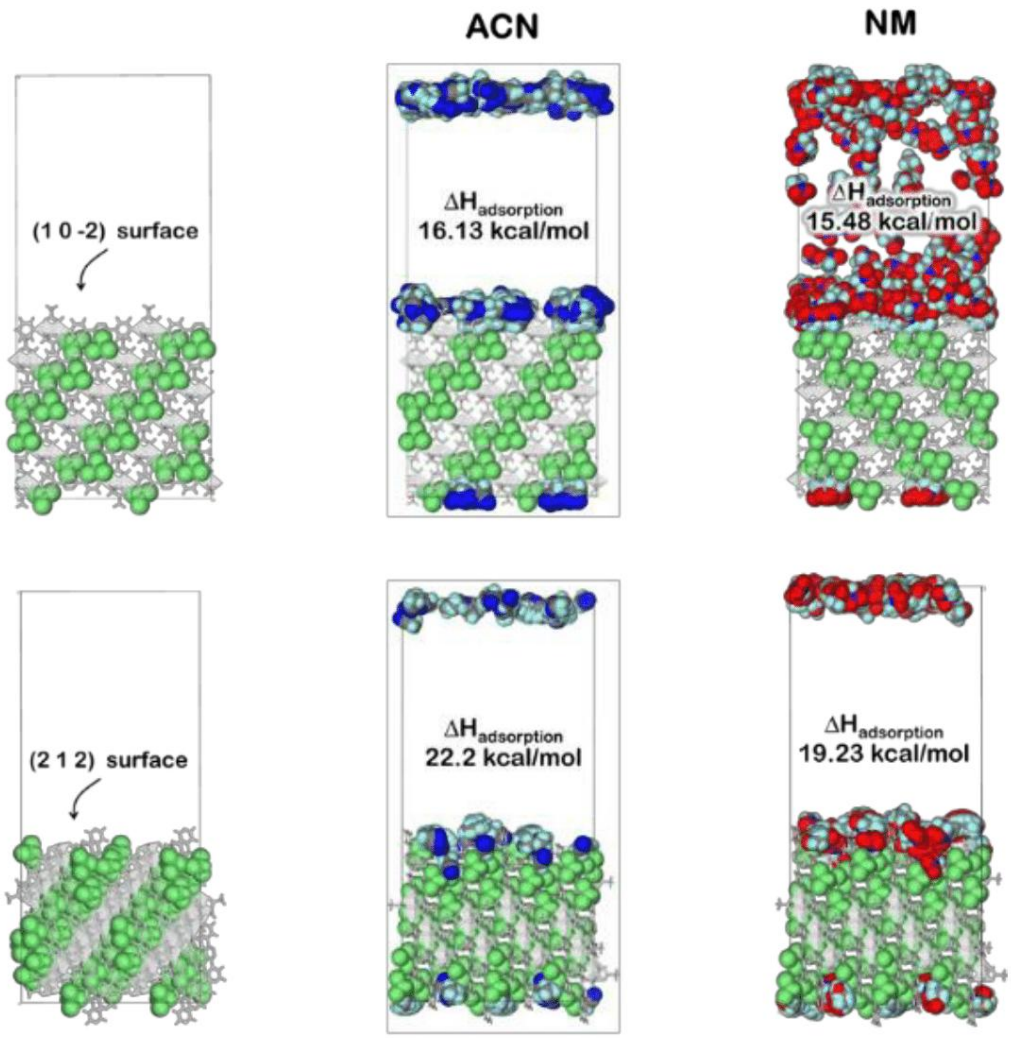

Fig. S15. Left – Molecular Mechanics models used to perform adsorption simulations of ACN and NM onto the (10-2) and (212) surfaces of a crystal of **1a**. Middle – ACN adsorption. Right – NM adsorption. Several snapshots were combined to produce the solvent-containing figures. Solvent molecules are represented in space-fill format and the coordination polymer in grey stick representation.

References

[1] Bakkali, H., et al., *Eur. J. Org. Chem.* **2008**, *2008*, 2156-2166

[2] (a) Atwood, J. L.; Barbour, L. J., *Cryst. Growth Des.* **2003**, *3*, 3-8; (b) Barbour, L. J., *J. Supramol. Chem.* **2001**, *1*, 189-191.

[3] Dolomanov, O.V., Bourhis, L.J., Gildea, R.J, Howard, J.A.K. & Puschmann, H., *J. Appl. Cryst.* **2009**, *42*, 339-341.

[4] Sheldrick, G.M., *Acta Cryst.* **2008**, *A64*, 112-122.

[5] Sheldrick, G.M., *Acta Cryst.* **2015**, *C71*, 3-8.

[6] Materials Studio Modeling Environment v7.0.0; Accelrys Software Inc.: San Diego, **2015**

[7] Delley, B., *J. Chem. Phys.* **1990**, *92*, 508-517.

[8] Delley, B., *J. Chem. Phys.* **2000**, *113*, 7756-7764.

[9] Perdew, J. P.; Burke, K.; Ernzerhof, M., *Phys. Rev. Lett.* **1996**, *77*, 3865-3868.

[10] Chen, F.; Johnston, R. L., *Acta Mater.* **2008**, *56*, 2374-2380.

[11] Inada, Y.; Orita, H., *J. Comput. Chem.* **2008**, *29*, 225-232.

[12] Delley, B., *J. Phys.: Condens. Matter* **2010**, *22*, 384208

[13] Vasiliev, I.; Öğüt, S.; Chelikowsky, J. R., *Phys. Rev. B* **2002**, *65*, 115416.

[14] Li, W.-Y.; Chen, F.-Y., *Chinese Physics B* **2014**, *23*, 117103.

[15] Metropolis, N.; Rosenbluth, A. W.; Rosenbluth, M. N.; Teller, A. H.; Teller, E., *J. Chem. Phys.* **1953**, *21*, 1087-1092.

[16] Kirkpatrick, S.; Gelatt, C. D.; Vecchi, M. P., *Science* **1983**, *220*, 671-680.

[17] Černý, V., *Journal of Optimization Theory and Applications* **1985**, *45*, 41-51.

[18] Frenkel, D.; Smit, B., *Understanding Molecular Simulation: From Algorithms to Applications*. Elsevier Science: 2001.

[19] Peng, Z.; Ewig, C. S.; Hwang, M.-J.; Waldman, M.; Hagler, A. T., *J. Phys. Chem. A* **1997**, *101*, 7243-7252.

[20] Zhao, L.; Liu, L.; Sun, H., *J. Phys. Chem. C* **2007**, *111*, 10610-10617.

[21] Macrae, C. F.; Bruno, I. J.; Chisholm, J. A.; Edgington, P. R.; McCabe, P.; Pidcock, E.; Rodriguez-Monge, L.; Taylor, R.; van de Streek, J.; Wood, P. A., *J. Appl. Crystallogr.* **2008**, *41*, 466-470.

Chapter 6

CONCLUDING REMARKS

The three sets of related MOFs described in this thesis have provided some insight into the subtleties of MOF properties and their dynamic host-guest interactions. The combination of experimental studies and molecular modelling is pivotal to a detailed understanding of the behaviour of such materials.

Three open-channel robust 3D MOFs, with varying pore dimensions constructed using 4,4´-bipyridyl linkers of different lengths, facilitates exploration of the effect of increasing pore dimensions on the sorption properties and dynamic host-guest interactions of the frameworks. These MOFs were synthesised hydrothermally to yield $[Cu_2(glu)_2(bpy)\cdot 2.9H_2O]_n$ (**1a**), $[Cu_2(glu)_2(bpe)\cdot 3H_2O]_n$ (**2a**) and $[Cu_2(glu)_2(bpymh)\cdot 7.5H_2O]_n$ (**3a**) as green block-shaped crystals. Since these MOFs have the same coordination topology and a varying ligand, they can be considered isoreticular. The crystals of these frameworks are extremely robust and survived dehydration under dynamic vacuum at 150 °C for 24 h to afford crystals of the apohosts **1**, **2** and **3**. There was no discernible deterioration in the crystals, thus demonstrating the stability of these MOFs. No significant change in the structures and unit cell parameters were observed. The channel dimensions of the MOFs increase from **1** to **3** as a result of the length of the varied linkers. Closer inspection of the guest-accessible space of the three MOFs revealed prominent corrugation of the channels. It was noted that the degree of corrugation of the channel could influence how guest molecules diffuse through the channels.

CO_2 adducts of the MOFs were obtained by solvent exchange of the as-synthesised crystals with CO_2 under supercritical conditions (**1b**, **2b**, **3b**). The samples were transported in a Dewar flask onto dry ice in order to maintain the guest occupancy during SCXRD and TGA analysis. From the crystal structures obtained, a well-defined sorption site could be discerned for **2b** and **3b**, while **1b** forms a sterically driven adduct. The sorption sites for **2b** and **3b** are centred on two carboxylate oxygen atoms directed into the channel. **1b** contains four CO_2 per unit cell, while **2b** and **3b** enclose eight molecules each.

The host-guest dynamics resulting from the combination of channel size and corrugation were explored using CO_2 gas sorption and thermal analysis of CO_2 adducts of all three MOFs. The sorption capacities for the three MOFs are in agreement with the CO_2 loaded structures with only **3** absorbing slightly more than eight molecules per unit cell. This is not surprising since MOF **3** still contains some accessible space in between the CO_2 molecules occupying the MOF sorption sites. However, the sorption isotherm for MOF **3** displays the least hysteresis, which we attribute to its large channel diameter. The sorption isotherm for **2** shows the highest degree of sorption hysteresis and CO_2 retention under vacuum. Numerous static-vacuum exposure (volumetric sorption apparatus) over a three day period were still insufficient

for complete desorption of the MOF, thus indicating the high retention stability of CO_2 within the framework. TGA was carried out for the same material used for the SCXRD analysis. There was a clear trend in the temperature of complete thermal evolution of the CO_2 guest molecules: **1** > **2** > **3**, corresponding to increasing channel size. For **1**, in particular, thermal evolution only completes upon decomposition of the host framework (164 °C), which is contrary to the observations from the gas sorption analysis at RT. However, owing to the narrow constrictions of the channels in **1** (as a result of the channel corrugation), the CO_2 molecules follow an extremely hindered path through the channels and egress is further exacerbated by the increase in kinetic diameter of the CO_2 with increasing temperature. Conversely, for **2** and **3**, the guest molecule can move more freely through the channel, thus lowering the temperature of complete thermal evolution of the guest (66 and 64 °C, respectively).

Theoretical models constructed from crystallographic data were used to calculate framework electrostatic potential maps through DFT and semi-empirical methods. The maps yielded a detailed picture of the electrostatic interactions at the sorption sites. Both the CO_2 (MEP) and framework (FEP) electrostatic potentials where mapped onto an electron density contour of a CO_2 molecule. The MEP and FEPs shows overlapping of opposite electrostatic potentials, thus indicating the presence of stabilising coulombic interactions. The highest potentials are centred on the δ+ carbon atom of the CO_2 molecule and the δ– carboxylate oxygen atoms of the glutarate moieties. Furthermore, multiple weaker interactions exist between the δ– CO_2 oxygen atoms and various δ+ methylene hydrogens of the glutarate moieties. This demonstrates complete electrostatic complementarity between the sorption sites and the CO_2 molecules, resulting in a strong interaction responsible for stabilising the gas within these MOFs. Finally, from this study we can conclude that MOF **2** possesses the most favourable combination of steric and electrostatic topologies for binding CO_2 guest molecules, thus explaining the observed extreme sorption hysteresis and guest retention.

The second set of 3D Cu(II)-glutarate-based MOFs, $[Cu_2(glu)_2(bpa)]_n$ (**1**) and $[Cu_2(glu)_2(bpp)]_n$ (**2**), utilise flexible 4,4´-bipyridyl linkers as pillars. These MOFs can be grouped with the previous set as an isoreticular series. These two MOFs undergo spontaneous phase changes upon solvent loss at RT. The structures of the new phases reveal a reduction in the guest-accessible volumes, denoted as the narrow-channel (nc) forms (**1'** and **2'**), although crystals of **2** large enough for SCXRD analysis could only be obtained by means of CO_2 guest exchange under supercritical conditions. Visual inspection of the crystal structures for both phases revealed an enantiomeric conformational change in the glu moieties through inversion of the *gauche* torsion angles. Although the +gauche and −gauche conformations have the same molecular size and shape, they are spatially distinct, which results in the observed phase change. The changes in orientation, bend angles and coordination angles of the 4,4´-bipyridyl linkers suggest that these moieties play a crucial role in accommodating the glu conformational change.

CO_2 sorption analysis at RT reveals a stepped sorption profile for **1'**, with the loading doubling from ca 4 to 8 molecules per unit cell. The step in the sorption isotherm is attributed to the phase change of **1'** to **1**, thus approximately doubling the guest-accessible volume. Sorption of other gases such as methane, ethane and propane did not yield any steps in the sorption isotherms. MOF **2'** produced Type I isotherms for all the gases (no step) with significant hysteresis for ethane and propane sorption. The gas loading remains at its

maximum until vacuum is reached, thus indicating a high stability for sorbed ethane and propane within MOF **2**. The CO_2 content within **2** is double that of the other gases, further highlighting the affinity of these MOFs towards CO_2.

Using supercritical CO_2, it was possible to obtain CO_2 loaded crystal structures for both MOFs **1b** and **2'b**. The CO_2 molecules could be modelled and were found to utilise the same electrostatically stabilised sorption sites as the two rigid MOFs described in **Chapter 3**. More significantly, **1b** is in the wide-channel (wc) form, yielding eight CO_2 sorption sites. This is in agreement with the assertion that **1'** (nc) must convert to **1** (wc) in order to accommodate eight CO_2 molecules. Conversely, **2'** can accommodate eight CO_2 molecules per unit cell in the nc form. Although the crystal structure of **2'b** shows ten CO_2 positions per unit cell, a SQUEEZE electron-count of the guest-attributed density confirmed only eight CO_2 molecules. This is in good agreement with the sorption data.

The glu *gauche-gauche* enantiomeric conversion can follow paths: direct *gauche-gauche* (±g ⇋ ∓g, Route 1) or via the *trans* conformation (±g ⇋ t ⇋ ∓g, Route 2). The conformational barriers for a single uncoordinated H_2glu molecule were first determined by performing a scan of the potential energy surface. The *cis*-barrier (±g ⇋ ∓g) is 1.4 kcal mol^{-1} higher than the ±g ⇋ t barrier, thus indicating a higher probability for Route 2, although not exclusively (91% according the Boltzmann distribution at 298 K). The computational model was then scaled up to include four glu and four paddlewheel moieties, the smallest representation of the Cu-glu 2D grid. In this scan large changes in the orientation of the copper paddlewheel moieties were observed. Such changes have to be accommodated by the 4,4´-bipyridyl linkers coordinated to the paddlewheel. This also explains the absence of a conformational change for the MOFs with rigid 4,4´-bipyridyl linkers in the first set. In order to obtain a complete description of the enantiomeric conversion, we proceeded with a potential energy surface scan using a full unit cell as the computational model. The scan was performed in the space group *P*1, from wc to nc for both Routes 1 and 2, and allowing for optimisation of the entire unit cell except for the scan parameter (*gauche* torsion angles). Firstly, the simulations yielded the appropriate nc phase with relative differences in cell parameters (between wc and nc) very close to the experimental data. Furthermore, the energy barrier for Route 1 is ca 10 kcal mol^{-1} (per glu moiety) more stable than for Route 2. Additionally, the energy barriers for Route 1, for MOFs **1** and **2**, are in the same range as that of a free H_2glu molecule (3 – 7 kcal mol^{-1}). These energies are comparable with reported conformational barriers of molecules such as butane and its derivatives, which spontaneously interconvert under ambient conditions. Thus the only option for spontaneous enantiomeric conversion is via a direct *gauche-gauche* interconversion: ±g ⇋ ∓g. Analysis of the scan trajectories shows a large degree of distortion within the 4,4´-bipyridyl linkers, therefore highlighting their role in accommodating these phase changes.

Our investigation of the solvent exchange process of the 1D PCP, $[Cu_2(acetate)_2(dptz)]_n$ demonstrated that guest exchange in porous materials is not always straightforward. This material displays pleochroic properties that are evident when observing the crystals from different angles. 1D chains, formed by copper acetate paddlewheel moieties and the bptz linkers, form 2D layers through C—H···N interactions between adjacent linkers. These layers combine to form 1D guest-accessible channels occupied by chloroform guest molecules (**1a**). Solvent exchange with acetonitrile (**1b**) and nitromethane (**1c**) yielded structures where the linkers are rotated inwards towards the open channel. This adjustment maximises host-guest interactions and ensures optimal host-guest fit. Additionally, the solvent exchange revealed

the solvatochromic properties of the PCP, with a blue shift in the solid-state UV-vis spectra. This can be attributed to the rotation of the bptz linkers, which results in the loss or weakening of the C—H···N interaction between adjacent linkers. Calculated UV-vis spectra, for a dptz ligand with and without C—H···N interactions show blue-shifts in the absorption bands, consistent with our experiment. The solvatochromic properties could then be used as a probe to further our understanding of the solvent exchange process for this PCP. Optical microscopy with polarised light proved to be an invaluable tool for monitoring the solvent exchange. The crystals show an initial double V-shaped exchange pattern prior to complete solvent exchange for both acetonitrile and nitromethane.

The crystal facets, determined from face indexing single crystals using SCXRD, were overlaid with the crystal structure of **1a** to show that the mapped channels run diagonally, connecting two of the facets, (212) and (10-2). This implies that the solvent molecules must have a preference for (212) since solvent exchange is initiated through this facet first. Adsorption simulation using MM showed a higher adsorption enthalpy for (212) compared to (10-2), thus confirming the facet selectivity of the solvents. Furthermore, the adsorption enthalpy for acetonitrile was found to be higher than that for nitromethane, thus explaining the faster exchange kinetics for acetonitrile. All of the evidence suggested that a single crystal could not form this double V-shaped profile for the solvent exchange. We therefore proposed that the crystals must be growth twins subject to the double re-entrant corner effect. This effect results in the growth morphology observed for **1a** crystals and yields four mirrored domains which can produce a double V-shaped solvent exchange pattern.

This study highlights the subtleties of the underlying physics that influence the properties exhibited by MOFs. In particular, it has been shown that complementary weak electrostatic interactions can be more stabilising than a single strong interaction. This is a concept that also applies to the binding of biological molecules where more complex weak electrostatic interactions facilitate the functions and activities of these molecules. In the case of gas sorption, strong interactions can lead to higher gas uptake, but are often indiscriminate compared to weaker interactions. Electrostatic complementarity can also lead to greater selectivity for gas separation applications, and needs to be studied further for both the weak and strong electrostatic interaction regimes. A better understanding of this electrostatic-interaction landscape can improve the design of new functional materials for intended applications.

Relatively weak electrostatic interactions can also greatly influence the optical properties of a MOF and additionally could extent to other properties of these materials. Investigation of the correlation between these interactions and the associated properties of these materials can significantly improve our understanding of the host-guest dynamics in MOFs and should not be overlooked. Optically active organic ligands combined with an electrostatic complementarity is one approach towards targeted sensing of small molecules. Furthermore, in order to produce reusable and robust sensors, reversible host-guest binding would be preferred. The perfect sensor would have the optimum combination of substrate binding strength (for a measurable effect) and binding reversibility. Electrostatic interactions play a crucial role in the interplay between these properties and can lead to improved ligand design for optical applications.

Finally, conformational changes of the linkers in MOFs are greatly affected by the rest of the framework structure and have to be facilitated by other moieties within the MOF. This non-locality of framework flexibility indicates that the phase change behaviour of a MOF can be tuned by modifying both the ligands undergoing the conformational change and the ligands that are distorted to accommodate the change. This concept lies at the heart of classical engineering where construction facilitates function and both aspects are always considered in conjunction with one another. The study of all the afore-mentioned concepts are part of a larger scope driving the area of MOF research towards true "CRYSTAL ENGINEERING".

Future work on the systems presented here include extending these MOF to the use of different metal cations. There are several published structures (see discussion in Chapter 3) isoreticular to the copper-glutarate MOFs that contain zinc and cadmium cations instead of copper. Such systems provide the means for investigating the phase-change energy barriers as a function of metal-ligand coordination strength. This adds another dimension to the possibility of tuning the properties of these and other MOFs. It is also possible to pillar MOFs using cationic organic ligands with large non-coordinating anions. The anions would likely include into the MOF structure to charge balance the system and can therefore be systematically exchanged with smaller anions, such as the halide series. This has the effect of tuning both the electrostatics and pore size, which in turn leads to modulated sorption behaviour. The solvent exchange studies can be expanded to include 2D and 3D porous MOFs. In most MOF crystals, especially those of multi-ligand MOFs, the surface functionalities are distinct and can lead to different rates of adsorption of small molecules. Furthermore, surface modification of the MOFs with appropriate organic reagents can be used to vary the surface adsorption of solvent molecules and therefor tune the surface selectivity. The overlay of the crystal habit and structure allows for the identification of the crystal surface functionality and can therefor facilitate suitable selections of organic reagent for surface modification. These experiments are all plausible and do not require instrumentation beyond those presented in this dissertation.

APPENDIX

A CD containing all the supporting files and videos provides the following:

Chapter 3:

- CIF files and CheckCIF reports

Chapter 4:

- CIF files and CheckCIF reports
- Video S1 shows the potential energy surface scan for the square model.
- Videos S2 and S3 show the potential energy surface scan for the full unit cell model of MOFs **1** and **2**.

Chapter 5:

- CIF files and CheckCIF reports
- Videos showing the solvent exchange of acetonitrile and nitromethane
- Videos showing the pleochroic properties of the chloroform solvate (**1a**).